Broadband Acoustic Energy Harvesting Via Synthesized Electrical Loading

by

Nathan M. Monroe

S.B., Massachusetts Institute of Technology (2013)

Submitted to the Department of Electrical Engineering and Computer Science

In Partial Fulfillment of the Requirements for the Degree of

Master of Engineering in Electrical Engineering

At the

Massachusetts Institute of Technology

June 2017

Author…………………………………………………………………………………

Department of Electrical Engineering and Computer Science

May 26, 2017

Certified by……………………………………………………………………………

Jeffrey H. Lang

Professor of Electrical Engineering and Computer Science

Thesis Supervisor

Accepted By…....………………………………………………………………………

Dr. Christopher J. Terman

Chairman, Masters of Engineering Thesis Committee

Broadband Acoustic Energy Harvesting Via Synthesized Electrical Loading

by

Nathan M. Monroe

Submitted to the Department of Electrical Engineering and Computer Science on May 26, 2017

In partial fulfillment of the requirements for the degree of

Master of Engineering in Electrical Engineering

Abstract

The need for self-powered wireless sensor nodes is ever increasing. One promising technology for self-powered sensor nodes is acoustic energy harvesting (AEH): deriving energy from ambient sound. Current AEH designs are typically based on resonant structures, yielding narrowband energy harvesting and therefore low efficiencies from broadband noise sources. They also generally exhibit MEMS-scale sizes, with consequently low power outputs.

This work addresses the size and bandwidth of AEH devices. A large-scale acoustic energy harvester is presented, based on piezoelectric Polyvinylidene Fluoride film, $100cm^2$ in size. This harvester design was selected after analysis and comparison of magnetic, electrostatic, piezoelectric, and triboelectric transduction.

An energy-based dynamics analysis of such design a yields a third-order nonlinear differential equation, modeling the electromechanical dynamics of the system in open-circuit conditions. The model can be represented by a linearized equivalent circuit and subsequently a Thévenin equivalent model. Optimal broadband energy harvesting is achieved in theory with a conjugate matched load at all frequencies. This load is realized using operational amplifier circuitry, with special attention paid to stability challenges.

The AEH design was fabricated and tested with acoustic input over a range of 70Hz-7KHz. The model was validated experimentally via open-circuit voltage measurements and delivered power measurements with resistive loading. The AEH design was loaded with the designed conjugate matched load, with corresponding experimental voltage and delivered power measurements to demonstrate power output and bandwidth improvement.

While stability challenges and sensitivity to load capacitance precluded a perfect impedance match, broadband performance was achieved exceeding that possible with purely resistive loads, or with resonant structures demonstrated in literature. The implemented design harvests 1.6uJ per takeoff event of a 747 aircraft, or 0.25% or available power, requiring 58 volts to generate the forces necessary for impedance match. A perfect impedance match of this would require 1387 volts, harvesting 491uJ per takeoff event. Losses arise primarily at low frequencies, where a poor impedance match exists and significant energy exists. Given resolutions to stability, sensitivity and voltage challenges, the technology has the potential to be scaled up further and used in additional applications such as large-scale sound absorption.

Thesis Supervisor: Jeffrey H. Lang

Title: Professor of Electrical Engineering and Computer Science

Acknowledgements

I thank my parents for providing the constant support and help during this work and always, enabling me to achieve my dreams. I thank my brother and sister for being a constant source of inspiration.

I thank Professor Jeffrey Lang for having extreme patience with me, believing in me during challenging times, and consistently going above and beyond as an advisor and mentor. I thank Professor Anantha Chandrakasan for the support and direction, acting as effectively co-advisor.

I thank Mark Belanger for his support and patience during the machine shop portion of this work. I thank Professor Zoltán Spakovsky for his acoustics support and generous sharing of testing facilities.

Finally, I thank the Microsoft Corporation for providing the encouragement to return to graduate school.

Contents

List of Figures

11

12

List of Tables

Chapter 1

Introduction

1.1 Thesis Objective and Contributions

Acoustic energy harvesting (AEH) is a budding technology that allows energy to be extracted from acoustic noise for the purposes of powering electronic devices. Such a technology has many potential applications, such as powering low power wireless sensor nodes or Internet of Things devices in commercial, industrial or residential settings where minimizing human intervention is valuable. AEH has particular potential in settings such as airports, construction sites and highways, where acoustic noise is guaranteed but other forms of ambient energy, such as solar, are not. For similar reasons it is applicable in the context of noisy machinery, such as inside aircraft engine cowlings. AEH has potential in applications requiring power passively from ambient sound as well as applications with active wireless power transfer via sound. A related technology is noise isolation, which has many related challenges and often employs similar engineering approaches. The background surrounding noise isolation and acoustic energy harvesting, and existing approaches for both, are discussed in Chapter 2.

Existing AEH technologies are largely based on the property of Helmholtz resonance, a well-understood effect in acoustics and mechanics. Helmholtz resonating AEH technologies

suffer limited performance due to their narrowband energy harvesting. Their ability to efficiently harvest energy over narrow frequency ranges is of limited utility in real-world scenarios where noise is broadband.

Existing AEH technologies are also limited in size. Many existing AEH devices are MEMS-scale with collection areas of square millimeters or smaller, and consequently offer low power output. This small size combined with a narrowband response severely limits performance of existing acoustic energy harvesting devices, as well as their utility in real-world scenarios.

This research addresses these two limitations by presenting a large-scale acoustic energy harvester capable of efficient broadband energy harvesting. This is achieved by a combination of transducer design, modeling techniques and accompanying circuit design. The overall objective of this work is two-fold: design and build an acoustic energy harvester of large scale exceeding the scale limitations of existing approaches, and capable of efficient harvesting of broadband noise, exceeding the limitations imposed by existing designs.

1.2 Thesis Organization

This chapter provides a context for the research, a motivation and the research contributions made by this work. Chapter 2 introduces a summary of background knowledge requisite for the work, including various transducer technologies, diffraction issues, acoustic modeling techniques, the impedance matching technique for energy transfer, and an overview of existing acoustic energy harvesting techniques. Chapter 3 presents the derivation of an analytical model for an acoustic energy harvester design, with adjustments for real-world implementation effects and higher mode considerations. Chapter 4 presents the realized mechanical design for the harvester modeled in Chapter 3. Chapter 5 presents the design for an electronic load

associated with the harvester to result in optimal broadband energy harvesting. This design is informed by the harvester model derived in Chapter 3 and also includes a realization of these electronics. It also discusses stability considerations associated with the design, as well as a parameter sensitivity analysis. Chapter 6 presents a testbench for the acoustic system, including test facilities and equipment, calibration procedures, electrical instrumentation, and an automated data collection procedure for rapid, precise and repeatable measurements. Chapter 7 presents harvesting results including a comparison of modeled performance versus measured performance. Chapter 8 provides a summary of results and conclusions, and suggestions for future work.

Chapter 2

Background

Background material is presented, with a focus on acoustic system modeling. An overview of the physical basis of acoustic energy is presented, along with the motivation for broadband harvesting. Various transducer technologies are introduced, with a discussion on their limitations and a discussion of the optimal transducer technology for acoustic energy harvesting. An in-depth discussion of acoustic modeling techniques is presented, building an analogy between acoustic systems and electrical circuits and motivating the selection of transducer technology for this work. The theoretical basis for impedance matching and optimal power transfer is presented. Finally, an overview of existing acoustic energy harvesting approaches is presented.

2.1 Acoustics and Energy

Acoustic energy harvesters are constrained by the amount of input energy available acoustically. Generally, this can be considered both in terms of sound level and sound spectrum. Sound level is generally given in dB SPL, or decibels of sound pressure level. This is a pressure measurement, where 0 dB is equal to 20 uPa. Therefore,

$$\textit{Sound Pressure Level} = 20\log_{10}(\frac{p_{\text{rms}}}{p_{\text{ref}}}) \qquad (2.1)$$

where $p_{\text{ref}} = 20$ uPa.

Sound intensity I, given in watts per meter squared, is a strong function of distance from the sound source and can be shown to follow the inverse square law [1]

$$I = \frac{P}{4\pi r^2} = \frac{p_{\text{rms}}^2}{2Z_0} \qquad (2.2)$$

where P is the source power in Watts, r is distance from source in meters, and Z_0 is acoustic impedance as defined below. Therefore, the amount of available energy is highly sensitive to distance from the source.

Acoustic impedance is derived from a far-field plane-wave solution [1], and is defined as the ratio of complex pressure $\hat{P}$ (Pa) to complex particle velocity $\hat{U}$ (m/s), such that

$$Z_O = \frac{\hat{P}}{\hat{U}} = \sqrt{\gamma P_o \rho_o} \qquad (2.3)$$

where γ is the adiabatic constant, P_o is atmospheric pressure (Pa), ρ_o is air density. (Kg/m^3) At standard temperature and pressure, Z_o is approximately equal to 420.5 Pa/(m/s). As will be discussed in Section 2.5, this source impedance is critical for matching to an acoustic energy harvester's load impedance for optimal energy harvesting in an analogous manner to optimal impedance matching in a power electronics context. The goal of this thesis being energy harvesting from aircraft noise, it is instructive to understand the nature of the energy available from this source. At a distance of 100 meters, the sound pressure level produced by aircraft is

SPL [dB]	I [W/m^2]	P$_{rms}$ [Pa]	U$_{rms}$ [m/s]	X$_{rms}$ (at 50Hz) [μm]
100	0.01	2	0.005	16
110	0.1	6.3	0.016	50
120	1	20	0.05	160
130	10	63	0.16	500
140	100	200	0.5	1600

Table 2.1. Acoustic parameters of a generalized noise source at 100-140 dB SPL.

approximately 100-140 dB SPL. Based on the linearized physics model, this gives rise to

acoustic parameters as seen in in Table 2.1.

As measured at a distance of 1000 feet, a typical frequency spectrum from a jet airplane

is given in Figure 2.1. This power spectral density provides information on total sound pressure

level contained within each frequency bin, with bin centers denoted by data markers.
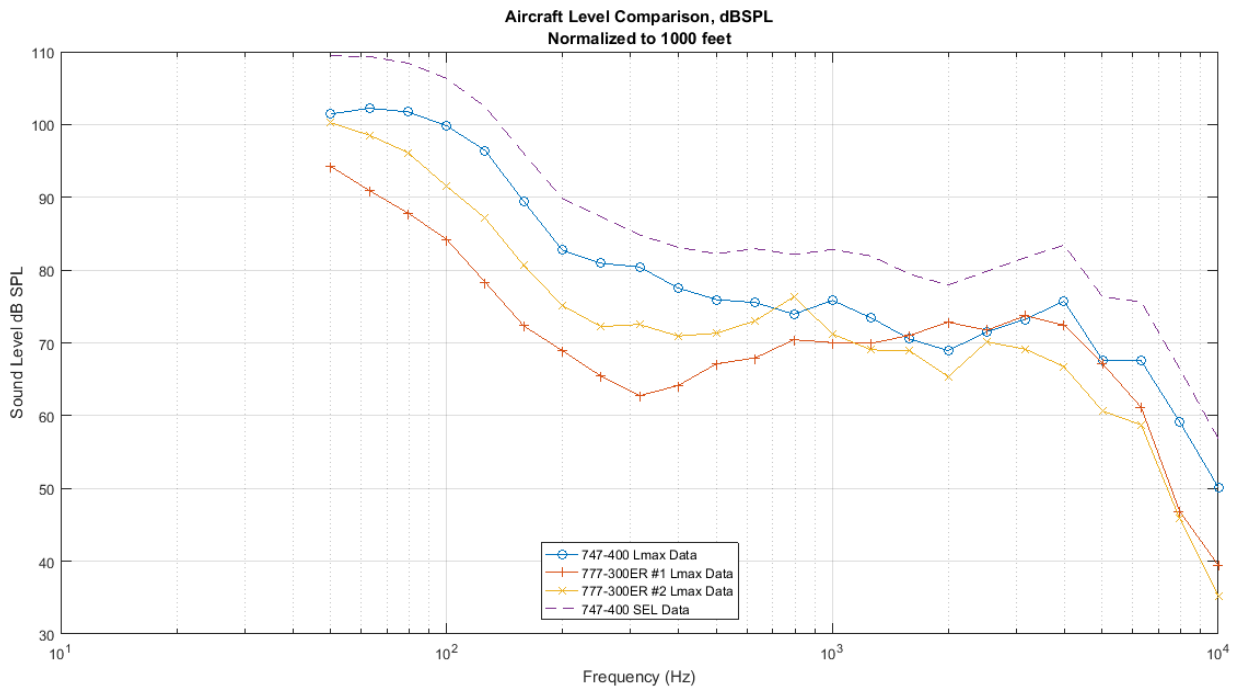
Figure 2.1. Typical noise spectra from various jet aircraft, taken at 1000 feet.

Bins are defined logarithmically, with centers on third-octave bands, as per industry standard.

Most notably, the noise is broadband in nature regardless of aircraft type, with the majority of

energy contained below 1000 Hz. Using a Boeing 757-200 as a reference, summation over

frequencies yields ~117 dB SPL, or approximately 0.5 W/M^2 at 1000 feet (330 meters).

2.2 Sound Transducer Technologies

Multiple technologies exist for the transduction of acoustic energy into the electrical

domain, and there is significant overlap between acoustic energy harvesting technology and

sound sampling technology (microphonics). Several technologies are discussed below. A crucial

difference is that in microphonics, a primary design goal is to maximize impedance presented to

the source, minimizing loading of the signal and therefore maximizing fidelity and accurate

reproduction of the sampled signal. In addition, primary goals include flat frequency response,

high linearity, minimization of THD+N (total harmonic distortion plus noise) and optimization

for perceived sound quality based on psychoacoustic factors. In contrast, in acoustic energy

harvesting the primary goal is to present an impedance which is matched to the source

impedance for maximum energy transfer, with no attention paid to perceived sound quality or

related factors.

2.2.1 Electrostatic Transduction

In an electrostatic (condenser) microphone or energy harvester, two conductive plates or

diaphragms are separated by a small gap, forming a capacitor [16]. An incoming pressure wave

does work against one diaphragm, causing it to move. The diaphragm moves in the presence of

an electric field, which is generated by a built-in bias potential (as in large-diaphragm condenser

microphones) or a pre-charged electrostatic material (as in electret condenser microphones). The

motion of the diaphragm causes a change in capacitance between the plates. By the principles of electrostatics, a change of capacitance with a fixed charge results in the generation of a time-varying voltage. In a practical electrostatic transducer the parallel plates have a parasitic capacitance which must be modeled and carefully engineered for optimal performance.

2.2.2 Magnetic Transduction

In a magnetic (dynamic) microphone, a diaphragm is caused to move by an incident pressure (sound) wave [16]. In one implementation, the diaphragm contains a coil of wire which moves through a magnetic field produced by static permanent magnets. As described by Faraday's law of Induction, the motion of a wire through a magnetic field generates a voltage which by proper electrical design can be extracted as electrical power. In a related implementation, a diaphragm with an associated magnet moves through a stationary coil, generating voltage on the same principle. In a practical magnetic transducer, the coil's resistance and inductance must be modeled and carefully engineered for optimal performance.

2.2.3 Piezoelectric Transduction

In a piezoelectric microphone or energy harvester, a diaphragm is supported by a structure with piezoelectric materials [16]. An incoming pressure wave moves the diaphragm against the spring force arising from the support structure. As described by the piezoelectric effect, a stress in a piezoelectric material creates a dipole moment, resulting in the generation of charge which is extracted as electrical energy or signal. In a practical piezoelectric transducer, the material's capacitance affects the electromechanical properties of the system, and must be modeled and carefully engineered for optimal performance.

2.2.4 Triboelectric Transduction

Triboelectric transduction is an emerging technology in energy harvesting. As described by the triboelectric effect, two dissimilar materials generate an electric charge (static electricity) upon contact. This effect has been demonstrated to have potential in energy harvesting. In this implementation, an incoming pressure wave moves a diaphragm, causing the repeated contact and separation of two materials, resulting in the constant generation of triboelectric charge which is extracted as electrical energy.

2.2.5 Optimal Transduction for Acoustic Energy Harvesting

A crucial commonality between the transduction technologies named above is reversibility. A force causes the generation of electrical energy, but the effects can be applied in reverse, applying electrical energy to produce a force. This effect will be exploited in designing a broadband energy harvester, as described in future sections.

While in theory the various transduction technologies equivalently transduce acoustic energy into electrical energy, they differ in implementation and tradeoffs associated with a practical design. As will be discussed in Section 2.5, an optimal broadband acoustic energy harvesting system can be created using a broadband impedance match between the acoustic impedance of air and that of the harvester. Due to the practicalities of building a real acoustic system, this generally involves construction of negative reactive circuit components. As an equivalent statement, the harvester is loaded with an electrical system to provide a frequency-dependent force to the harvester, which counteracts frequency-dependent forces inherent in the harvester to provide a broadband impedance match.
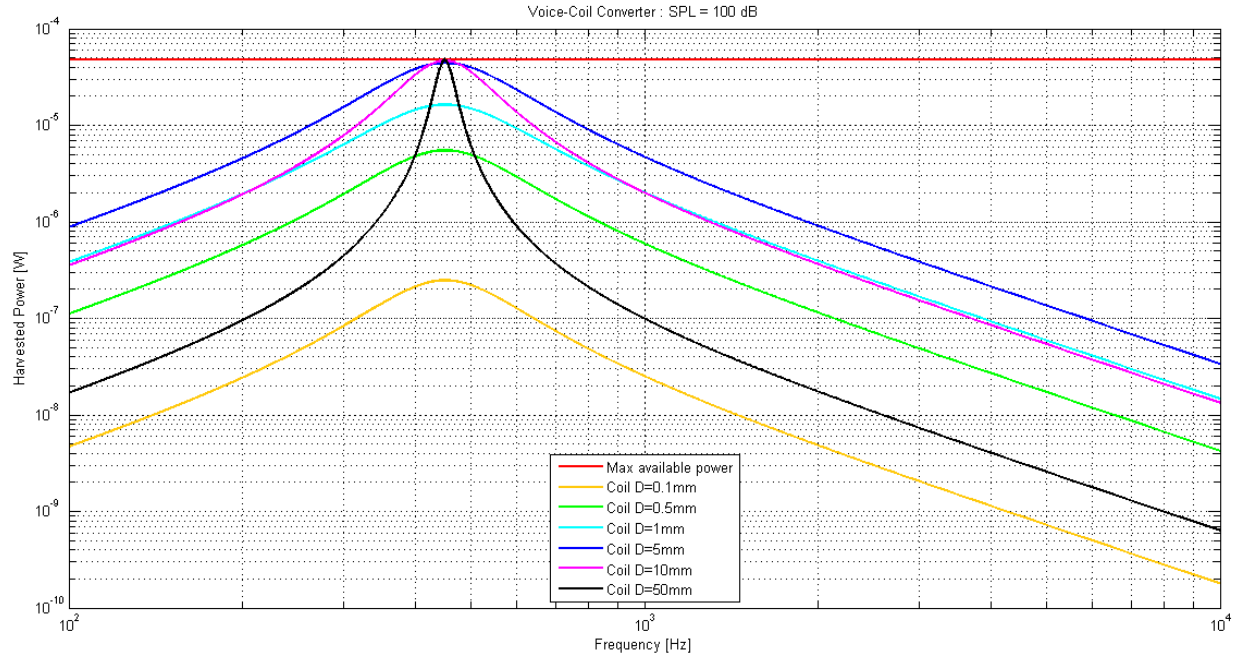
Figure 2.2. Harvested power versus frequency for different coil diameters for a square 10x10cm magnetic harvester with resonant frequency of 500Hz and 100 dB SPL input energy.

As discussed in Section 2.2.2, a magnetic harvester is made by a diaphragm with a coil of wire, which is acted upon by an acoustic force to move through a magnetic field, producing a current. The magnetic field is produced by a stationary magnet. To investigate the feasibility of such an approach for acoustic energy harvesting, an electromechanical circuit model was derived for a generic magnetic harvester based on principles discussed in Section 2.4. The details of this model and simulation code are presented in Appendix A. A key design decision is the gauge of wire and number of turns used in the coil. An inherent tradeoff exists between coil mass and coil resistance. An increase in wire diameter reduces resistance at the expense of increased mass. The increased mass requires more current through the coil for an optimal impedance match. The losses associated with increased current counteract the energy savings from reduced coil

resistance. This tradeoff is seen graphically in Figure 2.2. Even with an optimal coil diameter, optimal broadband harvesting cannot be achieved in this implementation.

An electrostatic harvester is constructed as discussed in Section 2.2.1. As in the magnetic harvester, an electrostatic harvester requires an electronic load to apply a force to the harvester for a broadband impedance match. It can be shown that the pressure applied to an electrostatic energy harvester takes the form

$$P_{\mathrm{e}} = \frac{\epsilon V^2}{2d^2} \quad (2.4)$$

with Pressure P_{e} in Pascals, dielectric constant ε in Farads/meter, Voltage V, and distance between plates d in meters. It can be shown that excessively high voltages are required to produce the electric fields necessary for impedance matching and therefore efficient energy harvesting. As an example from Table 2.1, 110 dB sound at 50 Hz requires a displacement of 50 um rms and a pressure of 6.3 Pa rms. Substituting into (2.4), this yields a required voltage of nearly 10kV, much too high for practical implementations. Thus, electrostatic transduction was deemed impractical for this application.

Triboelectric transduction is based on the mechanism of repeated contact and separation of two materials. Such contact and separation at a displacement of 50 um applies severe constraints on the mechanical design of the system, making this approach impractical.

Piezoelectric transduction was chosen primarily because of it's low loss properties and low cost. Furthermore, piezoelectric polymer film of Polyvinylidiene Fluoride was chosen in favor of piezoelectric ceramics such as PZT due to it's low weight, tunable compliance, low losses and low cost.

2.3 Diffraction Effects

One design issue that is common to acoustic energy harvesters and microphones is that of diffraction. At audio frequencies, wavelengths are typically much longer than transducer geometries. For example, the wavelength of an acoustic wave at 1KHz is approximately 30cm. As seen in Figure 2.3 below, a consequence of this is that the transducer looks "small" to the incoming wave, and the incoming wave diffracts around the transducer. The transducer is often thin enough that the incoming wave experiences little phase shift from the front to the back of the transducer. A negative consequence of this is that the incoming pressure wave will exert an equal pressure on both sides of the transducer diaphragm, resulting in zero force on the diaphragm and therefore no energy transfer. Solutions to this issue will be discussed in future sections.
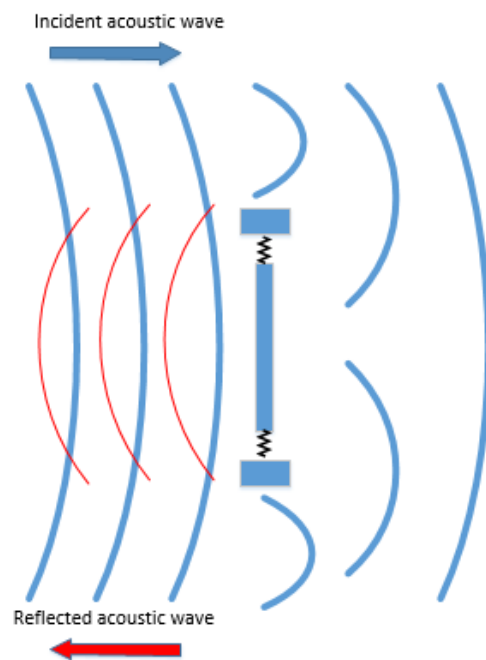
Figure 2.3. Diffraction of an acoustic wave around a "small" transducer

2.4 Acoustic System Modeling

Powerful analytical tools exist which allow for rapid and intuitive modeling of the behavior of such systems. The most commonly used tool is the circuit analogy, which models an acoustic system as an electrical system. Such a model enables the simulation of acoustic systems by numerical simulation software such as SPICE. In addition, it allows acoustic systems to be analyzed using classical circuit techniques such as superposition, sinusoidal steady state analysis and pole-zero analysis. This chapter focuses on the lumped-element circuit analogy technique for acoustic systems.

2.4.1 Lumped Element Approximations

The quasistatic approximation is required to enable acoustic systems to be represented as lumped-element circuit models with reasonable accuracy. This quasistatic approximation has an analogous assumption in electrical circuit systems. In an acoustic system, the quasistatic approximation assumes that the geometries of an acoustic system are much smaller than the wavelength of the acoustic waves which are interacting with the system, in the axis of wave propagation. A consequence of this is approximation is the approximation that pressure is constant over distance, and that velocity varies linearly with distance. This is seen in Figure 2.4 [1]. This approximation allows transmission line effects to be ignored, and the "lumping" of distributed attributes into idealized components. Such an approximation is also used in circuit modeling, when the circuit's geometries are much smaller than the electromagnetic wavelengths which are incident on the system. In an acoustic system, the quasistatic approximation can be made with little error when the system's geometries are much smaller than the incident waves. The relationship between frequency and wavelength of an acoustic wave is given by
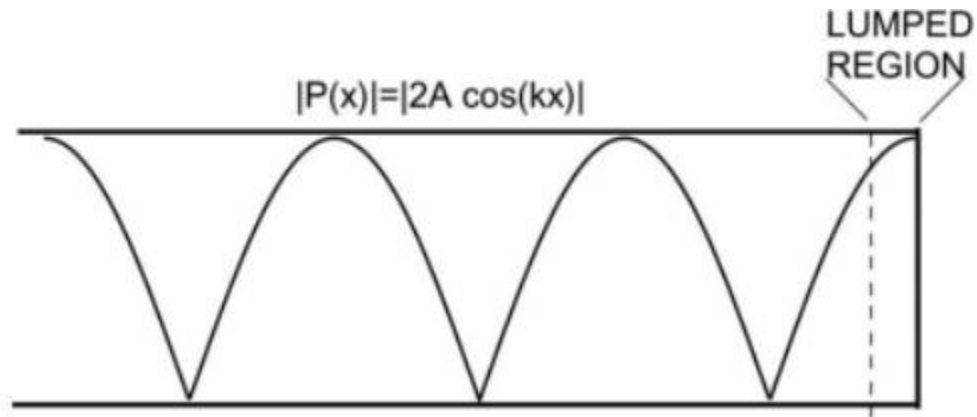
Figure 2.4. The quasistatic regime applies for structures much smaller than the wavelengths of interest [1].

$$C_0 = f * \lambda \qquad (2.5)$$

where C_0 is 334 meters/second at standard temperature and pressure, frequency f in Hz and wavelength λ in meters. A few representative examples of frequency and wavelength are given in Table 2.2. Because the harvester is designed to be much smaller than the wavelengths associated with the frequencies of interest (50Hz to 1KHz), the quasistatic approximation is valid for the modeling of this system. Corrections to this approximation are presented in Section 3.7.

Frequency (Hz)	Wavelength (m)
10	34.3
100	3.43
1k	0.343
10k	0.034

Table 2.2. Various frequencies and wavelengths of sound in air at standard temperature and pressure, with C_0=343 m/s.

The second approximation is that of linearity. While not required for lumped element modeling of an acoustic system, it allows for modeling of the system with standard linear electrical components. Air is a nonlinear medium, however it can be approximated as linear via a first order Taylor approximation for "small signal" sound levels, when particle velocity's magnitude |U| is much less than the speed of sound C_O in the medium. For sound levels and frequencies typical of human hearing, the linear approximation can be made with negligible error [26].

Two distinct models can be applied for modeling acoustic systems as lumped-element circuit models: the *impedance analogy* and the *mobility analogy*. This chapter will first focus on the impedance analogy then make the extension to the mobility analogy.

2.4.2 Force Source as Voltage Source

In the impedance analogy model, pressure is modeled as an "across variable", with units of Pascals, or Newtons per square meter [1]. This is analogous to voltage in an electrical system. Consequently, a pressure source is analogous to an electrical voltage source. In mechanical systems this is often instead represented as force (Newtons), which is simply pressure multiplied by area.

2.4.3 Velocity Source as Current Source

In the impedance analogy model, volume velocity is modeled as a "through variable", with units of cubic meters per second. This is analogous to current in an electrical system. Consequently, a volume velocity source is analogous to a current source. In mechanical systems the through variable is often instead represented as velocity (meters per second), which is simply volume velocity divided by area. In this case, voltage is analogous to force.

2.4.4 Loss as Resistor

In the impedance analogy model, a real loss can be modeled as an electrical resistor. In a mechanical or acoustic system, real losses can come from effects such as friction and viscous losses. In acoustic systems, such a resistance has units of Pascals/meters^3/second. In mechanical systems with force and velocity as across and through variables, a loss resistor model has units of Newtons/meters/second.

2.4.5 Compliance as Capacitor

In the impedance analogy model, a compliance element can be modeled as an electrical capacitor [1]. This can be seen by the relation between a compliance's pressure and volume velocity

$$u(t) = C_A \frac{dp(t)}{dt} \qquad (2.6)$$

where C_A is acoustic compliance, given in m^3 / Pa. This can be seen as a conservation of mass statement. In an equivalent electrical model of a mechanical system, a similar relation holds between force and velocity and is given by

$$v(t) = C_M \frac{df(t)}{dt} \qquad (2.7)$$

where C_M is mechanical compliance, given in meters/newton.

2.4.6 Mass as Inductor

In the impedance analogy model, an acoustic mass element can be modeled as an electrical inductor. This can be seen by the relation between pressure and volume velocity [1]:

$$u(t) = \frac{1}{L_A} \int p(t)dt \quad (2.8)$$

where L_A is acoustic mass, given in Pa*s^2/m^3. This can be seen as a conservation of momentum statement. In an equivalent electrical model of a mechanical system, a similar relation holds between force and velocity:

$$v(t) = \frac{1}{L_M} \int f(t)dt \quad (2.9)$$

where L_M is mechanical mass, given in newtons*second^2/meters.

A summary of the impedance analogy for both acoustic and mechanical systems is shown in Figure 2.5 [1].
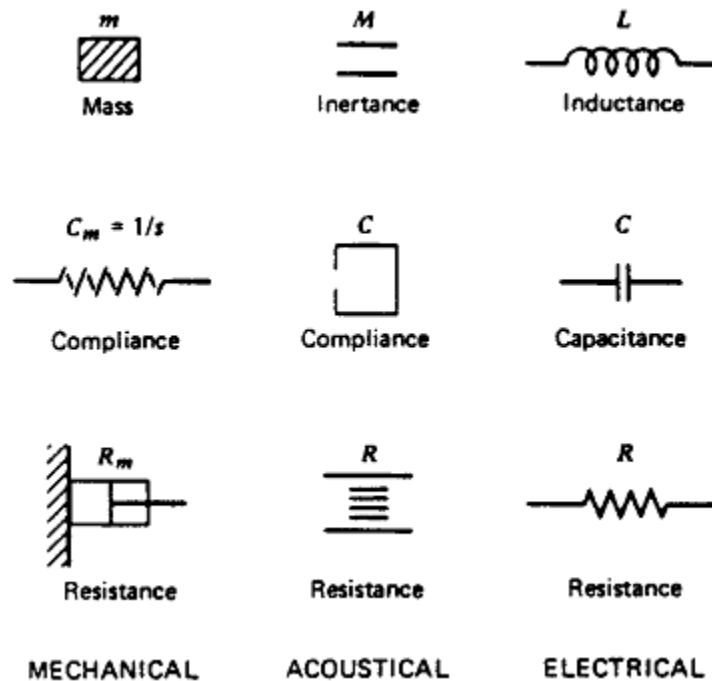
Figure 2.5. Summary of analogous mechanical, electrical and acoustical components.

2.4.7 Mechanical to Mechanical Transformers as Electrical Transformers

Various acoustic structures exist which exhibit a lossless transformation between volume velocity and pressure. Two such examples are horns and pistons, as seen in Figure 2.6. [2].

Such structures maintain energy conservation, while trading pressure for volume velocity or vice-versa. Consequently they have the effect of transforming the acoustic impedance seen at their input terminals. Such a structure can be modeled electrically as a transformer. The windings ratio T is given by

$$T = \frac{U_2}{U_1} = \frac{P_1}{P_2} = \frac{Area_2}{Area_1} \quad (2.10)$$

where U_1 and U_2 are the respective input and output volume velocities, P_1 and P_2 are the
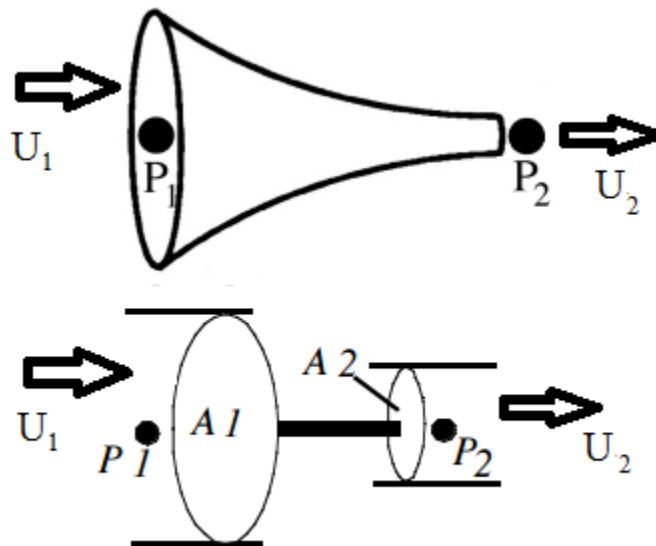
Figure 2.6. Horn (top) and piston (bottom) structures are analogous to electrical transformers, with windings ratio analogous to area ratio [2].

respective input and output pressures, and Area$_1$ and Area$_2$ are the respective input and output cross sectional areas. A mechanical equivalent of a transformer between force and velocity is a lever arm, which will not be discussed in further detail here.

2.4.8 Transducer as Electrical Transformer

The transducers described in Section 2.2 share the commonality that they transduce mechanical energy (force and velocity) into electrical energy (voltage and current). Applying this to the circuit analogy described in Sections 2.4.1-2.4.7, an appropriate model for a transducer is an electrical transformer. Such a transducer converts mechanical through and across variables (velocity and force) to electrical through and across variables (voltage and current), in a reversible manner. The effective windings ratio of such a transformer model is based on implementation: choice of transduction method, geometries, material properties and other design parameters. Real-world transducers also have various parasitic elements as discussed in Sections 2.2.1-2.2.4. In the impedance analogy, a more formal representation for electromechanical transduction is cross-coupled voltage and current sources, as seen in Figure 2.7.

2.4.9 Mobility Analogy

The mobility analogy is an alternative representation of a lumped-element acoustic model as an electrical circuit, and is reciprocal to the impedance analogy. In the mobility analogy, volume velocity is instead mapped to electrical voltage and pressure is mapped to current [1]. Losses, compliances, and masses are now modeled as parallel resistors, inductors and capacitors, respectively. This is analogous to a dual circuit of an electrical circuit, or a transformation from Thévenin equivalence to Norton equivalence. Impedance analogy and mobility analogy circuit models for a second-order Helmholtz resonator acoustic system are shown in Figure 2.7.
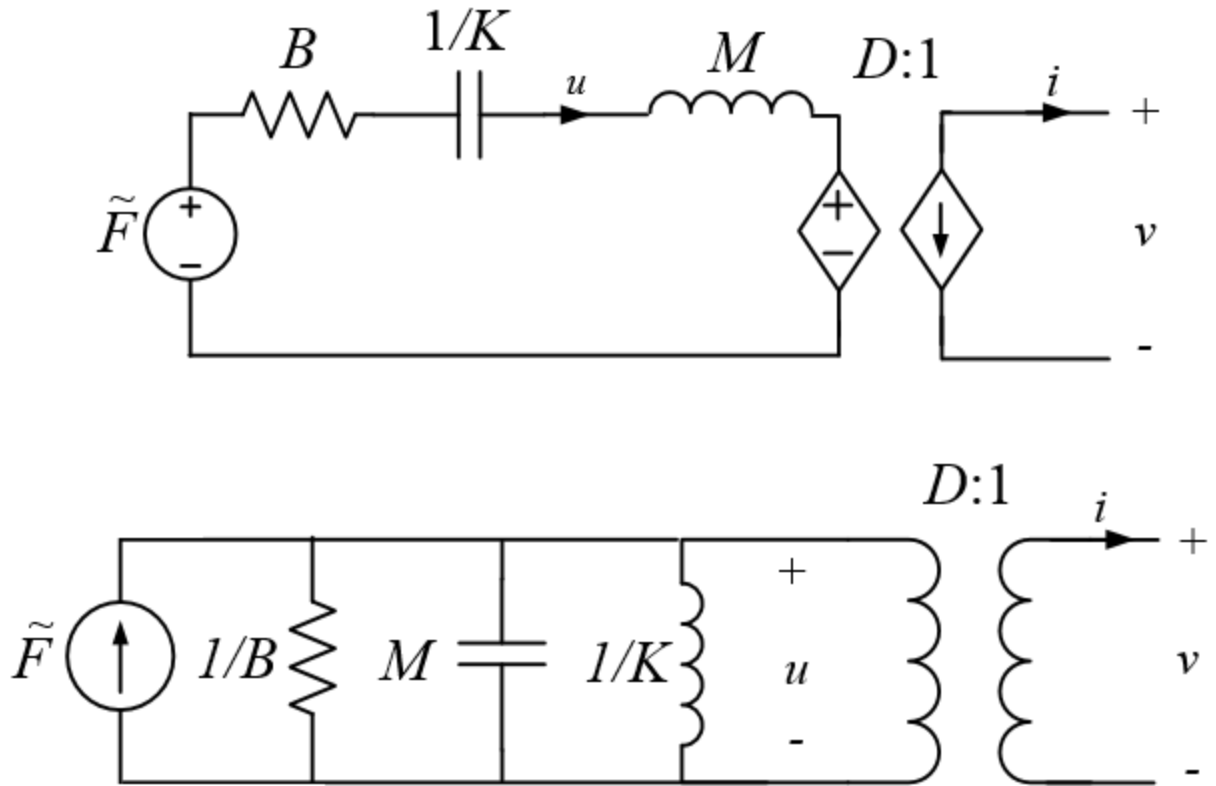
Figure 2.7. Impedance (top) and mobility (bottom) circuit analogies for generic Helmholtz acoustic system with transducer.

2.5 Load Matching for Optimal Energy Harvesting

An acoustic system can generally be described by an equivalent circuit model, as seen in Figure 2.7. Using standard linear circuit techniques, this can be described by a Thévenin equivalent circuit model with a frequency-dependent source and complex source impedance, as seen in Figure 2.8 [3].

A critical insight of this model is that it is *electromechanical*. It captures both the electrical and mechanical properties of the system. Any mechanical change to the system will
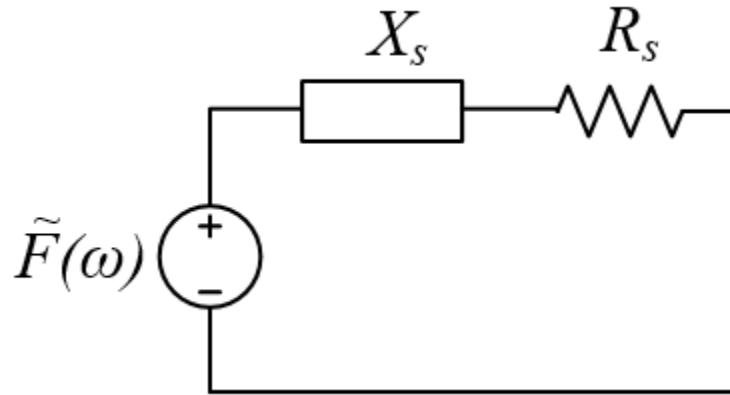
Figure 2.8. Thévenin equivalent circuit model of generic acoustic system, with frequency-dependent voltage source F(ω), reactance X_s and resistance R_s.

manifest as a change in Thévenin impedance seen electrically, and vice-versa. Energy applied to the system mechanically will be seen electrically, and vice-versa. Therefore, mechanical properties of the system are affected by electrical loading. For example, a reactive loading to the system will change it's complex impedance characteristic and it's resonant frequency. This property will be exploited to achieve broadband energy harvesting.

As described by the maximum power transfer theorem [27], a power source with source impedance Zs will transfer the maximum amount of power to a load impedance Zs* which is the complex conjugate of the source impedance, as seen in Figure 2.9b. This concept is widely used in acoustics, electromagnetism, vibration control and many other subfields within electrical and mechanical engineering. For an electromechanical Thévenin equivalent model of an acoustic system as in Figure 2.8, this optimal load is realized as a matched real part Rs and a negated reactive part Xs, as seen in Figure 2.9b.
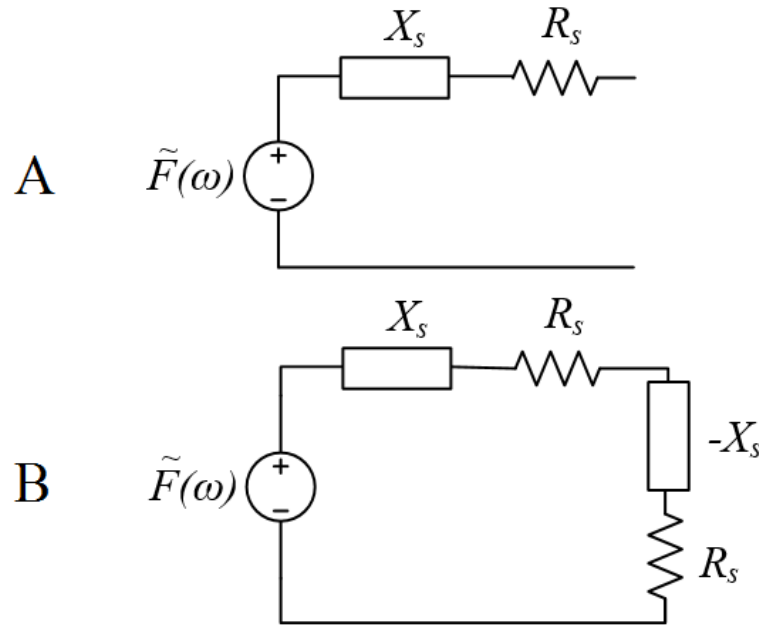
Figure 2.9. (a) Maximum power transfer is achieved to a load impedance which is the complex conjugate of the source impedance. (b) Such a match is realized with a matched real part and a negative reactive part.

Traditionally such a load is realized at a single frequency using a positive reactive component such as inductance (to match reactance of a capacitor) and capacitance (to match reactance of an inductor). However, such an approach yields narrowband response, which has little utility in energy harvesting applications where input energy is broadband. This technique is widely used in Power Factor Correction circuits, where impedance match is only required at a single frequency [15]. A similarly matched load can also be realized using a *negative* reactive component. For example, matching an inductive source with a negative inductive load. This has the advantage of matching impedance at all frequencies, allowing for broadband response. However it introduces a number of challenges, including sensitivity and stability, which will be discussed in Sections 5.2 and 5.4, respectively.

2.6 Existing Acoustic Energy Harvesting Approaches

A common approach to acoustic energy harvesting is founded upon the use of a

Helmholtz resonator [4]. As seen in Figure 2.10, a Helmholtz resonator is a hollow cavity with a

narrow neck, which receives an incident sound wave. Typically, a backplate acts as a diaphragm

which moves in a force field in an implementation of one of the transduction technologies

described previously. A Helmholtz resonator can be modeled as a second order system,

analogous to a RLC circuit system or mass-spring-dashpot system as seen in Figure 2.10 [5].

An advantage of this approach is that minimal damping can result in very high Q, or very

highly resonant systems. The Q amplification provided by this resonance can result in highly

efficient energy transfer at the resonant frequency due to mechanical systems having generally

smaller forces and large motions. However, a significant drawback of this approach is that a high

Q results in a very narrow bandwidth, significantly limiting the frequencies over which the

harvester can efficiently harvest energy. This approach still has application in areas where the
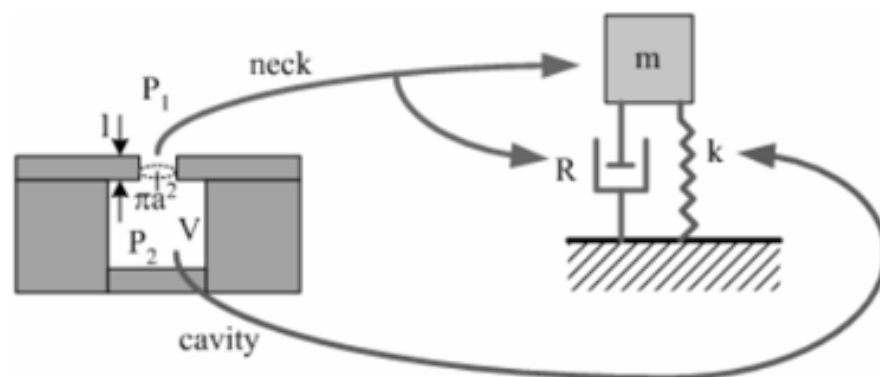
Figure 2.10. A Helmholtz acoustic resonator and it's equivalent second-order model.

noise source is fixed at a known frequency. However, it has low efficiency for noise sources which are broadband or varying in frequency, such as aircraft noise.

Multiple approaches [6] have been proposed for increasing the frequency range of energy harvesters, or allowing harvesting frequency to be tunable. Phipps et al [7] has demonstrated a system with multiple energy harvesters in parallel, each having a slightly different resonant frequency. This system has the appearance of a broadband system. However, it has the drawback of being space inefficient, with very few of the many harvesters collecting energy efficiently at any given time. Williams et al [8] describes a system with a reduced Q factor (increased dampening). While this does increase the frequency range of collection, it comes at the expense of decreasing collection efficiency at any one frequency.

Many sources have described achieving tunable harvesting by the use of variable-length cantilevers or variable spring tension [6]. While this approach allows for tunable resonant frequency, the downside of narrow bandwidth remains. A coupled oscillator effect with a higher-order system has been described by Petroupolos et al [9], however it also demonstrated reduced efficiency than a generator with a single mass. Amplitude limitation and nonlinear effects have been described variously in the literature [6]. These devices work generally by exploiting a nonlinearity in the system, allowing the resonant frequency to be changed with manipulation of system operating point. These devices typically show increased bandwidth over a variable range of frequencies and often are sensitive to the direction of frequency variation. Thus, they are unable to collect energy from arbitrary frequency/time combinations and as such are not truly broadband.

Multiple sources [10] [11] have reported the use of variable load impedance to enable a tunable harvester. These systems generally exploit the reversible nature of the transducer to
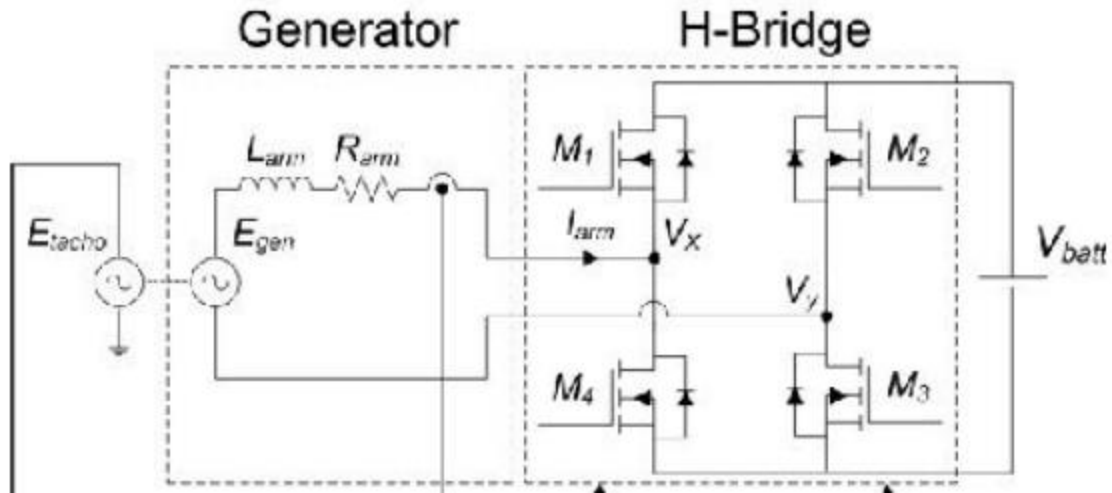
Figure 2.11. A full-bridge switching rectifier for tunable load impedance.

manipulate the reactance of the mechanical system by variation of reactance in an electrical load.

Mallick et al [12] demonstrates the variation of resonant frequency by variation in load

capacitance. This approach has been extended by the use of switching power electronics to

synthesize reactance, as reported by Kaphengst et al [10], and also Chang et al [11]. In this

approach, an electrically controllable H bridge active rectifier is used in lieu of a standard full-

bridge diode rectifier as seen in Figure 2.11, in a similar approach to that used in active power

factor correction circuitry [15].

By sensing source voltage and load current and addition of a classical control scheme, the

active rectifier can be controlled to synthesize negative electrical reactances to interact with

mechanical reactances in order to tune the resonant frequency electrically. This approach has

also been used to create a harvesting system with multiple resonant frequencies, as described by

Chang et al [11]. It is this approach that will be extended in this work to create a truly broadband

energy harvester.
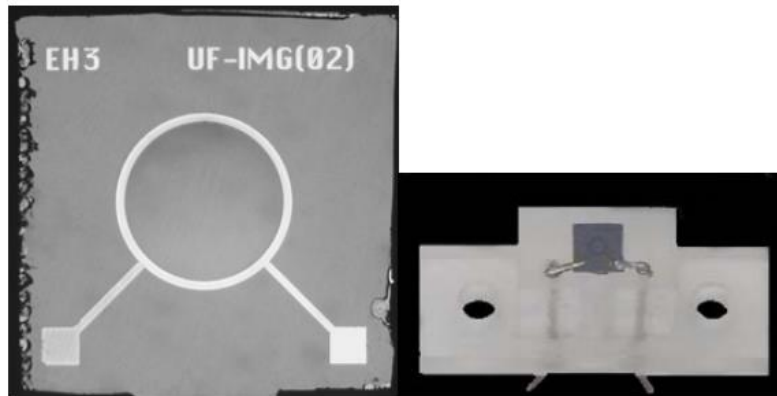
Figure 2.12. A MEMS-scale acoustic energy harvester.
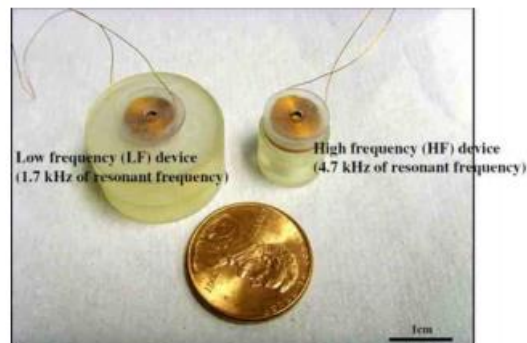
Figure 2.13. A Magnetic acoustic energy harvester.

Another notable commonality between existing energy harvesters is their size. The majority of harvesters reported in literature are either micro-scale based on MEMS techniques, or very large scale vibration harvesters for ocean wave-based applications. Existing MEMS harvesters tend to have collection areas of fractions of a square centimeter, with correspondingly small power output levels. For example, Horowitz et al [5] reports a nano-scale harvester based on Silicon-on-Insulator techniques with a collection area of 17.4mm^2, as seen in Figure 2.12.

Kim et al [13] report a slightly larger collector based on magnetic transduction, as seen in Figure 2.13.

The generally diminutive size coupled with the limitation of narrow band energy harvesting limit existing acoustic energy harvesters to very low power output levels, on the order of nanowatts to microwatts. On the opposite end are large-scale harvesters intended for marine wave applications [17]. Little research attention has been directed towards energy scales between these two extremes, such as energy scales appropriate for wireless sensor node applications. Thus, a significant opportunity exists to innovate and improve upon acoustic energy harvester technology, both by increasing frequency range and improving upon size. The improvement of output power would enable the use of acoustic energy harvesters in wireless remote sensor node or similar applications.

The use of PVDF and negative capacitance circuits has been explored in the context of noise isolation. Sluka et al [18] describe a curved PVDF film loaded with a negative capacitance generated by an operational amplifier circuit. Broadband performance is limited by their inability to match the load with the frequency-dependent capacitance PVDF arising from it's frequency-dependent dielectric constant. Various authors [18] [19] also describe a dynamic circuit with feedback control to optimize the load negative capacitance value. Date et al [20] provides the initial theoretical analysis of the PVDF/negative capacitance approach, and describes an extreme sensitivity to load capacitance, which requires a ~0.1% precision. Fukada et al [21] describe tunable narrowband sound isolation using a negative capacitance load. Kim et al [22] describe a successful broadband sound isolation system using two pieces of curved PVDF film and a negative capacitance circuit. Crucially, the above literature uses piezoelectric PVDF film with negative capacitance load to increase effective stiffness of the system, providing a sound

isolation effect by reflecting incident sound. In such systems no energy is extracted from the sound and impedance of the load is maximized rather than matched to the source. No precedent was found literature for the use of PVDF and negative capacitance for acoustic energy harvesting. There was similarly no precedent found for demonstration of similarly large-scale or broadband acoustic energy harvesting.

2.7 Chapter Summary

Energy exists in the air particle motion associated with sound. The energy is a square function of sound pressure, and an inverse square function of distance from noise source. It is linearly related to collection area. Various technologies exist for transduction between acoustic and electrical energy, many of which are used in microphonics. Piezoelectric transduction has been identified as the optimal transduction technology due to it's low parasitic properties. Powerful analytical models exist for the modeling of acoustic or mechanical systems as electrical circuits, allowing them to be analyzed by classical circuit techniques such as Thévenin and Norton equivalence and superposition. Such techniques are used for realizing an efficient broadband acoustic energy harvester by matching the source impedance of an electromechanical system with a matched conjugate electrical load. This concept has been explored in the context of sound isolation by the use of piezoelectric PVDF transducers and negative capacitance circuits. Existing acoustic energy harvesting technologies are limited in performance due to diminutive size and lack of efficient broadband harvesting. A piezoelectric film transducer is used for energy harvesting, and the use of negative reactive components are employed for efficient broadband energy harvesting.

Chapter 3

Acoustic Energy Harvester Analysis and Model

This chapter develops an analytical model, describing electromechanical dynamics of the above acoustic energy harvester. The end result is a lumped-element circuit model of a distributed system describing the harvester's mechanical, transduction, and electrical properties. The model is lumped on a modal basis, considering only the first mode of film behavior. This model is instrumental in developing appropriate load circuitry for efficient broadband energy harvesting. The model is then validated experimentally, as described in future sections. The base dynamics model is based on an energy conservation statement. This is later extended to include second-order effects, such as back-cavity reflections.

The total system energy is the sum of energy contributions from kinetic energy, strain energy, and electric field energy. Thus,

$$E_{\text{system, total}} = E_{\text{kinetic}} + E_{\text{strain}} + E_{\text{E field}} \quad (3.1)$$

In the energy analysis, the derivative of system energy equals net power into or out of the system as expressed by

$$\frac{d}{dt}\left(E_{\text{system, total}}\right) = P_{\text{in}} - P_{\text{out}} \quad (3.2)$$
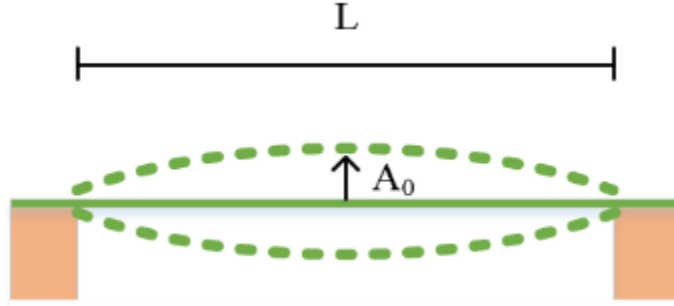
Figure 3.1. Assumed mode shape of PVDF film energy harvester, side view. Length L given in meters and maximum film displacement A_0 also given in meters.

where Pin and Pout are input and output powers, respectively. This can be seen as a conservation of energy statement. Expansion of (3.2) then yields the desired dynamic model.

The analysis begins by examining a square film of piezoelectric PVDF film, and assuming a film shape with only a fundamental mode in each dimension as seen in Figure 3.1. The mode shape is assumed to be

$$A(x, y, t) = A_o(t) \sin\left(\frac{\pi x}{L}\right) \sin\left(\frac{\pi y}{L}\right) \quad (3.3)$$

with L as length of the film (meters) in dimensions x and y, and A_0 the peak modal film displacement for the film's fundamental mode, given in meters.

3.1 Kinetic Energy: Effective Mass M

Kinetic energy of the film is derived by integrating kinetic energy over small volumes of film with dimensions dx,dy. Thus,

$$E_{\text{kinetic}} = \int_0^L \int_0^L \frac{1}{2} \rho T \left(\frac{dA}{dt}\right)^2 dy\,dx \quad (3.4)$$

with film mass density ρ (Kg/m^3), and thickness T (meters). Substitution of (3.3) into (3.4) evaluates to

$$E_{\text{kinetic}} = \frac{\rho T L^2}{8} \left(\frac{dA_0}{dt}\right)^2 \quad (3.5)$$

The power arising from kinetic energy can be evaluated by taking the time derivative of kinetic energy

$$\frac{dA_o}{dt} F_{\text{mass}} = \frac{d}{dt}(E_{\text{kinetic}}) = \frac{d}{dt}\left(\frac{\rho T L^2}{8} \left(\frac{dA_0}{dt}\right)^2\right) = \frac{\rho T L^2}{4} \frac{d^2 A_0}{dt^2} \frac{dA_o}{dt} \quad (3.6)$$

Therefore, the fundamental mode's effective mass M (kilograms) can be seen by inspection as

$$M = \frac{\rho T L^2}{4} \quad (3.7)$$

3.2 Strain Energy: Spring Coefficient K

Based on the assumed film shape in (3.3), spatial derivatives are evaluated as

$$\frac{dA}{dx} = A_0(t) \frac{\pi}{L} \cos\left(\frac{\pi x}{L}\right) \sin\left(\frac{\pi y}{L}\right) \quad (3.8)$$

$$\frac{dA}{dy} = A_0(t) \frac{\pi}{L} \sin\left(\frac{\pi x}{L}\right) \cos\left(\frac{\pi y}{L}\right) \quad (3.9)$$

and film velocity is evaluated as a time derivative through

$$\frac{dA}{dt} = \frac{dA_0(t)}{dt} \sin\left(\frac{\pi x}{L}\right) \sin\left(\frac{\pi y}{L}\right) \qquad (3.10)$$

Strain in x and y are evaluated by integrating over the length of the film, yielding

$$\epsilon_x(y,t) = \frac{1}{L}\int_0^L \sqrt{1 + \left(\frac{dA}{dx}\right)^2}\, dx - 1 \qquad (3.11)$$

$$\epsilon_y(x,t) = \frac{1}{L}\int_0^L \sqrt{1 + \left(\frac{dA}{dy}\right)^2}\, dy - 1 \qquad (3.12)$$

This is approximately equal to

$$\epsilon_x(y,t) \approx \frac{1}{L}\int_0^L \left(1 + \frac{1}{2}\left(\frac{dA}{dx}\right)^2\right) dx - 1 \qquad (3.13)$$

$$\epsilon_y(x,t) \approx \frac{1}{L}\int_0^L \left(1 + \frac{1}{2}\left(\frac{dA}{dy}\right)^2\right) dy - 1 \qquad (3.14)$$

Substituting (3.8) and (3.9) into (3.13) and (3.14) yields

$$\epsilon_x(y,t) = \left(\frac{\pi}{2L}\right)^2 A_0^2(t) \sin^2\frac{\pi y}{L} \qquad (3.15)$$

$$\epsilon_y(y,t) = \left(\frac{\pi}{2L}\right)^2 A_0^2(t) \sin^2\frac{\pi x}{L} \qquad (3.16)$$

The stress-strain relationship for a generic bending material is given by (25)

$$\begin{bmatrix} \epsilon_x \\ \epsilon_y \end{bmatrix} = \frac{1}{E}\begin{bmatrix} 1 & -\nu \\ -\nu & 1 \end{bmatrix}\begin{bmatrix} \sigma_x \\ \sigma_y \end{bmatrix} \qquad (3.17)$$

with Young's Modulus E (Pa), Poisson's ratio ν (unitless), and stress in x and y σ_x and σ_y (Pa).

inverting (3.17) yields stress:

$$\begin{bmatrix} \sigma_x \\ \sigma_y \end{bmatrix} = \frac{E}{1-v^2} \begin{bmatrix} 1 & v \\ v & 1 \end{bmatrix} \begin{bmatrix} \epsilon_x \\ \epsilon_y \end{bmatrix} \qquad (3.18)$$

The total strain energy in a material is given by integrating energy density over the piezoelectric volume [24]. Doing so yields

$$E_{\text{strain}} = \int_0^T \int_0^L \int_0^L \left(\frac{1}{2}\sigma_x\epsilon_x + \frac{1}{2}\sigma_y\epsilon_y \right) dxdydz \qquad (3.19)$$

Substituting (3.15-3.17) into (3.18) and using the result to evaluate the integral in (3.19) yields total strain energy as

$$E_{\text{strain}} = \frac{TEL^2(3+2v)}{8(1-v^2)} \left(\frac{\pi A_o}{2L} \right)^4 \qquad (3.20)$$

The power arising from the stress field is the time derivative of strain energy. Thus,

$$\frac{dA_0}{dt} F_{\text{strain}} = \frac{d}{dt}(E_{\text{strain}}) = \frac{TEL^2(3+2v)}{2(1-v^2)} \left(\frac{\pi}{2L} \right)^4 A_o^3 \frac{dA_0}{dt} \qquad (3.21)$$

This can be understood as a cubic spring, with force being proportional to film displacement cubed. Matching terms to Hooke's law yields an effective cubic spring constant K_{spring} as

$$K_{\text{spring}} = \frac{TEL^2(3+2v)}{2(1-v^2)} \left(\frac{\pi}{2L} \right)^4 \qquad (3.22)$$

where K_{spring} has units of Newtons/meter^3.

At this point, the total forces on the film are a summation from mass and spring forces. Combining (3.21) and (3.6) and evaluating,

$$F_{\text{total}} = \frac{TEL^2(3+2\nu)}{2(1-\nu^2)} \left(\frac{\pi}{2L}\right)^4 A_o^3 + \frac{\rho T L^2}{4} \frac{d^2 A_0}{dt^2} \qquad (3.23)$$

where F_{total} is the total force on the film, in the absence of piezoelectric effects, sources or damping. This can be seen as an undamped mass-spring system.

3.3 E-Field Energy: Electromechanical Transducer Ratio D

For piezoelectric materials the stress-strain relationships include an electric field term arising from the piezoelectric effect and are defined as

$$\begin{bmatrix} \epsilon_x \\ \epsilon_y \end{bmatrix} = \frac{1}{E} \begin{bmatrix} 1 & -\nu \\ -\nu & 1 \end{bmatrix} \begin{bmatrix} \sigma_x \\ \sigma_y \end{bmatrix} + \begin{bmatrix} d_{31} \\ d_{32} \end{bmatrix} E_z \qquad (3.24)$$

with piezoelectric coefficients d_{31} and d_{32} in x and y dimensions (Coulombs/Newton), and electric field E_z in the z direction (Volts/Meter).

In a piezoelectric material, electric displacement D_z (C/m^2) is given by

$$D_z = [d_{31} \quad d_{31}] \begin{bmatrix} \sigma_x \\ \sigma_y \end{bmatrix} + \epsilon E_z \qquad (3.25)$$

where ϵ is the dielectric constant of the piezoelectric material (Farads/meter). Stress in x and y, σ_x and σ_y, can be found by rearranging (3.24) to obtain

$$\begin{bmatrix} \sigma_x \\ \sigma_y \end{bmatrix} = \frac{E}{1-\nu^2} \begin{bmatrix} 1 & \nu \\ \nu & 1 \end{bmatrix} \begin{bmatrix} \epsilon_x \\ \epsilon_y \end{bmatrix} + \frac{E}{1-\nu^2} \begin{bmatrix} 1 & \nu \\ \nu & 1 \end{bmatrix} \begin{bmatrix} d_{31} \\ d_{32} \end{bmatrix} E_z \qquad (3.26)$$

50

Substituting (3.15), (3.16), and (3.26) into (3.25) yields D$_z$ as a function of x and y, according to

$$D_z = \frac{d_{31}E}{1-v}\left(\frac{\pi}{2L}\right)^2 A_0^2(t)\left(\sin^2\frac{\pi x}{L} + \sin^2\frac{\pi y}{L}\right) + E_z\left(\epsilon - \frac{2d_{31}^2E}{1-v}\right) \quad (3.27)$$

The electric field in the z direction is a function of voltage V over film thickness such that

$$E_z = \frac{V}{T} \quad (3.28)$$

Charge Q in Coulombs can be found by integration of the electric displacement Dz over piezoelectric film surface, as described by Gauss's Law, to obtain

$$Q = \int_0^L \int_0^L D_z \, dxdy \quad (3.29)$$

Substituting (3.27) and (3.28) into (3.29) and evaluating yields

$$Q = \frac{L^2V}{T}\left(\epsilon_3 - \frac{2Ed_{31}^2}{1-v}\right) + \frac{A_0^2Ed_{31}\pi^2}{4(1-v)} \quad (3.30)$$

which can be seen as an expression for the total charge Q on the piezoelectric film.

In an open-circuit condition, the net external charge is zero. Therefore, the following expression results:

$$\frac{L^2V}{T}\left(\epsilon_3 - \frac{2Ed_{31}^2}{1-v}\right) = -\frac{A_0^2Ed_{31}\pi^2}{4(1-v)} \quad (3.31)$$

This can be seen by inspection as two terms: a contribution from film deflection Ao arising from the piezoelectric effect, and an effective capacitance arising from the film's dielectric behavior. Differentiating the mechanical contribution with respect to A yields

$$D = \frac{d}{dA_o}\left(\frac{A_o^2 E d_{31} \pi^2}{4(1-v)}\right) = \frac{A_o E d_{31} \pi^2}{2(1-v)} \qquad (3.32)$$

where D is the electromechanical transduction ratio between current and velocity.

3.4 E-Field Energy: Effective Capacitance C

Effective capacitance C can be seen by matching the voltage term in (3.30) to capacitive behavior Q=CV. By inspection, effective capacitance C (farads) is equal to

$$C = \frac{L^2}{T}\left(\epsilon_3 - \frac{2E d_{31}^2}{1-v}\right) \qquad (3.33)$$

The energy contribution arising from the electric field is equal to

$$E_{\text{E Field}} = \frac{1}{2}CV^2 = \frac{1}{2}\frac{L^2}{T}\left(\epsilon_3 - \frac{2E d_{31}^2}{1-v}\right)V^2 \qquad (3.34)$$

3.5 Input Power: Damping B

The damping factor B arises from energy lost to the system due to reflections of the incoming pressure wave off the piezoelectric film. This can be seen by a force balance assertion applied to the film, assuming incoming acoustic wave of pressure p_+ and particle velocity u_+, reflected acoustic wave of pressure p_- and particle velocity u_-, transmitted acoustic wave of pressure q_+ and velocity v_+, and film velocity and pressure defined respectively by U and P, as seen in Figure 3.2.
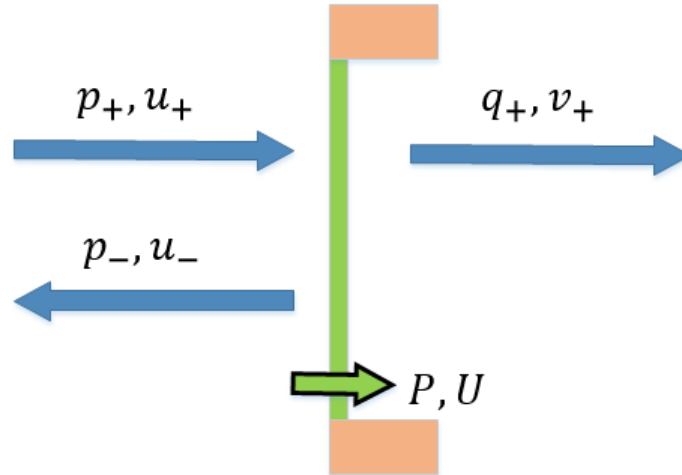
Figure 3.2. Incoming, reflected and transmitted particle velocity and pressure waves, and velocity and force arising from the film.

Conservation of mass on both sides of the film set relationships between incoming, reflected and transmitted particle velocity as

$$U = v_+ \quad (3.35)$$

$$U = u_+ + u_- \quad (3.36)$$

The net pressure P across the film is described by the incoming, reflected and transmitted pressure waves as

$$P = p_+ + p_- - q_+ \quad (3.37)$$

Applying (3.35), (3.36), (3.37) and (2.3), the net pressure evaluates to

$$P = 2Z_0(u_+ - U) \quad (3.38)$$

The instantaneous incoming power is evaluated as the product of pressure and velocity, integrated over the film area:

$$Power_{in} = \int_0^L \int_0^L PU \, dxdy \qquad (3.39)$$

Applying (3.38), (3.39), and (3.10) and evaluating, incoming power can be expressed as

$$Power_{in} = \frac{dA_o}{dt} F = 2Z_0 u_+ \left(\frac{2L}{\pi}\right)^2 \frac{dA_o}{dt} - \frac{Z_0 L^2}{2} \left(\frac{dA_o}{dt}\right)^2 \qquad (3.40)$$

This can be seen to have two contributions to system net power input/output: a power input arising from the incoming pressure wave, and a power output (loss, dampening term) arising from reflection and radiation of acoustic waves. By inspection, the damping term B can be fit to the classical damping model F=BdAo/dt as

$$B = \frac{Z_0 L^2}{2} \qquad (3.41)$$

3.6 Input Power: Source F

The input power source F can be seen from the net system power input/output in expression (3.40). By inspection, the term arising from the incoming pressure wave is:

$$F = 2Z_0 u_+ \left(\frac{2L}{\pi}\right)^2 = \left(\frac{8L^2}{\pi^2}\right) p_+ \qquad (3.42)$$

It is noted that in this harvester design, it is impossible to harvest all incoming energy incident on the harvester. This is due to the film's constrained boundaries, which prevent the film from displacing equally over the entire film area. Due to this, energy cannot be optimally extracted over the entire film area simultaneously. As a result, the maximum efficiency possible with this harvester design is $64/(\pi)^4$, or approximately 66%. This distributed parameter is captured in the lumped element parameter as the $8/\pi^2$ term in (3.42).

3.7 Transmission Line: Back-cavity effect

To address performance degradation associated with diffraction effects as discussed in Section 2.3, the piezoelectric PVDF film is supported with an enclosure on one side, creating a cavity as seen in Figure 3.3. A constant pressure inside the cavity provides a pressure reference point for acoustic forces acting on the film.

The back cavity also applies a force on the harvester film due to acoustic waves launched by the film's motion reflected at the rear of the cavity, and interacting with the film. The analysis is performed assuming a one-dimensional transmission line, similar to classical quarter-wave resonators. Consider the film and enclosure system as a transmission line of length Δ (meters), as
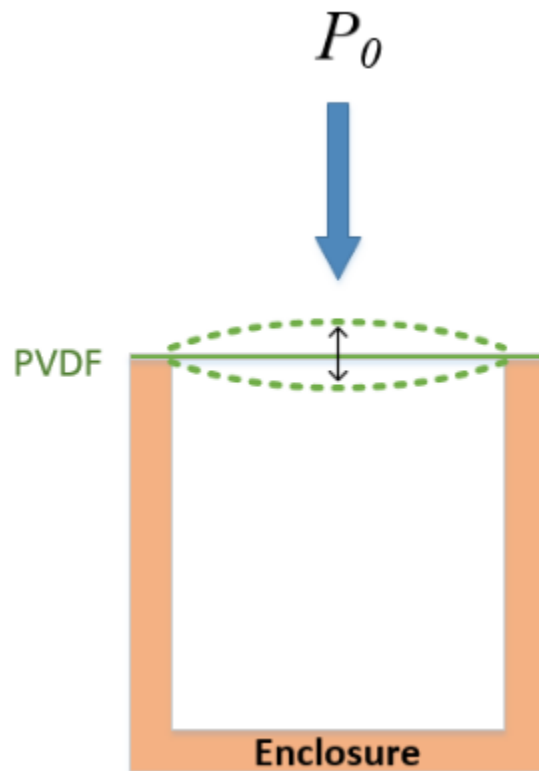
Figure 3.3. The harvester is enclosed, addressing performance loss associated with diffraction effects.
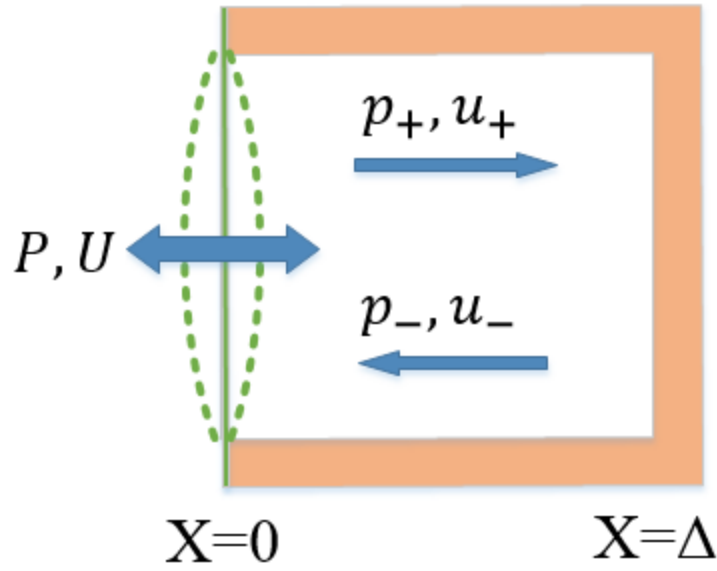
Figure 3.4. Film with velocity U and pressure P. Back cavity of length D. Launched pressure and velocity waves p+ and u+, and reflected pressure and velocity waves p- and u-.

seen in Figure 3.4. The film's velocity and pressure are given as U and P, respectively. Launched pressure and velocity waves are given as p_+ and u_+, respectively. Reflected pressure and velocity waves are given as p_- and u_-, respectively.

Pressure and velocity waves are expressed in time-harmonic form as

$$u_+ = \hat{u}_+ e^{j(\omega t - kx)} \qquad (3.43)$$

$$u_- = \hat{u}_- e^{j(\omega t + kx)} \qquad (3.44)$$

$$p_+ = Z_o \hat{u}_+ e^{j(\omega t - kx)} \qquad (3.45)$$

$$p_- = -Z_o \hat{u}_+ e^{j(\omega t + kx)} \qquad (3.46)$$

with frequency ω in radians/second, time t in seconds, k wavenumber in radians/meter, distance

x in meters, and acoustic impedance Z_o in Pascals/meter/second.

Applying boundary conditions at X= Δ (zero particle velocity) results in the following:

$$\hat{u}_- = -\hat{u}_+ e^{-2jk\Delta} \qquad (3.47)$$

Applying boundary conditions at X=0, the sum of the medium's launched and reflected particle

velocities must equal the film's velocity

$$U = \hat{u}_+ + \hat{u}_- = \hat{U}e^{j\omega t} \qquad (3.48)$$

Therefore,

$$\hat{u}_+ = \frac{\hat{U}}{1-e^{-2jk\Delta}} \qquad (3.49)$$

$$\hat{u}_- = \frac{-\hat{U}e^{-2jk\Delta}}{1-e^{-2jk\Delta}} \qquad (3.50)$$

Applying pressure boundary conditions at X=0,

$$P = p_+ + p_- = Z_o(\hat{u}_+ - \hat{u}_-) = \hat{p}e^{j\omega t} \qquad (3.51)$$

Therefore, combining (3.49-3.51), pressure arising from the reflected wave is found to be:

$$\hat{p} = \frac{Z_o\hat{U}}{j}\cot(k\Delta) \qquad (3.52)$$

Scaling pressure by film area L^2 and substituting wavenumber $2\pi/\lambda$ yields the final expression

for the back cavity's force contribution as

$$\hat{f} = \frac{Z_o L^2 \hat{U}}{j} \cot\left(\frac{\omega\Delta}{c}\right) \quad (3.53)$$

with speed of sound c in m/s.

An acoustic compliance applies a force:

$$f = U \frac{K}{j\omega} \qquad (3.54)$$

With spring constant K, in Newtons/meter. Combining (3.53) and (3.54) and matching terms, the force arising from the back cavity can be understood as a frequency-dependent compliance:

$$K_{\text{cavity}} = Z_o \omega L^2 \cot\left(\frac{\omega\Delta}{c}\right) \qquad (3.55)$$

Such an impedance characteristic presents as a compliance at certain frequencies and a mass at other frequencies. This effect could be mitigated by application of an acoustic absorbing material in the cavity, such as sound absorbing foam. This would have the effect of reducing the quality factor of the cavity's resonances. However, the benefit would be negligible at the frequencies of interest (100-1000Hz), where the wavelengths of interest are very long compared to the cavity's geometries.

The effect of the back cavity's transmission line can equivalently be understood in the time domain. This can be seen by the inverse Fourier transform of (3.47), which is

$$u_-(t) = -u_+\left(t - \frac{2\Delta}{c}\right) \qquad (3.56)$$

or that u₋ is equal to u₊ delayed by the round trip transit time over the depth of the cavity, with a negation resulting from the end-of-cavity reflection. Combining (3.48) and (3.56) yields the time-domain velocity component arising from the back cavity, such that

$$U(t) = u_+(t) - u_+\left(t - \frac{2\Delta}{c}\right) \qquad (3.57)$$

with parameters given as before. Combining (3.56) and (3.51) yields the time-domain pressure component arising from the back cavity, such that

$$P(t) = Z_0\left(u_+(t) + u_+\left(t - \frac{2\Delta}{c}\right)\right) \qquad (3.58)$$

Combining (3.57) and (3.58) yields the pressure as a function of film displacement, which when scaled by film area yields the total force being imparted on the film. Thus,

$$F_{\text{cavity}}(t) = L^2 Z_0\left(U(t) + 2u_+\left(t - \frac{2\Delta}{c}\right)\right) \qquad (3.59)$$

where U(t) is film velocity and is equal to dA₀/dt, and u₊, the velocity wave launched by the film is determined recursively from previous film states such that

$$u_+(t) = U(t) + u_+\left(t - \frac{2\Delta}{c}\right) \qquad (3.60)$$

and the initial film state U(t) is assumed to be zero for all time t < 0.

3.8 Linearization: DC bias pressure effect

As was discussed in Section 3.3, the electromechanical transducer ratio D is a linear function of film displacement Ao. When the film has a higher displacement Ao, it's transduction

performance improves. This has the benefit of reduced voltages electrically for a given force, and reduced losses. Therefore, it is beneficial to apply a DC bias to the film displacement. This is implemented as a DC bias pressure applied across the film, realized as a partial vacuum in the film's enclosure. The input power arising from such a force can be found by

$$Power_{\text{bias}} = \int_0^L \int_0^L P_b \frac{dA}{dt} \sin\left(\frac{\pi x}{L}\right) \sin\left(\frac{\pi y}{L}\right) dy dx = P_b \left(\frac{2L}{\pi}\right)^2 \frac{dA}{dt} \quad (3.61)$$

where Power$_{\text{bias}}$ is power in watts and P_b is bias pressure, in Pascals.

The force resulting from this power is understood as

$$F_{\text{bias}} = \frac{4P_b L^2}{\pi^2} \quad (3.62)$$

This force is a DC bias force and thus only acts against the film's effective spring to produce a DC bias displacement. Equating (3.62) to the spring's force (3.21), substituting (3.22) and solving for Ao yields static bias displacement

$$P_o = \sqrt[3]{\frac{P_b \left(\frac{2L}{\pi}\right)^2}{K_{\text{spring}}}} \quad (3.63)$$

where Po is seen as the DC component of film displacement in meters.

The effective transducer windings ratio D, given in (3.32) is a function of film displacement Ao. Assuming the film displacement arising from acoustic forces is a small signal when compared to the bias displacement, the bias displacement is a "large signal". Therefore, the system is linearized using a first-order Taylor expansion around the film's DC operating point Po. This yields

60

$$D_{\text{eff}} = \frac{P_o E d_{31} \pi^2}{2(1-v)} \qquad (3.64)$$

The bias pressure also applies a pre-stress term to the film, affecting the spring constant. This allows the system's resonant frequency to be tuned through the application of a bias pressure. Applying the same small-signal assumption, the force (3.21) arising from the spring can be linearized as a first-order Taylor expansion, evaluated at the operating point Po:

$$F_{\text{strain}} = 3K_{\text{spring}} P_o^2 A_o \qquad (3.65)$$

Therefore the linearized spring constant arising from DC bias pressure can be understood as:

$$K_{\text{eff}} = 3P_o^2 K_{\text{spring}} \qquad (3.66)$$

This linearized spring constant is a second-order function of static film displacement Po. Bias pressure P_b was chosen to yield film resonance at approximately 1KHz, while improving transduction ratio D.

3.9 Model adjustments

A real-world system has certain implementation-related parasitic properties and other variations from the above idealized model. These deviations are modeled to the best extent possible for optimal performance.

3.9.1 Air Mass

In a real, physical system there is a near-field boundary of air near the film, which moves in association with the film's movement. The inertial force arising from this air layer adds to the

effective mass of the acoustic system. Assuming a boundary layer of the same dimensions as the film and having thickness H_{air}, applying the analysis used in Section 3.1 results in the following contribution to mass:

$$M_{air} = \frac{\rho_{air} H_{air} L^2}{4} \quad (3.67)$$

where ρ_{air} is air density (Kg/m^3) and H_{air} is thickness of the air layer in meters. The total system mass is the sum of the two mass contributions. Thus,

$$M_{eff} = M + M_{air} \quad (3.68)$$

In practice the mass contribution from the air is minimal, less than 5% of the total mass in the implemented design.

3.9.2 Electrode Capacitance

In a real system, the area of the piezoelectric film is larger than the part which is moving due to acoustic forces. Extra film is needed for electrical connection, and to support the film mechanically. This portion of film is constrained and does not contribute meaningfully to harvesting action, but does contribute to the film's capacitance. This capacitance can be modeled as a parallel plate capacitor, with capacitance equal to

$$C_{elec} = \frac{\epsilon_3 A_{elec}}{T} \quad (3.69)$$

where C_{elec} is electrode capacitance in farads, and A_{elec} is the area of the extra film portion, in square meters. Because this capacitance appears in parallel to the harvester's capacitance, the effective capacitance is the sum of these two capacitances. Thus,

$$C_{\text{eff}} = C + C_{\text{elec}} \qquad (3.70)$$

where C_{eff} is the effective system capacitance in Farads. In practice this capacitance contributes meaningfully to the system capacitance, accounting for approximately 40% of total capacitance in the implemented design.

3.9.3 Transmission Line Length

The force term arising from the transmission line derived in Section 3.7 is highly sensitive to the cavity depth, Δ. The transmission line length was assumed to be equal to the depth of the cavity, resulting from a flat film. However, in reality the film is curved inwards due to the bias pressure, reducing the effective transmission line length. The new effective cavity depth arising from this is given by

$$\Delta_{\text{eff}} = \Delta - \frac{P_o}{2} \qquad (3.71)$$

where Δ_{eff} is effective transmission line length, in meters. In practice this adjustment has a minor effect, adjusting resonant frequencies by less than 5% in the implemented design.

3.10 Complete Model and Circuit Analogy

The complete nonlinear, time-domain dynamics model for the harvester's open-circuit behavior can be seen in terms of changes in system stored energy, as in (3.2). Substituting (3.1), (3.5), (3.20), (3.34), and (3.40) into (3.2), and applying adjusted component values seen in Section 3.9, yields

$$\frac{d}{dt}\left(\frac{M_{\text{eff}}}{2}\left(\frac{dA_0}{dt}\right)^2 + \frac{K_{\text{spring}}}{4} A_o^4 + \frac{1}{2} C_{\text{eff}} V^2 \right) = \tilde{F}\frac{dA_o}{dt} - B\left(\frac{dA_o}{dt}\right)^2 \qquad (3.72)$$

which can be seen as a measure of total system energy, as well as it's inputs and outputs. This model omits the force contribution arising from the back cavity, which is considered separately as a force. Evaluation of (3.72) and algebraic manipulation yields a pair of coupled differential equations:

$$F_{\text{cavity}} + M_{\text{eff}}\frac{d^2 A_o}{dt^2} + B\frac{dA_o}{dt} + K_{\text{spring}}A_o^3 + DA_oV = \tilde{F} \quad (3.73)$$

$$DA_o\frac{dA_o}{dt} = C_{\text{eff}}\frac{dV}{dt} \quad (3.74)$$

with independent variables V as film voltage and A_o as peak film displacement, and variables F_{cavity}, M_{eff}, B, K_{eff}, D_{eff}, F, and C_{eff} as derived in Sections 3.1-3.9. Arguments as made in Section 3.8 apply a linearization to (3.73) and (3.74), resulting in

$$F_{\text{cavity}} + M_{\text{eff}}\frac{d^2 A_o}{dt^2} + B\frac{dA_o}{dt} + K_{\text{eff}}A_o + D_{\text{eff}}V = \tilde{F} \quad (3.75)$$

$$D_{\text{eff}}\frac{dA_o}{dt} = C_{\text{eff}}\frac{dV}{dt} \quad (3.76)$$

where effective spring constant K_{eff} (3.66) and effective transduction ratio D_{eff} (3.64) result from first-order Taylor approximations of their nonlinear expressions, evaluated at the DC operating point Po (3.63). An equivalent circuit model incorporating (3.75), (3.76) and the force contribution arising from the back cavity (3.53) is seen in Figure 3.5. A table with parameters used in the model can be found in Table 3.1. The corresponding lumped element model values are seen in Table 3.2.
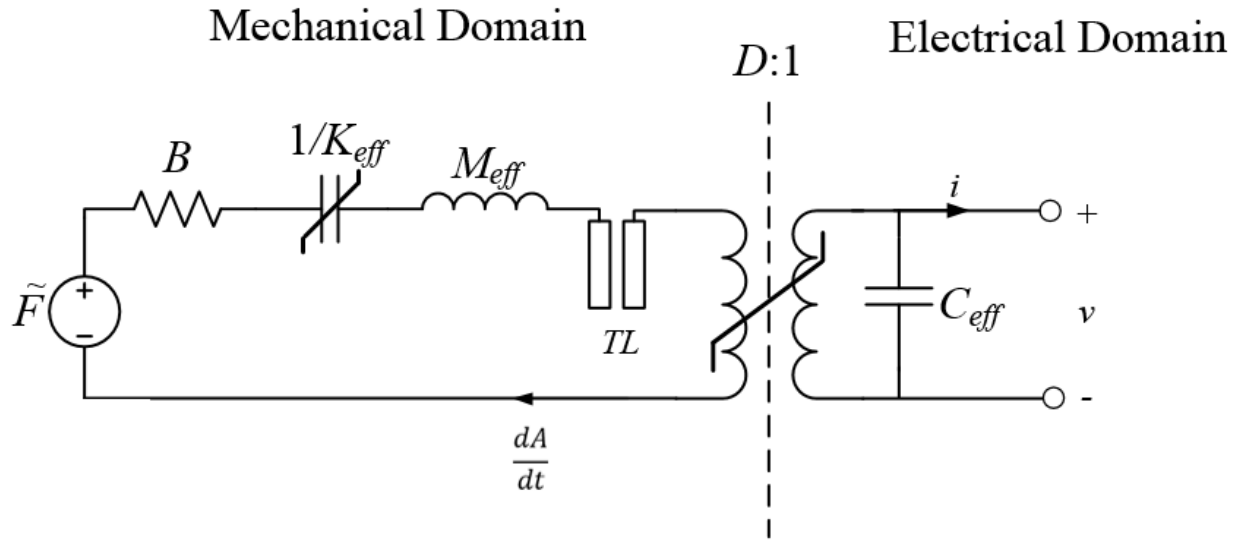
Figure 3.5. Equivalent electromechanical circuit model of film dynamics in open circuit.

Parameter	Description	Value	Units
F	Input Pressure	Independent	dB SPL
L	Film edge length	0.1	M
T	Film Thickness	110	uM
P_b	Bias Pressure	10	KPa
Δ	Cavity Depth	0.09	M
H_{air}	Thickness of air layer	6.35	mm
A_{elec}	Area of Electrode	0.00889	M^2
P_{atm}	Atmospheric Pressure	101.325	KPa
T_{air}	Atmospheric Temperature	20	C
E	PVDF Young's Modulus	2.5	GPa
ν	PVDF Poisson's Ratio	0.3	unitless
d31	PVDF Piezoelectric Coefficient	23	pC/N
ε_3	PVDF relative dielectric constant	11	unitless
R_{piezo}	Equivalent Resistance of electrodes	100	mOhm
ρ	PVDF mass density	1780	Kg/M^3
γ	Adiabatic Constant, Air	1.4	unitless
R_{sp}	Specific Gas Constant, Air	287.058	J/(Kg*K)

Table 3.1. Parameters used in acoustic energy harvester model.

Parameter	Description	Value	Units
M_{eff}	Effective Mass	516.5	g
B	Damping Factor	2.069	Ω
D_{eff}	Effective Windings Ratio	2.0125	unitless
C_{eff}	Effective Capacitance	16.37	nF
K_{eff}	Effective Spring Constant	24.489	kN/m
Po	Film Bias Point	4.96	mm

Table 3.2. Effective parameters resulting from linearized harvester model.

3.11 Higher Mode Considerations

The above analysis only considers the fundamental mode of film behavior by assuming the film shape in (3.3). Other solutions exist to the set of boundary conditions imposed by the film's constrained edges. These solutions manifest as higher order film modes in dimensions x and y, which occur at higher frequencies than the fundamental film mode derived above. Given parameters seen in Table 3.2, the film resonates at a fundamental frequency of approximately 1KHz. The frequencies of interest being below this (100-1000Hz), the fundamental mode dominates film behavior and higher frequency modes can therefore be neglected with minimal error at low frequencies. As a result of this, modeled and experimental spectra will deviate at high frequencies, manifesting as extra peaks and nulls in film response above 1KHz.

3.12 Chapter Summary

An energy-based fundamental analysis of the acoustic energy harvester's dynamics is derived for open-circuit conditions. This model is a lumped-parameter model based on the first mode shape, and mapped onto an equivalent circuit model. The dynamics of the system are nonlinear; a cubic spring and bias-dependent transformer terms exist. A DC bias point is

provided in film deflection via a static pressure, improving performance and allowing for small-signal analysis to linearize the system. The model is updated to account for real-world deviations from an idealized model, such as electrode capacitance and air mass.

Chapter 4

Acoustic Energy Harvester Mechanical Design

The mechanical design and fabrication of an acoustic energy harvester design are presented. The harvester is designed according to the basic assumptions made in the harvester model (Chapter 3). This includes a square piezoelectric film suspended over a cavity, with a bias provided by a partial vacuum in the cavity. In future chapters the harvester is fabricated and characterized experimentally, validating the analytical model. The harvester design allows for large-scale implementation with collection area of $100cm^2$, with the potential for further scaling in future work.

An idealized conceptual view of the acoustic energy harvester device was presented in Figure 3.3 and is repeated here in Figure 4.1. The harvester is based on poled piezoelectric Polyvinylidiene Fluoride (PVDF) film of 110um thickness. The PVDF film (TE Connectivity) is metallized on both sides with Nickel/Copper emulsion for electrodes. The film is suspended over an acrylic enclosure in a manner similar to a drum. An incoming acoustic pressure wave displaces the film, causing it to deflect mechanically and generate a charge via the piezoelectric effect. Proper electronic loading then harvests power.
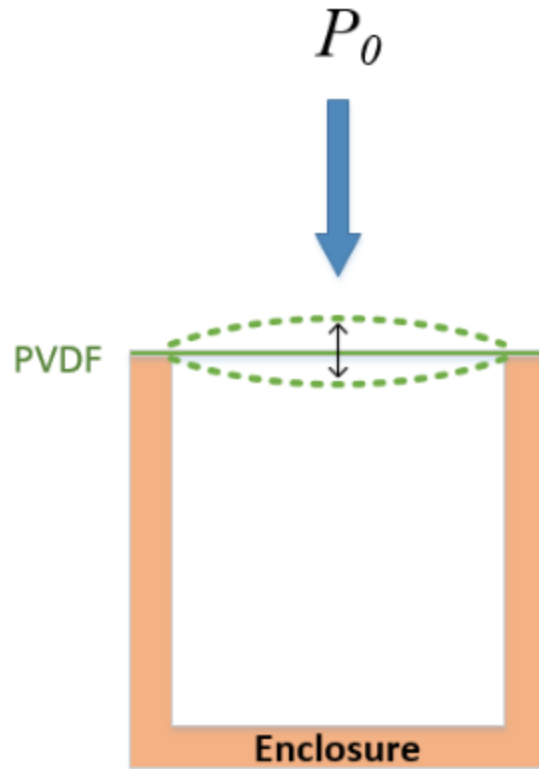
Figure 4.1. Idealized side-view schematic of the acoustic energy harvester to be fabricated.

An exploded mechanical view of the designed harvester is seen in Figure 4.2. The realized implementation is seen in Figure 4.3. The PVDF film has a square active area of 10cm x 10cm, or 100cm^2. The film is suspended over a cavity of milled acrylic, having a depth of 9cm. The film is held in place by a frame of ¼ inch thick milled acrylic with eight screws, and a rubber o-ring to maintain vacuum. Circular magnets contact the film in a mechanically constrained area, providing low contact resistance electrodes for connection to the control electronics (see Chapter 5).
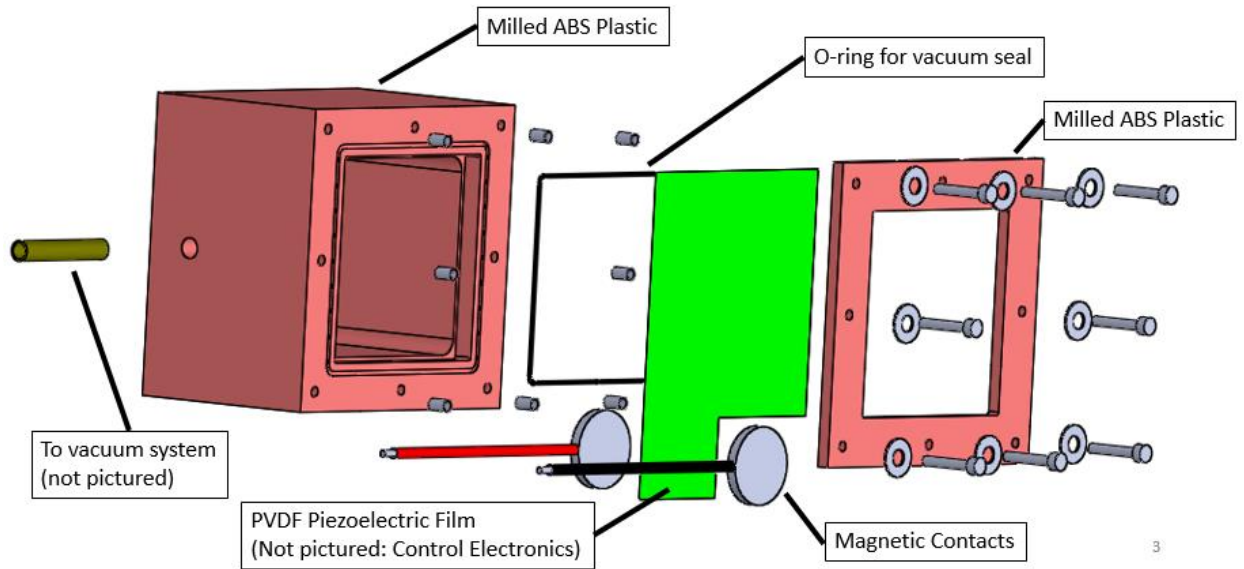
Figure 4.2. Exploded mechanical view of acoustic energy harvester design, with various design components labeled.

Figure 4.3. The realized Acoustic Energy Harvester design.

Behind the PVDF film is a milled cubic cavity, measuring 9cm in depth. The cavity is necessary to mitigate diffraction effects, as discussed in Chapter 3. Inside the cavity is a partial vacuum of 10 kPa, referenced to atmospheric pressure outside the cavity. Therefore, a 10 kPa static pressure is held across the film. This has the effect of improving performance and linearizing the system, as discussed in Section 3.8. The vacuum is maintained by a rubber o-ring and vacuum system seen in Figure 4.2. A detailed diagram of the vacuum system is seen in Figure 4.4. A port leading from the harvester's cavity passes through a valve, pressure gauge and hand pump. This generates and maintains the DC pressure differential across the film. The leakage in the vacuum system was determined experimentally to be approximately 200 Pa per hour. While not ideal for real-world settings, this is more than adequate for experimental settings.
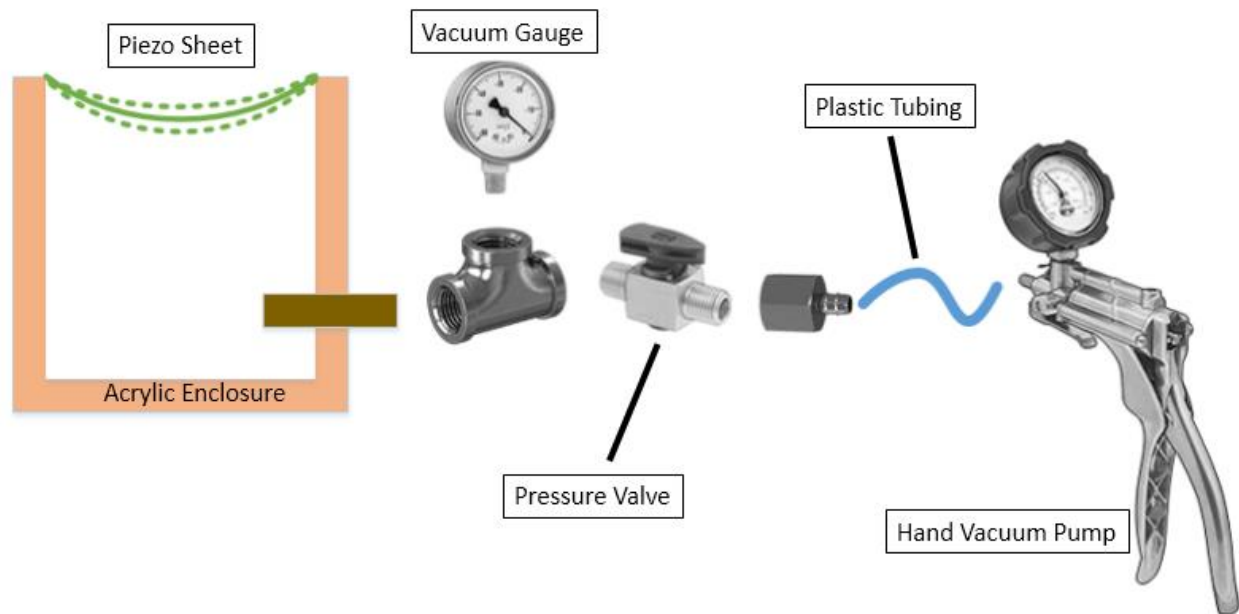
Figure 4.4. Diagram of pressure system, designed to produce a partial vacuum in the harvester's cavity, and thus DC bias pressure across the film.

In summary, a mechanical design is presented for large-scale acoustic energy harvesting, with an active area of 100cm^2. The design enables the possibility of scaling further in the future. The design is based on a cube of acrylic, which is milled to produce a back-cavity. The film is suspended over the cavity and constrained mechanically between the acrylic base and an acrylic frame. The film is contacted electrically by two magnetic electrodes, which lead to load electronics. A vacuum system comprising of a hand vacuum pump, vacuum gauge and valve produce the DC bias pressure resulting from a vacuum in the harvester's cavity. An o-ring between the film and acrylic base provides a vacuum seal.

Chapter 5

Electrical Design

This chapter presents the design of the electrical system to load the AEH in a manner which most optimally extracts energy. The electrical design is informed by the electromechanical AEH model derived in Chapter 3. This model is simplified into a Thévenin equivalent model, exploiting a number of assumptions and approximations. As discussed in Section 2.5, energy is most optimally extracted at a given frequency when the harvester is loaded with a conjugate matched load at that frequency. Energy is extracted most optimally at any frequency which a conjugate match load is presented; broadband energy harvesting is achieved when such a load exists over a broad frequency range. An analog circuit is implemented to achieve this with a focus on efficient harvesting over 50Hz-1000Hz, corresponding with the aircraft noise spectrum seen in Figure 2.1. The load is implemented using operational amplifier circuitry. The energy losses incurred in this implementation exceed the energy harvested, and harvested energy is intentionally spent in a load resistor. However, in future incarnations an equivalent load could be implemented using more efficient circuitry, resulting in net energy profit. An operational amplifier circuit architecture was chosen for it's rapid prototyping benefits purely to validate the conceptual basis behind broadband energy harvesting.

5.1 Simplified Thévenin Source Model

An analytical model for the AEH device was derived in Chapter 3, culminating in a

dynamics model and equivalent electromechanical linear circuit model presented in Section 3.10.

As discussed in Section 2.5, using standard linear circuit techniques such a circuit can be

decomposed into a Thévenin equivalent model with a frequency-dependent voltage source V_t,

reactance X_t and resistance R_t. Frequency-dependent values for V_t, X_t, R_t and quality factor Q are

seen in Figure 5.1, based on a driven input of 75 dB SPL, which is roughly equivalent in

amplitude to a loud talking level.
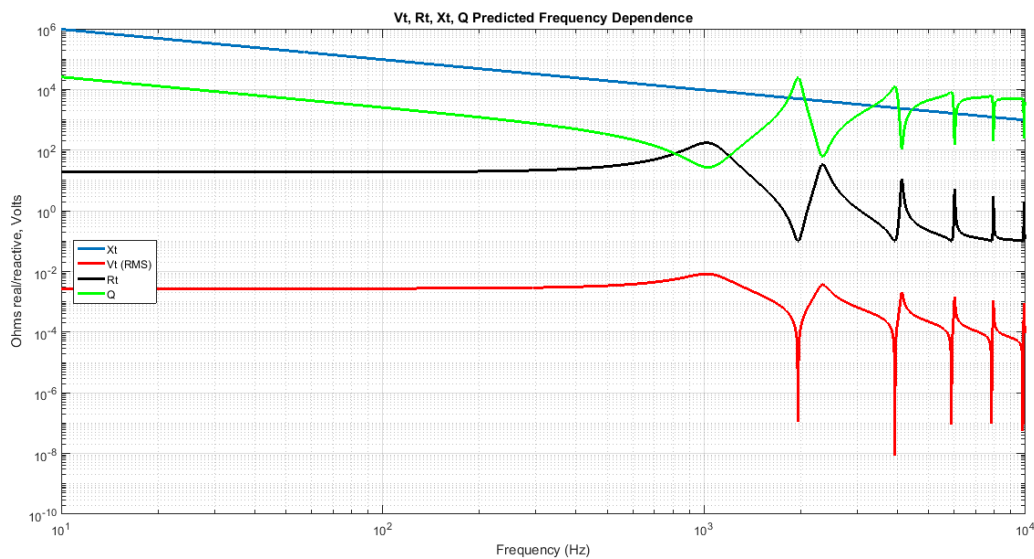
Figure 5.1. Thévenin equivalent Voltage V_t, Reactance X_t, Resistance R_t and quality factor Q,

based on the AEH linearized electromechanical circuit model at a driven input of 75 dB SPL.

74
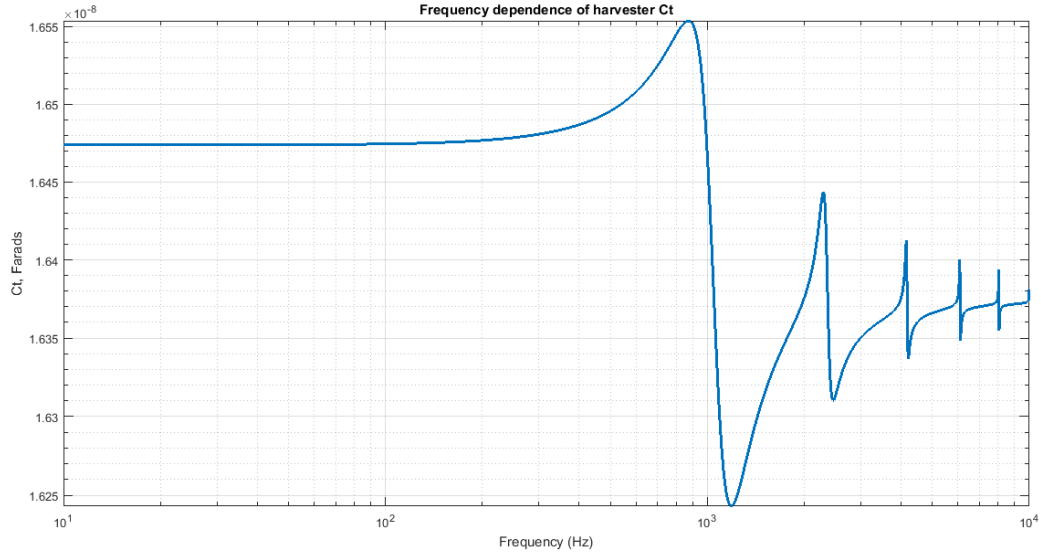
Figure 5.2. Frequency dependence of harvester's equivalent series capacitance Ct.

Over the target frequency range for energy harvesting (50-1000Hz), a number of approximations can be made. As can be seen in Figure 5.1, V_t and R_t are nearly constant at 2.7 mV rms and 18.8 ohms, respectively, over this frequency range. Furthermore, X_t is largely capacitive in nature, with an impedance characteristic closely resembling that of a capacitor with capacitance 16.47 nF, as can be seen in Figure 5.2. This is consistent with the following intuitive arguments.

1. The inductor modeling mass M has an impedance which is negligible at low frequencies and can therefore be ignored.
2. The transmission line appears capacitive in nature well below it's λ/4 resonance frequency (~1KHz) and can therefore be modeled as a capacitor.

75

Applying these arguments to the linearized electromechanical circuit model in Figure 3.5 and reflecting circuit components through the transformer results in the model seen in Figure 5.3a, where K_{TL} is the equivalent compliance presented by the transmission line. This is further simplified using Thévenin equivalence into the final simplified model, seen in Figure 5.3b, where V_t R_t and C_t taken as before. This is the model used in circuit design for broadband impedance matching, where Vt = 2.7 mv rms, Rt = 18.8 ohms and Ct = 16.47nF.
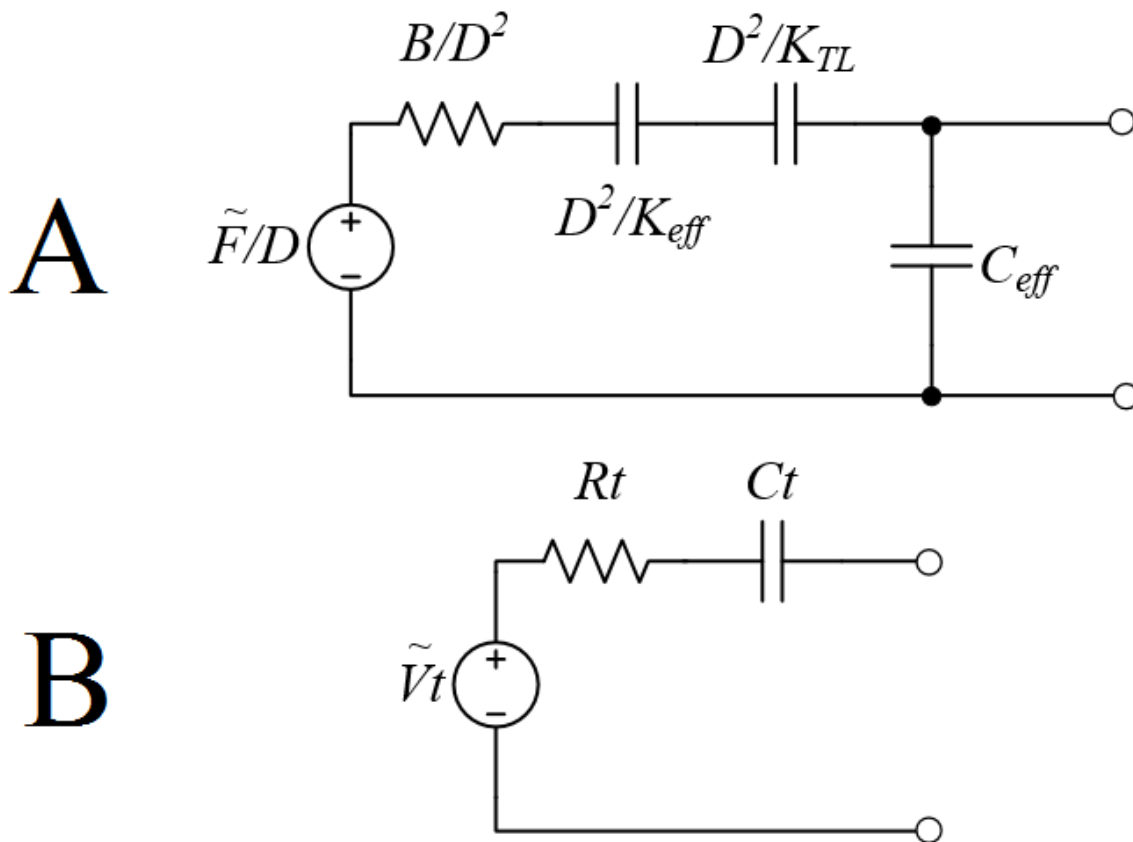
Figure 5.3. (a) simplified Thévenin equivalent AEH electromechanical model. (b) Thévenin equivalent model, further simplified.
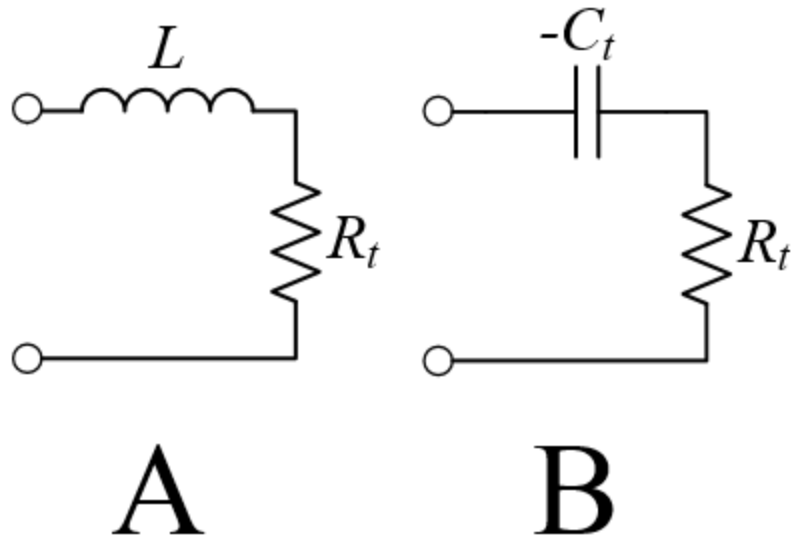
Figure 5.4. (a) Matched conjugate load implementing optimal energy harvesting at a single

frequency using a matched resistor and resonant inductor. (b) Matched conjugate load

implementing optimal broadband energy harvesting using a matched resistor and negative

capacitor.

As discussed in Section 2.5, efficient energy harvesting occurs at any frequency where

the harvester is loaded with an impedance which is the complex conjugate of the source

impedance seen in Figure 5.3b. Conceptually this load consists of a matched resistance R_t and an

impedance which is the negation of C_t's impedance. Such a load can be implemented over a

narrow frequency range using a matched load resistor R_t and series load inductor L as seen in

Figure 5.4(a), where L is sized to resonate with Ct at the desired frequency, canceling out

reactance near the resonant frequency.

A complex conjugate load can also be implemented using the circuit load seen in Figure

5.4b, consisting of a matched resistor R_t and a negative capacitor C_t. This circuit has the benefit

of achieving optimal energy harvesting over a broad frequency range, rather than the narrowband

harvesting produced by the circuit in Figure 5.4a. For this reason, the load seen in Figure 5.4b was chosen for this work. The simplified model shown in Figure 5.3b, while effective for impedance matching considerations, does not capture resonance details and sensitivity to parasitic resistances necessary for stability analysis. Therefore the full, detailed harvester model is used in the stability analysis seen in Section 5.4.

5.2 Parameter Sensitivity Considerations

In the impedance matching scheme described above, optimal broadband energy harvesting is achieved when the load capacitor is equal in value to $-C_t$, where C_t is the Thévenin source equivalent capacitance, and the load resistor is equal to R_t, the Thévenin source resistance. As derived in Chapter 3, R_t and C_t are functions of the harvester and environmental parameters. The parameters used in this work are seen in Table 3.1. If the load R_t and C_t are designed for a certain set of harvester and environmental parameters, any deviation from these parameters will alter the source impedance, degrading broadband energy harvesting performance. Therefore, it is instructive to understand the sensitivity of harvesting performance to these parameters.

The harvester and environmental parameters are divided broadly into two categories. One set of parameters includes those which are unknown, or are known with some uncertainty but fixed and measurable. This includes nearly all of the parameters, excepting those discussed below. It is assumed that these parameters are measured and accounted for in the load design process, eliminating the effect of their uncertainty. The second set of parameters includes those which are unknown and variable over time. This primarily includes ambient air temperature T_{air} and pressure P_{atm}. Cavity bias pressure P_b is an independent design parameter, however it has the

potential to vary over time due to imperfections in the vacuum system and sealing, and changes in atmospheric pressure. Therefore it is included in this set. The sensitivity of harvested energy to these parameters is analyzed, using a 747-400 noise spectrum as the driving source. The parameters are varied one at a time, while keeping all others fixed. The load is fixed between experiments, set to be an optimal match at the nominal conditions. This simulates real-world conditions where the load is set at design time for an optimal impedance match and remains constant in the presence of environmental conditions, perturbing the optimal impedance match.

A plot of harvested energy versus environmental air temperature is seen in Figure 5.5. A change of less than 4% over the entire expected temperature operating range indicates a low sensitivity to air temperature.
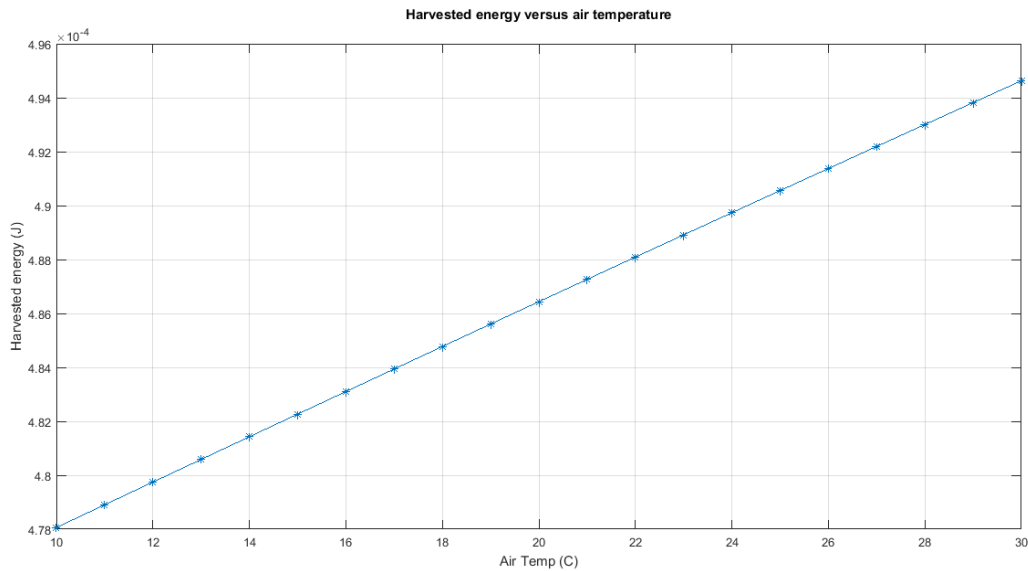
Figure 5.5. Harvested energy versus environmental air temperature.

A plot of harvested energy versus ambient air pressure is seen in Figure 5.6. A change in harvested energy of 25% over the expected operating air pressure range of 95 kPa – 1050 kPa
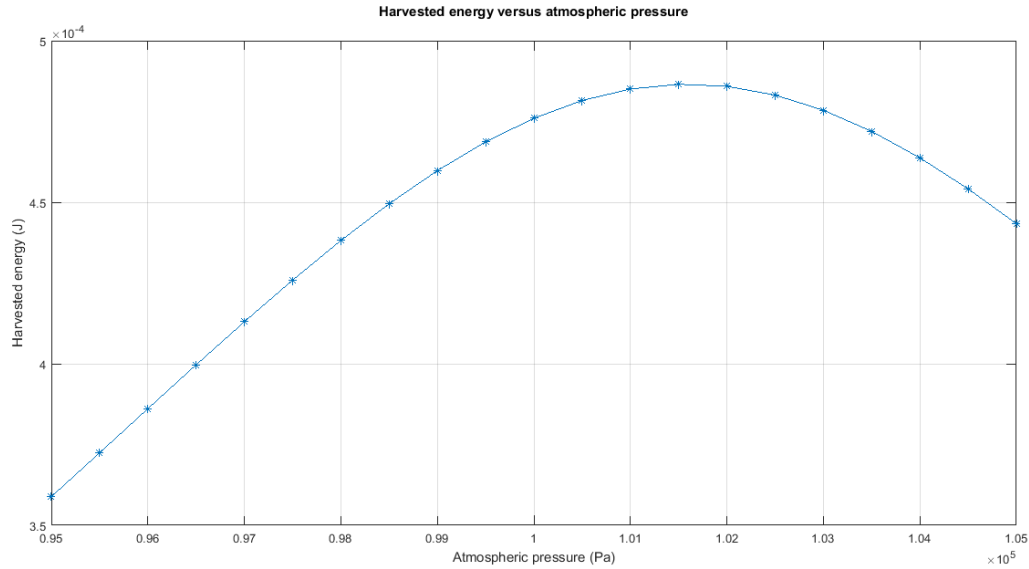
Figure 5.6. Harvested energy versus atmospheric pressure.

indicates relatively low sensitivity to barometric air pressure. With air pressure most commonly

falling over an even narrower range, the expected variance in harvested energy is even lower.

A plot of harvested energy versus cavity bias pressure is seen in Figure 5.7. A change in

harvested energy of 12% over an expected uncertainty of Pbias from 9.5 kPa - 10.5 kPa indicates

low sensitivity to bias pressure.

Low sensitivity of harvested energy to the time-variant parameters indicates that the

harvester's design is robust to expected environmental changes during long-term use. All other

parameters are fixed in value and while they may have some level of uncertainty, the effect of

the uncertainty can be tuned out in the initial design phase.

One other design sensitivity that is instructive to highlight is the sensitivity to load

capacitance Ct, given a fixed harvester and environmental conditions. This sensitivity is a

measure of the allowable variability in load capacitance before an unacceptable amount

80
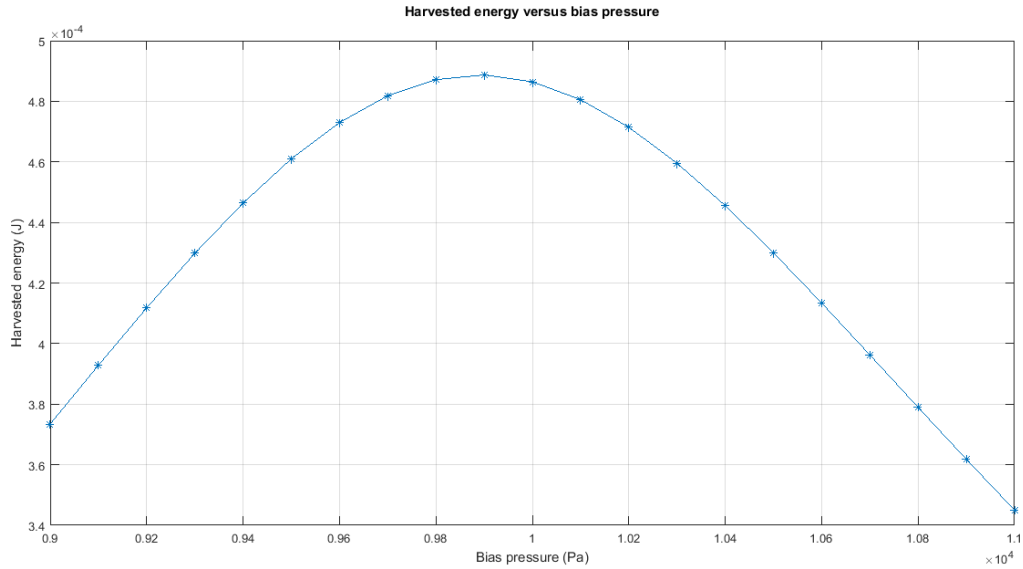
Figure 5.7. Harvested energy versus bias pressure.

of energy is lost. The sensitivity of harvested energy to load capacitance is seen in Figure 5.8, which indicates an extremely high sensitivity to load capacitance. A load capacitance 20pF away from the target capacitance reduces the quality of the impedance match, reducing harvested power to 10% of it's maximum value. This results in a constraint on load capacitance to be within approximately 0.1% of the target value. This sensitivity is consistent with that widely reported in literature [18],[19],[20],[21],[23],[24], using PVDF and negative capacitance for noise isolation applications. As will be seen in Section 5.4, a load capacitance that is too low results in an unstable system with negligible energy harvesting. These two constraints result in a 20pF (0.1%) window of load capacitance for acceptable behavior. Such a constraint is a challenge, especially given the 10% tolerance typical of real-world capacitors.
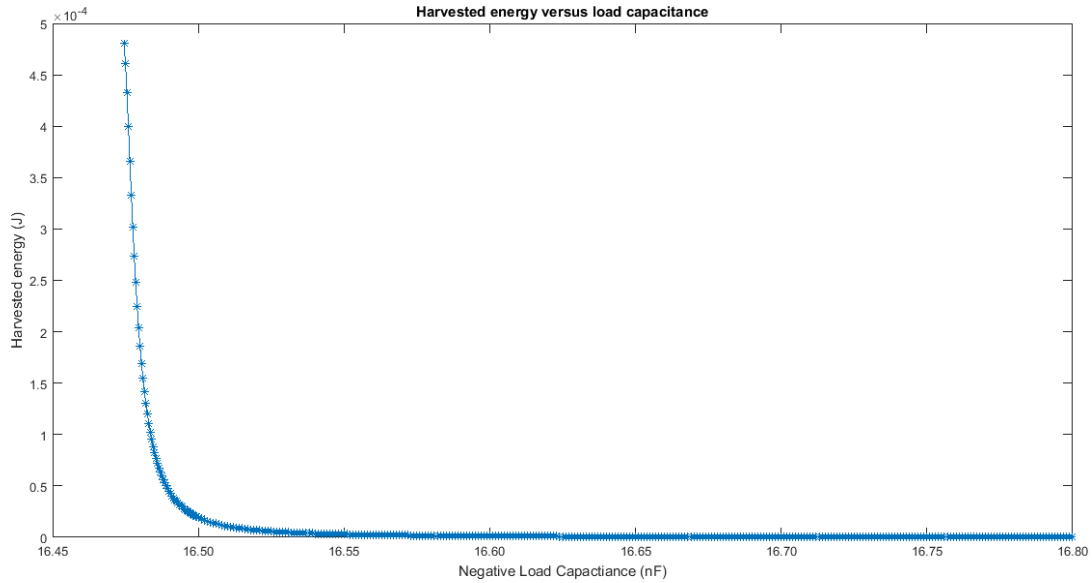
Figure 5.8. Harvested energy versus load capacitance.

5.3 Analog Design for Conjugate Load

This section outlines the design of the conjugate matched load. The real part R_t of the desired load impedance seen in Figure 5.4b is implemented using a simple resistor of 18.8 ohms. The negative capacitor of Figure 5.4b is implemented using an operational amplifier-based negative impedance converter, one example of which can be seen in Figure 5.9a. The input impedance of the circuit in Figure 5.9a can be derived using an assumed input-output transfer function of the operational amplifier:

$$V_{\text{out}} = A * (V_+ - V_-) \qquad (5.1)$$

where A is frequency-dependent open-loop gain, and V_{out}, V_+ and V_- are voltages at the amplifier's output, noninverting input and inverting input nodes, respectively. The input

impedance Z_{in} is derived by applying a test voltage v_{test} at the input node and observing the input current i_{test}, such that

$$Z_{in} = \frac{v_{test}}{i_{test}} \qquad (5.2)$$

Applying the properties of linear circuits and assuming infinite input and output impedance of the amplifier, it can be shown that the circuit's input impedance is equal to

$$Z_{in} = -Z_3 \frac{Z_1(A-1)+Z_2}{Z_2(A+1)+Z_1} \qquad (5.3)$$

Where Z_1, Z_2 and Z_3 are frequency dependent impedances as seen in Figure 5.9a. When the amplifier gain A is large, small terms can be neglected and this input impedance is approximately equal to
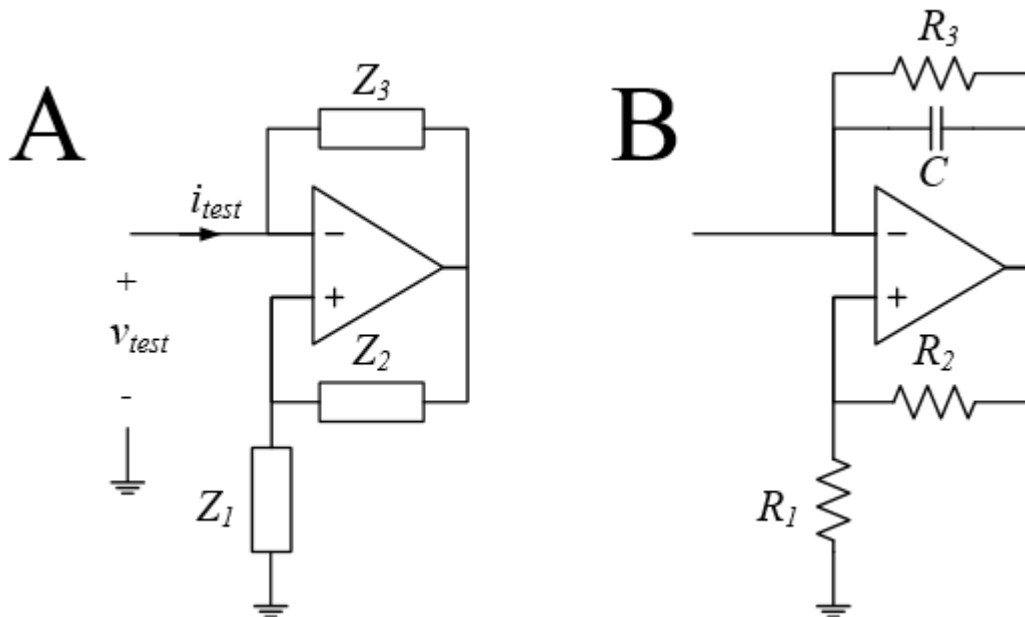
Figure 5.9. (a) generalized negative impedace converter. (b) Realized negative capacitance circuit.

$$Z_{\text{in}} \approx \frac{-Z_3 Z_1}{Z_2} \qquad (5.4)$$

The circuit in Figure 5.9b is the realization of the negative impedance converter used to provide a negative capacitance load to the acoustic energy harvester. Applying (5.4) to the circuit in Figure 5.9b, it has an input impedance approximately equal to

$$Z_{\text{in}} \approx \frac{-R_1 R_3}{R_2(1+j\omega C R_3)} = -\frac{R_3 R_1}{R_2(1+(\omega R_3 C)^2)} + \frac{j\omega R_3^2 C R_1}{R_2(1+(\omega R_3 C)^2)} \qquad (5.5)$$

with R_1, R_2, R_3 and C as in Figure 5.9b, and angular frequency ω in radians. Negative feedback resistor R_3 is for the purpose of low frequency stability as discussed in Section 5.4. The real part of (5.5) manifests as a negative resistor, supplying power from the operational amplifier to the harvester. Ideally R_3 is large such that at frequencies of interest (50Hz-1KHz) this negative resistor is negligibly small. However, the stability constraint discussed in Section 5.4 forced an implemented value of R_3 which causes (5.5) to have a significant real component below approximately 400Hz. Therefore, the load circuit in Figure 5.9b is approximately an ideal capacitor at frequencies above 400Hz, and in addition to the negative capacitance supplies energy to the harvester at frequencies below 400Hz. Therefore, above approximately 400Hz the circuit has an input impedance resembling a capacitor having capacitance C_{eff}, where

$$C_{\text{eff}} = \frac{C R_2}{R_1} \qquad (5.6)$$

An operational amplifier (Linear Technologies LT1677) was chosen with nominal open-loop gain of $19*10^6$, gain-bandwidth product of 7.2MHz, and MOSFET input stages with input resistance and capacitance of 2GΩ and 4.2pF, ensuring the above ideal operational amplifier assumptions are valid with little error.

The entire circuit, including the harvester's simplified model, is seen in Figure 5.10.

Circuit component values are given in Table 5.1. Feedback resistor R_2 is implemented as a series

combination of two resistors R_{2a} and R_{2b}, where R_{2b} is a potentiometer and is used for tuning of

the negative capacitance value. A detailed SPICE model of this design can be found in Appendix

C.
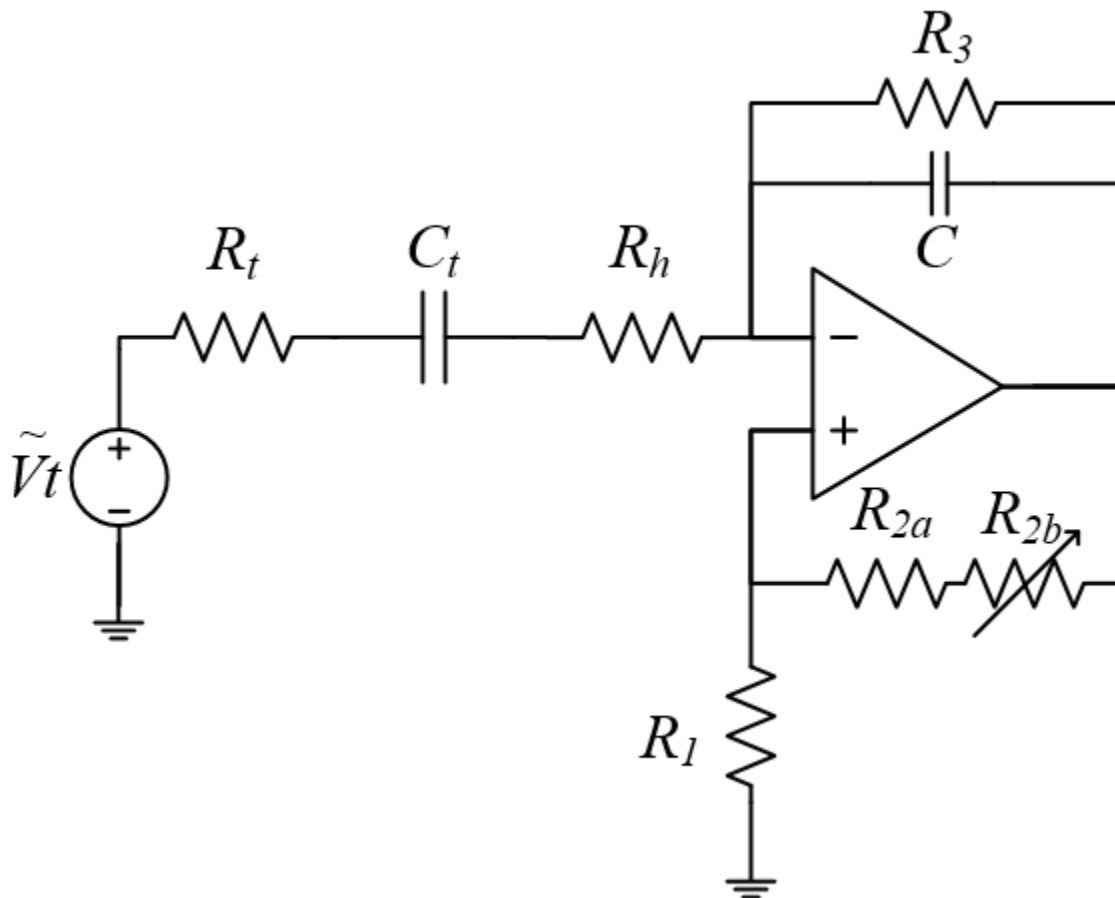
Figure 5.10. Entire circuit, including harvester simplified electromechanical model and conjugate matched load resistance and negative capacitance, as generated by a negative impedance converter circuit.

Component	Value	Unit
Vt	2.7	mV
Rt	18.8	Ω
Ct	16.47	nF
Rh	18.8	Ω
R1	49.9	K Ω
R2a	450	Ω
R2b	100 (max)	Ω
R3	2.55	MΩ
C	1.65	uF

Table 5.1. Circuit component values used in circuit realization of harvester load.

5.4 Stability Considerations

Due to the negative impedance characteristic of the circuit and it's frequency dependent positive and negative feedback, a number of potential instabilities are inherent to the system. Careful design of circuit schematic and layout are required to mitigate the effect of these potential instabilities. Stability analysis on the system in Figure 5.10 results in a constraint on the system net feedback β, such that [19]

$$Re(\beta) = Re(\beta_- - \beta_+) > 0 \qquad \forall F \qquad (5.7)$$

where β_- and β_+ are the negative and positive feedback factors, respectively. Four sources of potential instability exist, which are discussed in Sections 5.4.1-5.4.4. These sources of instability include leakage resistance, parasitic capacitance, resonance, and low-frequency poles associated with resistive negative feedback.

86

5.4.1 Leakage: Very Low Frequency Stability

When considering stability at very low frequencies, the circuit model in Figure 5.10 is modified to include Rp, a parasitic leakage resistance. Rp models the leakage resistance in the PVDF film, along with board leakage and input resistance of amplifiers used for instrumentation (see Section 6.3). Capacitors are removed from the very low frequency stability model, having large impedance at low frequencies. The resulting circuit is seen in Figure 5.11. Negative feedback factor β_- at low frequencies is given by the voltage division ratio

$$\beta_{-,\text{lf}} = \frac{R_p + R_h}{R_p + R_h + R_3} \qquad (5.8)$$

Positive feedback factor β_+ at low frequencies is given by the voltage division ratio
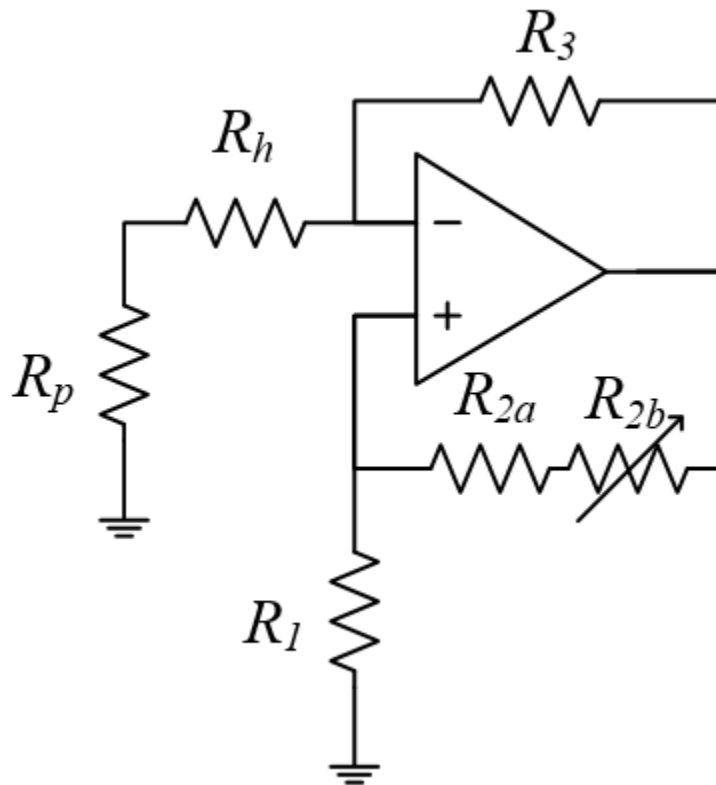
Figure 5.11. Circuit model for low frequency stability.

$$\beta_{+,\text{lf}} = \frac{R_1}{R_1 + R_{2a} + R_{2b}} \quad (5.9)$$

Combining (5.7) - (5.9), applying known values of R1, R2a, and R2b, from Table 5.1, and neglecting Rh results in $R_p > 100R_3$ as constraint relating R_p and R_3 for low frequency stability.

The high impedances involved preclude direct measurement of R_p; the maximum stable value of R_3 was found empirically to be 2.55MΩ. As will be discussed in Section 5.4.4, R_3 also affects AC stability, which imposes constraints driving R_3 to be as large as possible.

5.4.2 Parasitic Capacitance: Low Frequency Stability

At low frequencies (10Hz-900Hz), the resistors R_t and R_h in Figure 5.10 have negligible impedance when compared to that of capacitors C_t and C, and can therefore be neglected. Resistor R_3 similarly is large enough to be negligible when in parallel with capacitor C. C_t is nearly constant in this frequency range. In addition, parasitic capacitance C_p on the inverting node of the amplifier has an impact on stability. C_p models the parallel capacitance contributed by circuit board trace capacitance, amplifier input capacitance, as well as capacitance contributed by input capacitance of instrumentation amplifiers, as discussed in Section 6.3. The resulting stability model is seen in Figure 5.12.

The circuit in Figure 5.12 can be seen as a resistive voltage divider R_1, R_{2a}, R_{2b} providing positive feedback and capacitive voltage divider C, C_t, C_p providing negative feedback. Applying (5.7) to the circuit in Figure 5.12 and applying known values of C_t R_1, R_{2a} and R_{2b} imposes the following constraint on C and C_p:

$$C > 100(C_t + C_p) \quad (5.10)$$
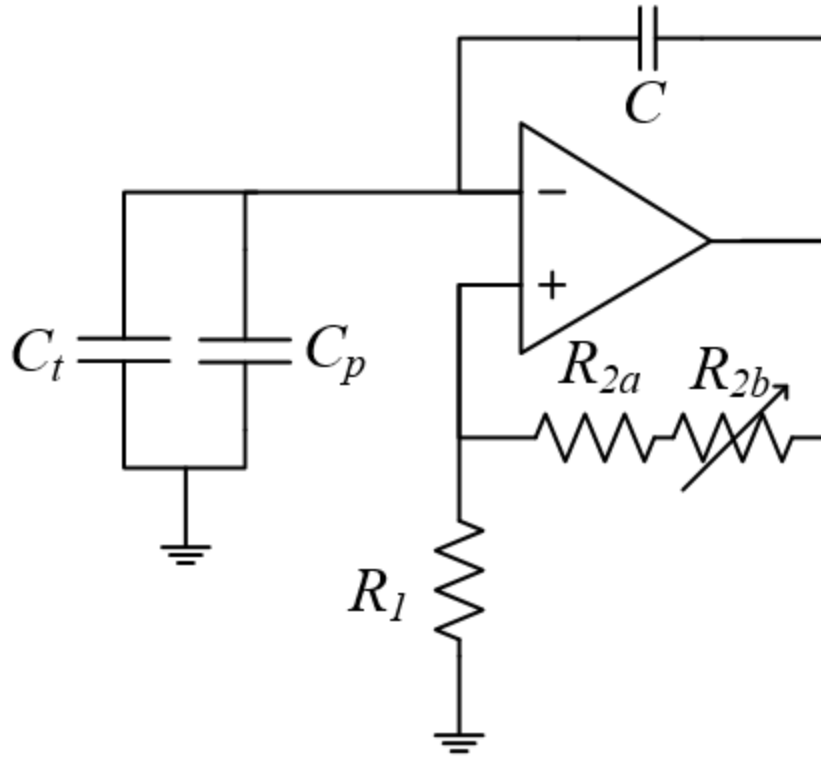
Figure 5.12. AC stability model for 10Hz-900Hz frequency range.

In ideal conditions $C_p = 0$, allowing C to be set to $100C_t$, producing a perfect cancellation and therefore broadband impedance match. However, the presence of parasitic capacitance C_p effectively reduces the amount of negative feedback, shifting the instability point to a value of negative capacitance C which is an over cancellation. Therefore, it is crucial to minimize parasitic capacitance on the inverting node. The value of C_p was determined analytically to be the parallel capacitance of four sources: negative capacitance operational amplifier (4.2pF), voltage measurement operational amplifier (4.2pF), current measurement instrumentation amplifier (3.2pF) and PCB trace capacitance (1pF), or a total capacitance of 12.6pF. Therefore, the negative capacitance load cannot stably approach perfect cancellation of harvester capacitance C_t within 12.6pF. Particular care was taken in circuit board layout to minimize the effect of PCB capacitance; circuit board layout details can be seen in Appendix D. As seen in

Figure 5.8, the effect of this 12.6pF offset is the reduction of maximum stable performance to approximately harvesting 20% of the available energy, with losses primarily occurring at low frequencies.

5.4.3 1KHz AC Stability: Resonance

An additional source of instability arises from the effect of resonance. This occurs near 1KHz for both the transmission line and the mass-spring system. Reduced reactance at frequencies surrounding resonance has the effect of locally increasing the Thévenin equivalent capacitance C_t, as seen in Figure 5.2.

Applying (5.7) and (5.10), a potential for instability exists near 1KHz in the implemented circuit due to the implemented circuit's frequency independent negative capacitance and the local increase in Ct. Due to the frequency invariant nature of the implemented negative impedance converter circuit, it is impossible to achieve perfect cancellation of reactance at low frequencies without suffering instability near 1KHz. Therefore, the best possible performance achievable is a capacitance cancellation mismatch equal to the height of the peak in Figure 5.2, or approximately 80pF. As seen in Figure 5.8, this has severe consequences for harvested power at low frequencies. The 80pF offset reduces maximum stable harvesting performance to approximately 1% of available power, with losses primarily occurring at low frequencies. Circuit modifications would be necessary to overcome this limitation.

5.4.4 Low Frequency Stability: Negative Feedback Resistor

A fourth source of potential instability arises from negative feedback resistor R_3, as seen in Figure 5.10. Applying linear circuit techniques and ideal operational amplifier assumptions,

the transfer function from input voltage V_t to operational amplifier output voltage V_o can be found as

$$\frac{V_o}{V_{in}} = \frac{AR_3}{(sCR_3+1)\left(\frac{A(sC_tR_h+sC_tR_t+1)}{sC_t\left(R_h+R_t+\frac{1}{sC_t}+\frac{R_3}{sCR_3+1}\right)} - \frac{AR_1}{R_1+R_2}+1\right)\left(R_h+R_t+\frac{1}{sC_t}+\frac{R_3}{sCR_3+1}\right)} \qquad (5.11)$$

with variables taken as before in Chapter 5. This model ignores the effects of leakage, parasitic capacitance, and ignores resonance effects by modeling the harvester as a series R_t and C_t. By algebraic manipulation, (5.11) can be broken down into five poles, one of which is purely real, having location

$$p_1 = -\frac{1}{CR_3} \qquad (5.12)$$

The remaining four poles come as two sets of pairs. One pair is real-valued and stable given the component values used in Table 5.1 and has pole location

$$p_2, p_3 = \frac{-C_t(R_t+R_h)-R_3(C+C_t)\pm\sqrt{((-C_t(R_h+R_t)-R_3(C+C_t))^2-4C\,C_t\,R_3\,(R_h+R_t))}}{2CC_tR_3(R_t+R_h)} \qquad (5.13)$$

where component values are taken as before.

The second pair of poles are given in terms of the three variables Pa, Pb and Pc;

$$p_a = CR_3(R_h+R_t)\left(\frac{R_1}{R_1+R_2} - \frac{1}{A} - 1\right) \qquad (5.14)$$

$$p_b = R_3\left(\frac{R_1}{R_1+R_2} - \frac{1}{A}\right) + \left(\frac{R_1}{R_1+R_2} - \frac{1}{A} - 1\right)\left(R_h + R_t + \frac{CR_3}{C_t}\right) \qquad (5.15)$$

$$p_c = \frac{\frac{R_1}{R_1+R_2} - \frac{1}{A} - 1}{C_t} \qquad (5.16)$$

The second pair of poles are then located at

$$p_4, p_5 = -\frac{p_b}{2p_a} \pm \frac{\sqrt{p_b^2 - 4p_a p_c}}{2p_a} \qquad (5.17)$$

with component values as before. Given the component values in Table 5.1 and a perfect impedance match, these poles appear as conjugate pairs. While not unstable in the formal bounded input/bounded output sense, the poles do produce lightly damped oscillation at low frequencies surrounding 100Hz, adding risk of saturating the negative impedance converter operational amplifier. The poles also provide a 180 degree phase shift at low frequencies, setting the minimum frequency at which negative capacitance is achieved and therefore energy harvested.

It is desirable to minimize these poles' frequency as much as possible, to maximize harvesting bandwidth. It is also desirable to maximize damping of these poles, mitigating the risk of saturating the operational amplifier. These design goals drive the decision to maximize R_3 as much as possible, to the extent allowed by low frequency stability constraints described in Section 5.4.1. These design goals also drive the decision to maximize capacitance division ratio seen in (5.6), maximizing capacitor C. This has the added benefit of mitigating the effect of parasitic capacitances described in Section 5.4.2. A pole-zero map and Bode plot of the transfer function described in (5.11), using component values in Table 1 are seen in Figures 5.14 and 5.15, respectively. The plots in Figures 5.13 and 5.14 assume a perfect impedance match, ideal operational amplifier, and omit instability sources described in Sections 5.4.1-5.4.3. The

conjugate poles at 100Hz add the requisite phase shift above 100Hz, precluding effective energy

harvesting below 100Hz. With a significant amount of energy in aircraft noise existing below

100Hz it is desirable to reduce the frequency of these poles by increasing R_3. However, the

choice of R_3 and therefore pole location was constrained by leakage effects described in Section

5.4.1. The light damping at 100Hz on both the Bode plot and the pole-zero diagram indicates the

risk of saturating the operational amplifier for even small acoustic inputs at 100Hz, given a

perfect impedance match. As will be seen in Chapter 7, the best stable load realized

experimentally had an impedance mismatch equal to 130pF. This mismatch stabilizes these

poles, significantly damping them. The resulting pole-zero and Bode plots can be seen in Figures

5.15 and 5.16, respectively. Corresponding MATLAB code for stability analysis in both

symbolic and numerical form can be found in Appendix E.
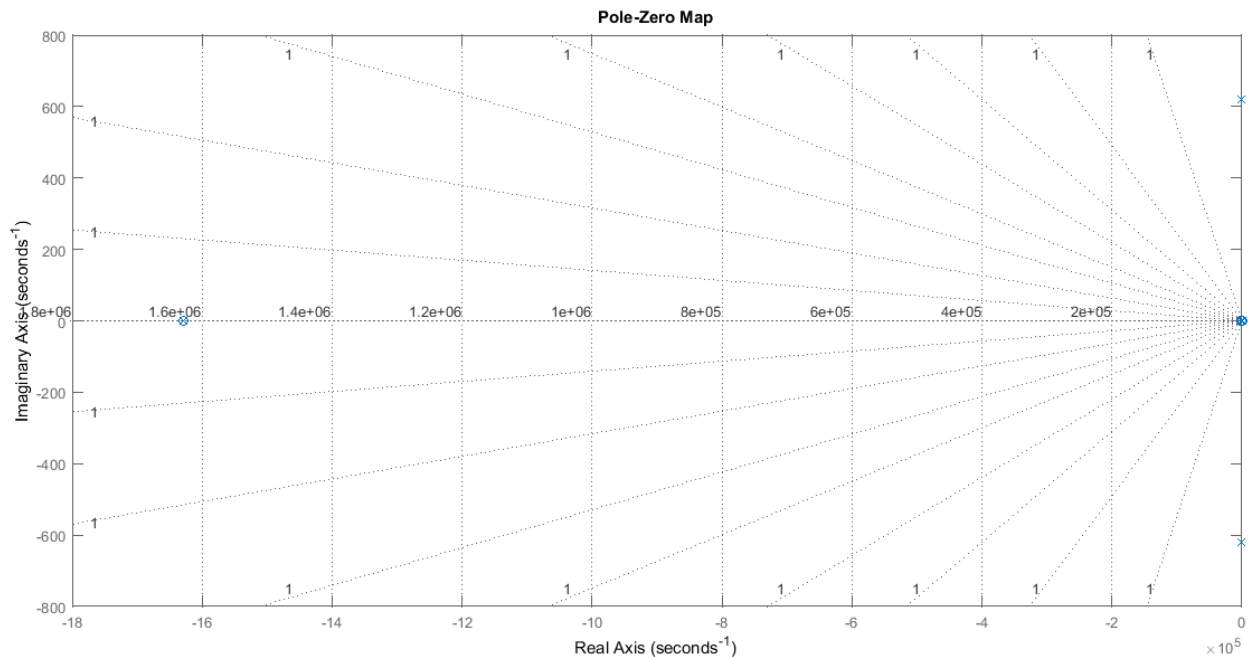
Figure 5.13. Pole-zero map of operational amplifier's Vo/Vin transfer function given perfect
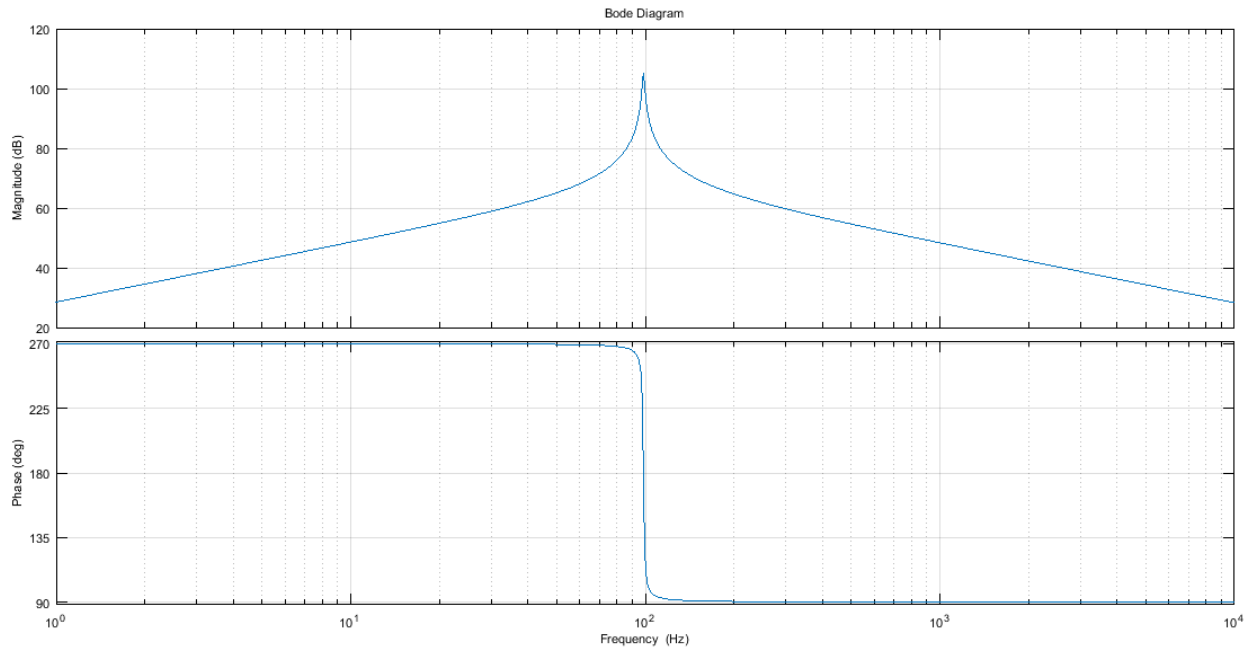
impedance match.

Figure 5.14. Bode plot of operational amplifier's Vo/Vin transfer function given perfect
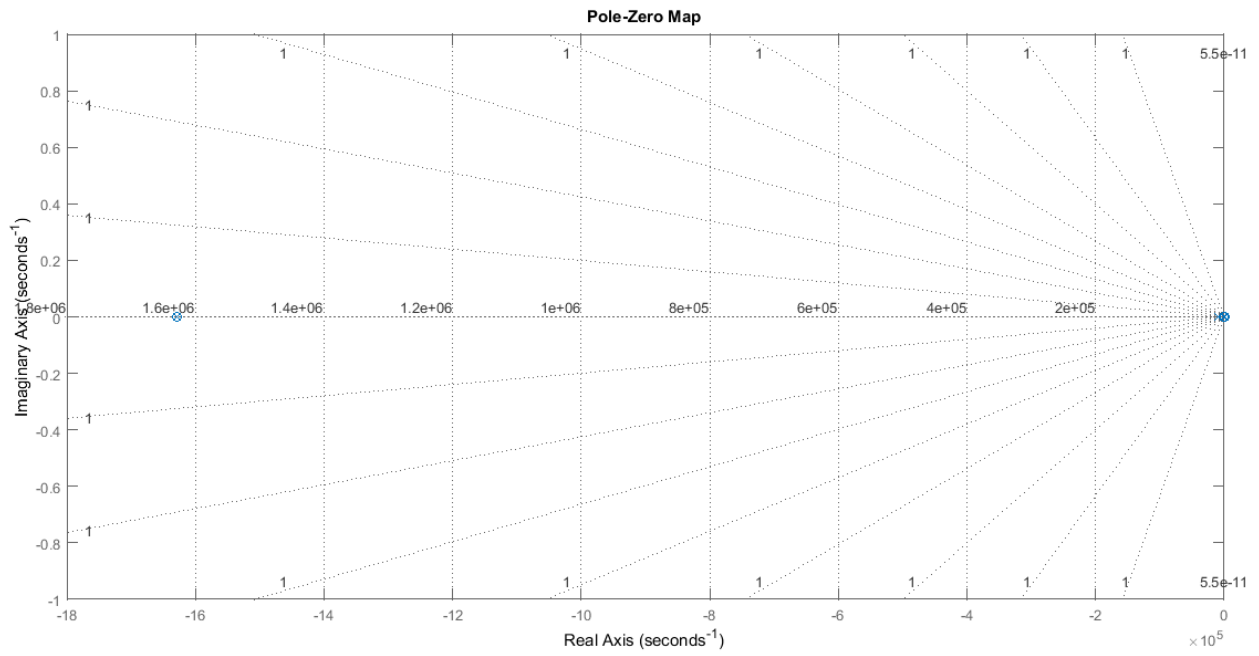
impedance match.

Figure 5.15. Pole-zero map of operational amplifier's Vo/Vin transfer function given realized impedance match.
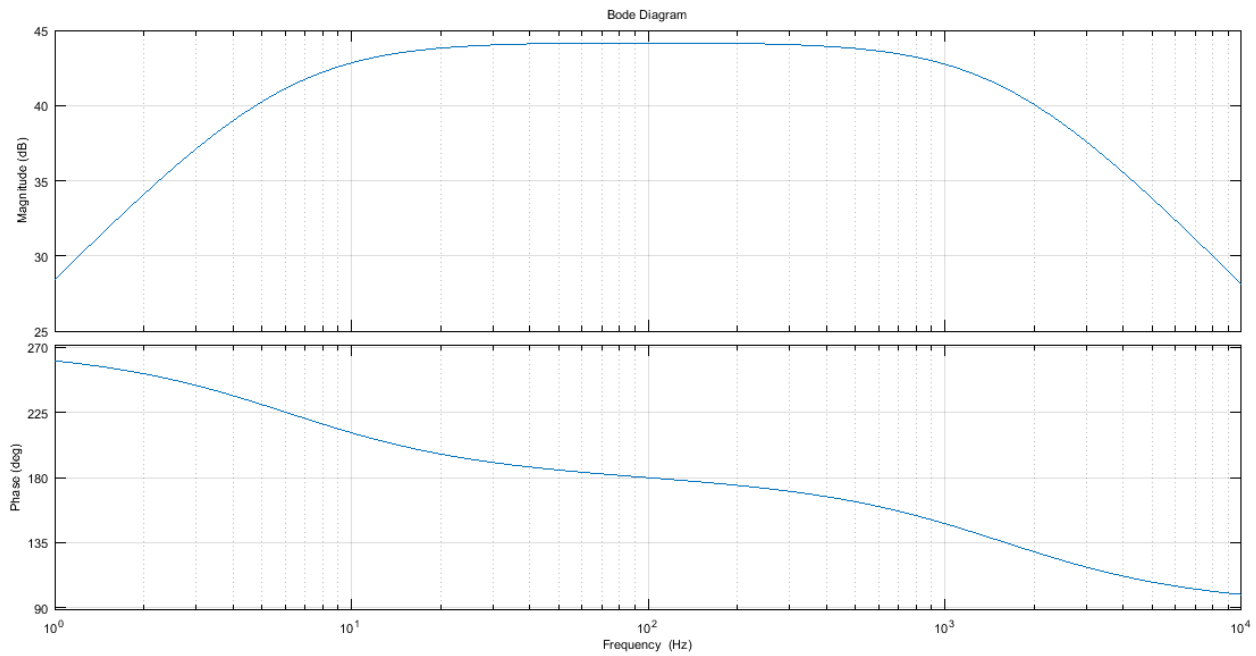
Figure 5.16. Bode plot of operational amplifier's Vo/Vin transfer function given realized impedance match.

5.5 Chapter Summary

A simplified electromechanical harvester model is presented, allowing for broadband impedance match using relatively simple electronics. The harvester's ability to efficiently harvest broadband noise is relatively tolerant to environmental factors, such as air temperature and pressure. It is extremely sensitive to negative load capacitance, requiring approximately a 20pF precision to result in efficient harvesting while remaining stable. This presents a significant challenge for efficient broadband harvesting. A design is presented for an operational amplifier based negative impedance converter, which is used for providing a conjugate matched load to the

96

harvester for optimal energy transfer. A number of stability challenges are identified and addressed, including parasitic resistances and capacitances, resonance effects and lightly damped oscillatory poles. These challenges, while not fundamental to broadband acoustic energy harvesting, ultimately limit harvester performance in the implemented design.

Chapter 6

Energy Harvester Test Bench

An extensive testbench infrastructure is designed and assembled. The primary purpose of the testbench is to drive the system acoustically and measure the response of various electrical outputs, in a predictable and repeatable way. Industry best practices are used throughout the process to ensure precision.

6.1 Anechoic Chamber

At the core of the testbench is an acoustic anechoic chamber, seen in Figure 6.1. An acoustic anechoic chamber has two main properties, which are essential for acoustic characterization. Firstly, noise isolation significantly reduces or eliminates the effect of intruding noise from the local environment, both acoustic and mechanical vibrations. This is achieved by a combination of concrete walls, acoustic foam cladding, airtight walls and door, and tensioned wire flooring. The test chamber used in this work has a noise floor of less than 48 dB(C), where dB(C) are decibels of sound pressure, referenced to 20uPa with a standard C-weighting filter applied. C-weighting is used due to the emphasis on low frequencies, which are of interest in this work. Secondly, predictable sound field distributions are enabled by a test chamber design which mitigates the effect of room resonances and echoes. This is achieved by the use of sound

absorbing foam on walls, ceiling and floor. This has the effect of reducing the quality factor of

the room's resonances to near zero so that no sound is reflected, approximating free-field

conditions. The test chamber used in this work is effective in this sense down to a cutoff

frequency of approximately 300Hz. Test equipment and other objects in the room during testing

are covered in acoustic foam to mitigate effects associated with their reflective properties.

Objects not covered in acoustic foam, such as test computers or operators were either removed

from the chamber during testing or obscured behind acoustic foam.
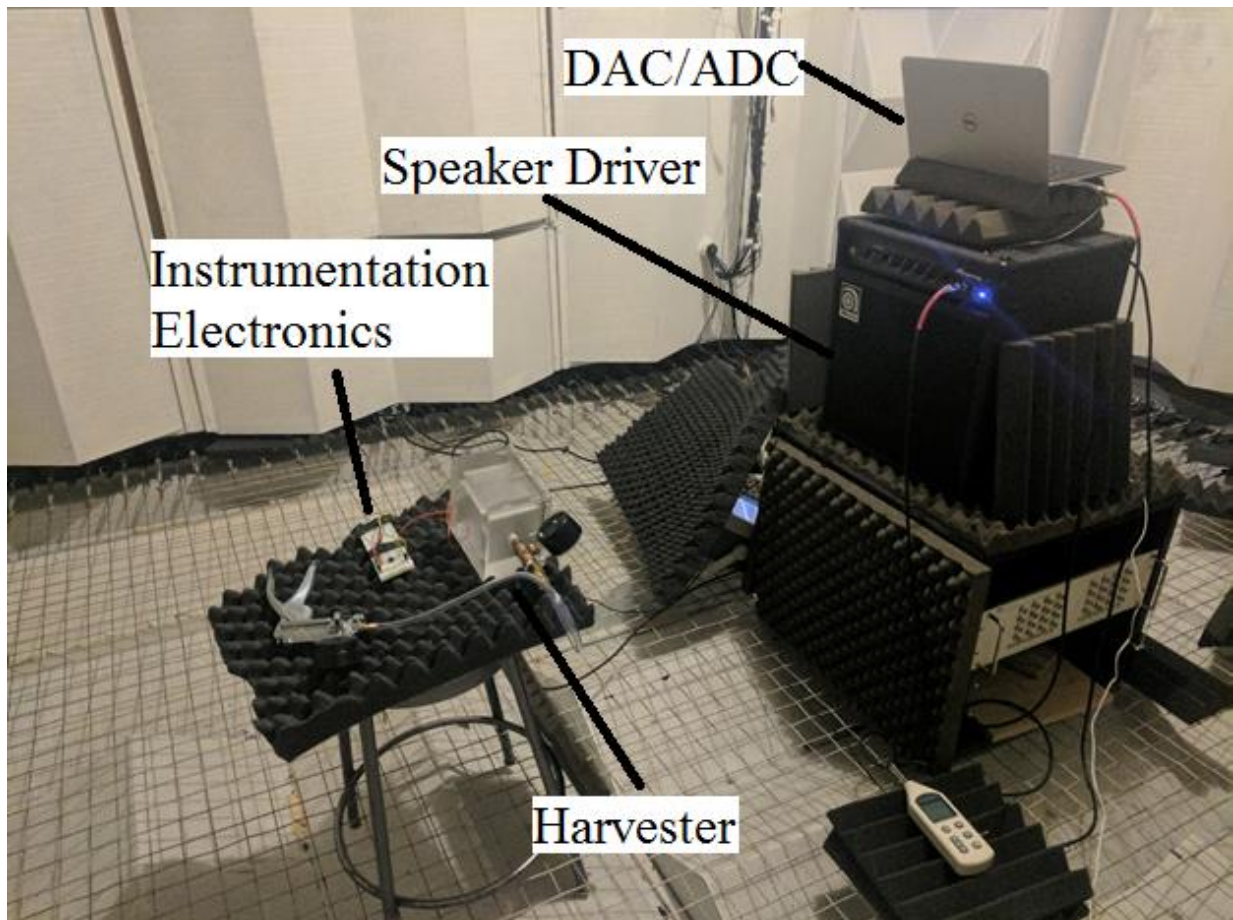
Figure 6.1. Anechoic chamber used in Acoustic Energy Harvester characterization.

6.2 Testbench Architecture and Calibration

The entire signal path representing the testbench is seen in Figure 6.2. The harvester is driven acoustically by a ten-inch speaker driver (Ampeg BA-110), rated at 40 Watts. The harvester is driven at a distance of one meter. Electrical signals output from the harvester's instrumentation are sampled and recorded by a 24-bit, 96KHz audio ADC (AKAI EIE Pro) and recorded via a laptop PC.

The purpose of the calibration procedure is to counteract the frequency response effects of the testbench to provide a flat, frequency-invariant pressure field to the harvester. The calibration procedure is performed in steps, intended to characterize and offset the frequency response of each component individually.

The frequency response of the operating system software audio pipeline, drivers, ADC and DAC is characterized via a loopback test, as seen in Figure 6.3. The output DAC is electrically connected directly to the ADC, driving it directly. During this phase of the test the
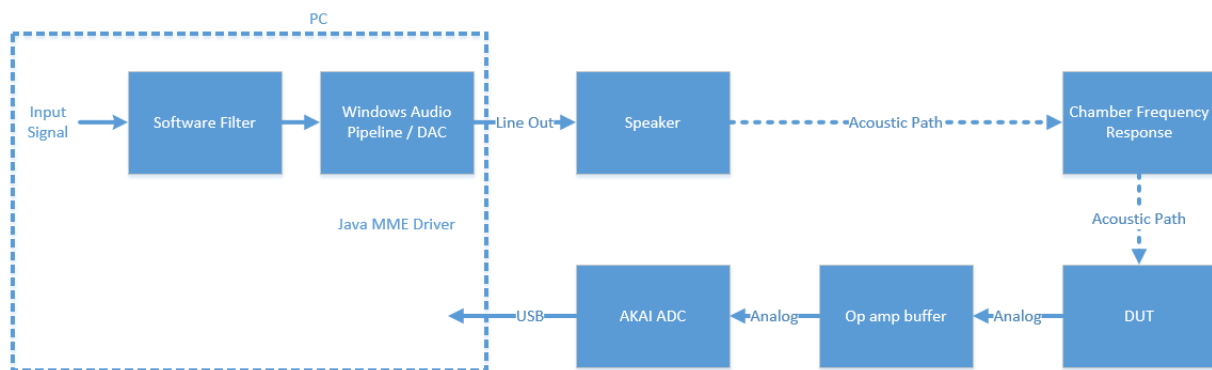
Figure 6.2. Entire signal path used in Acoustic Energy Harvester characterization.
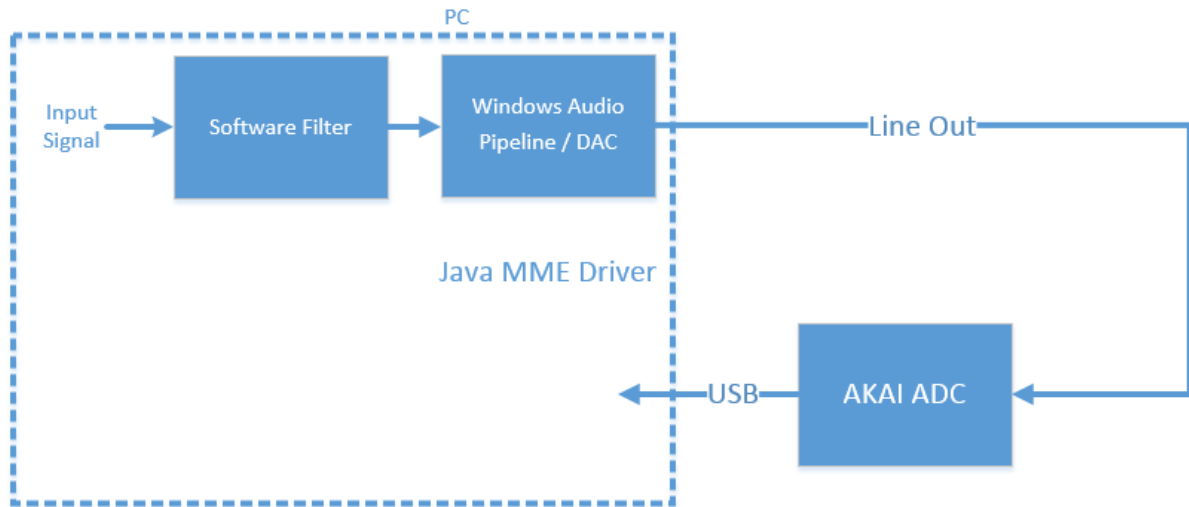
Figure 6.3. Loopback test used for characterizing operating system audio pipeline, drivers, DAC and ADC.

 "software filter" block has a flat, unity-gain response. The frequency response of the remaining components is measured using software tools (Room EQ Wizard) using a frequency-sweep "chirp" input. This frequency response is negated using an inverse filter, flattening the frequency response of these components.

The second stage of the calibration is intended to calibrate out the frequency-response contributions of the speaker amplifier, speaker driver, and test chamber, as seen in Figure 6.4. A flat SPL meter (Foneso GM1356) is used as a reference microphone for acoustic measurements.

The reference microphone is collocated with the harvester, resulting in the same chamber frequency response. A chirp is driven acoustically and the frequency response measured. Given that all other components have a frequency response which has been measured and compensated (software pipeline, drivers, ADC, DAC) or known to be flat (reference microphone), the resulting measurement describes the composite frequency response of the speaker amplifier,
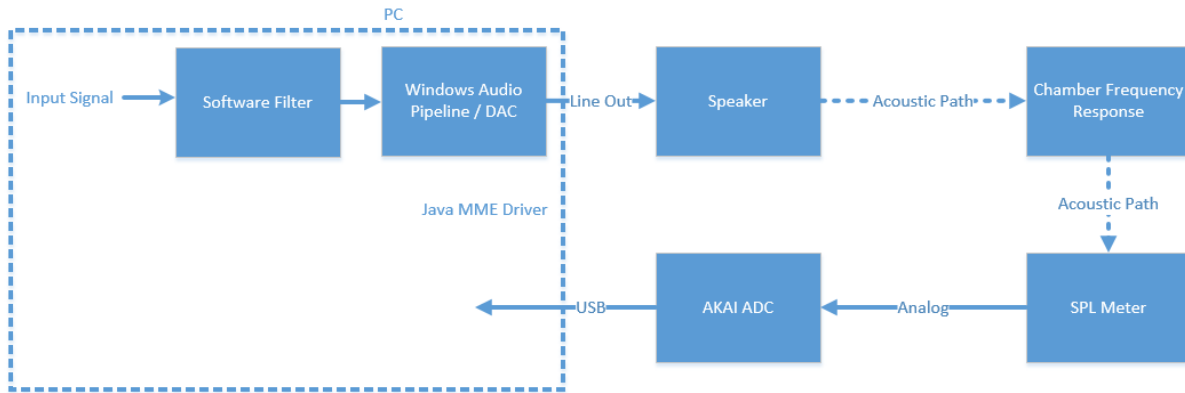
Figure 6.4. Acoustic calibration used to calibrate the effects of speaker amplifier, speaker driver, and test chamber.

speaker driver, and test chamber. A 20th order inverse peaking filter is generated in software (Room EQ Wizard) and applied digitally (EqualizerAPO) to the output signal to flatten the effects of the aforementioned components. The end result is a pressure field presented to the harvester which is flat in frequency. In practice the composite frequency response was flattened within +/-3 dB SPL over a frequency range of 70-7000Hz. An example of such a calibration is
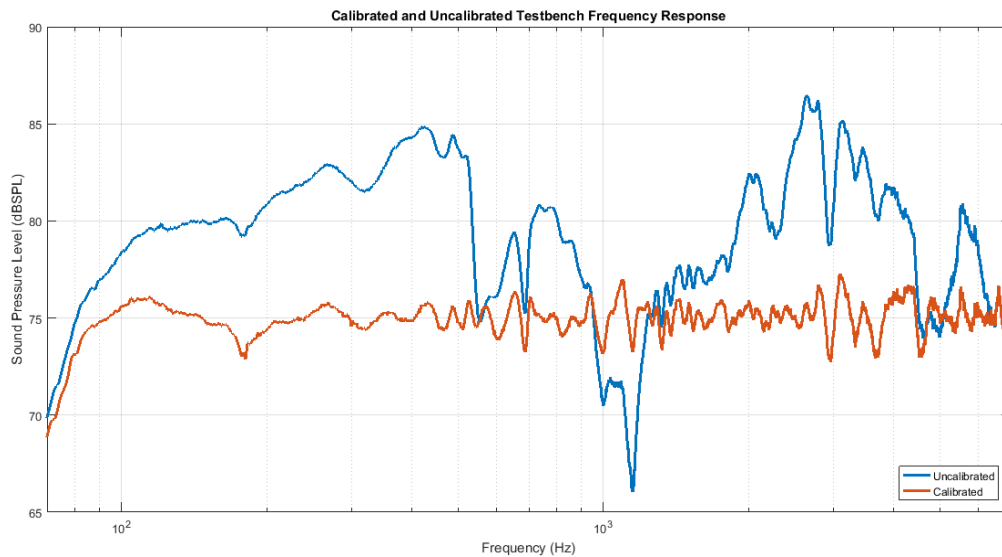
Figure 6.5. Frequency response of the measurement testbench before and after calibration.

102

seen in Figure 6.5. The sample characterization can then proceed replacing the reference

microphone with the sample and electrical instrumentation.

6.3 Energy Harvester Electrical Instrumentation

The harvester is instrumented with electrical circuitry to measure the harvester's loaded

voltage and current. The harvester's voltage is measured via an operational amplifier (Linear

Technologies LT1677) configured as a unity-gain buffer, which drives the ADC seen in Figure

6.2. See Appendix C (SPICE harvester model) for complete details of circuitry. The amplifier's

FET inputs result in extremely high input resistance (2GΩ nominal) and low input capacitance

(4.2pF nominal), minimizing effects on harvester performance.

Harvester output current is measured via an instrumentation amplifier (Linear

Technologies LT1167), using the load resistor (18.8Ω) as a current-sense resistor. The

amplifier's FET inputs also yield high input resistance (1TΩ nominal) and low input capacitance

(3.2pF nominal), again minimizing effect on harvester performance. The effects of parasitic

capacitances and resistances are discussed in Section 5.4. The instrumentation amplifier is

configured to have a nominal gain of 107. The instrumentation amplifier was chosen for a high

CMRR of 125 dB. The harvester output has a large common-mode signal ~10Vp and small

differential voltage across the load resistor. A CMRR of 125 dB across the load resistor of Rt

(18.8Ω) allows for measurement of currents as low as 5uAp with a maximum of 10% error. The

instrumentation amplifier directly drives the ADC seen in Figure 6.2.

6.4 Automated Data collection

The harvester is measured for it's voltage or current response when driven by a flat frequency sweep "chirp" signal, as produced by test software (Room EQ Wizard). An example output is seen in Figure 6.6. Voltage signal representing harvester's loaded voltage or current is recorded in units of dB SPL, referenced to an arbitrary 0 dB determined by the ADC's internal gain structure and software calibration gain. Simultaneously, a data point of Vpp at a known frequency is recorded manually via oscilloscope observation. This data sample is used in post-processing to normalize the output signal in dB SPL back to units of Volts peak-peak for the entire frequency spectrum.

The automated data collection system also measures phase of the output signal, referenced to the phase of the outgoing digital signal which drives the speaker driver. The absolute phase is unimportant; it is affected by software calibration filters and acoustic paths with unknown phase. However, the phase measurement of importance is the relative phase of voltage and current output by the harvester, which is used in power calculations seen in Section 7.2. Therefore, the unknown phase shift contributed by filters and acoustic paths is of trivial importance given that it is constant between measurements.
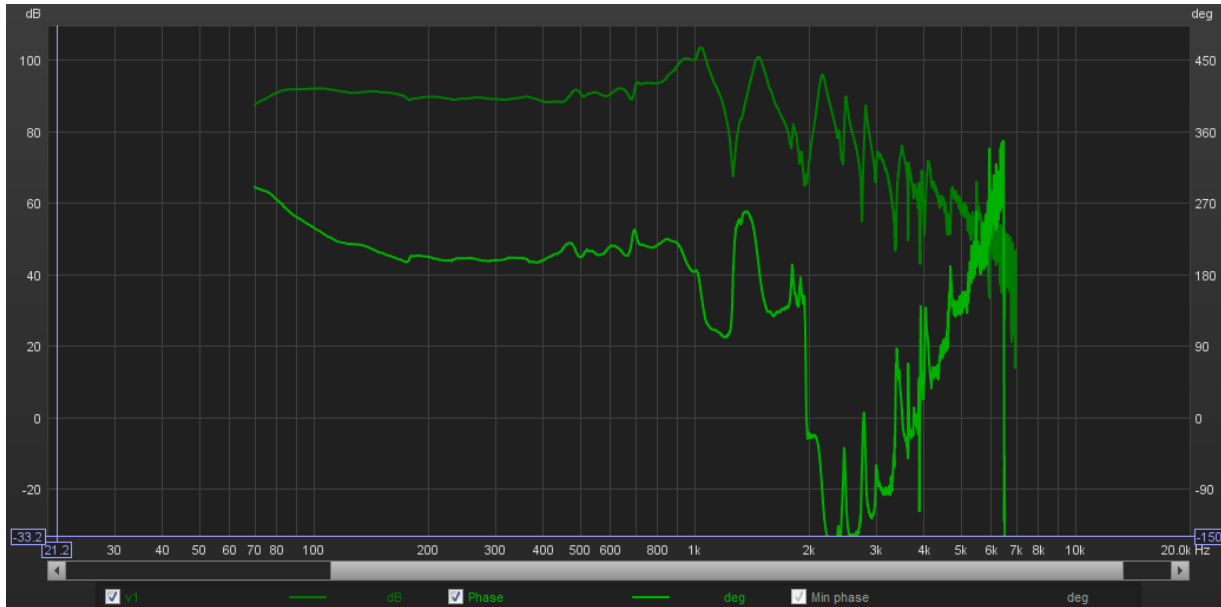
Figure 6.6. Output measurement of magnitude and phase output from an acoustic energy harvester sample.

6.5 Chapter Summary

In summary, a testbench system is presented. The use of anechoic chamber facilities allows for approximately free-field measurements free of echoes and resonances, and an extremely low noise floor. A test system architecture and calibration procedure are developed using a calibrated reference microphone, resulting in high fidelity and repeatable measurements. The harvester sample is characterized using instrumentation circuitry with special focus on high input impedance and low noise, which is crucial given the low currents and high impedances involved. Finally, an automated test suite is assembled and procedure developed, allowing for rapid characterization of samples. The test system is capable of measuring the voltage and current at the harvester's nodes as a function of frequency, given arbitrary loading. It is capable of accurately producing frequencies between 70Hz and 7KHz with programmable intensity.

105

Chapter 7

Harvesting Simulations and Experiments

This chapter presents four experiments. The first two experiments serve to validate the analytical model developed in Chapter 3. The last two experiments explore broadband harvesting. The first experiment (Section 7.1) compares the measured open-circuit voltage of the harvester to the modeled source voltage Vt. Attempts were made to directly measure the harvester's source impedance Rt and Xt using impedance analysis equipment, however this was unsuccessful due to the harvester high reactive impedance, small real impedance and the low frequencies involved. Therefore, the harvester load impedance was validated via the second experiment (Section 7.2.1), which compares the harvested power to modeled power delivered to a purely resistive load. The third experiment (Section 7.2.2) demonstrates the broadband performance benefit attained with the conjugate load designed in Chapter 5. This experiment compares the harvested power measured to the maximum possible power, and the modeled harvested power. The fourth experiment (Section 7.3) uses the same conjugate matched load, and compares measured loaded voltage to the modeled loaded voltage.

All measurements were taken using the anechoic chamber testbench described in Chapter 6, calibrated to be flat in frequency. The harvester was driven with a frequency-swept chirp signal of 512,000 points, from 70Hz – 7KHz, at a constant 75 dB SPL.

7.1 Open-Circuit Voltage

A comparison of modeled and measured open-circuit harvester voltage is seen in Figure 7.1. The model accurately describes harvester behavior in a general sense. It captures trends in open-circuit voltage both in terms of low-frequency behavior, as well as resonances and antiresonances arising from the transmission line behavior and mass-spring resonance. Extra peaks and nulls in the experimental data are explained by higher order modes in the film dynamics, where the model only considers the fundamental mode (see Section 3.11). The divergence of the model and experimental data can be attributed to experimental uncertainty, represented in Figure 7.1 as centered error bounds. The divergence can also be explained by uncertainty surrounding film parameters. Open-circuit voltage is inversely proportional to the film's d_{31} parameter, which is specified by the manufacturer without specified uncertainty. Open-
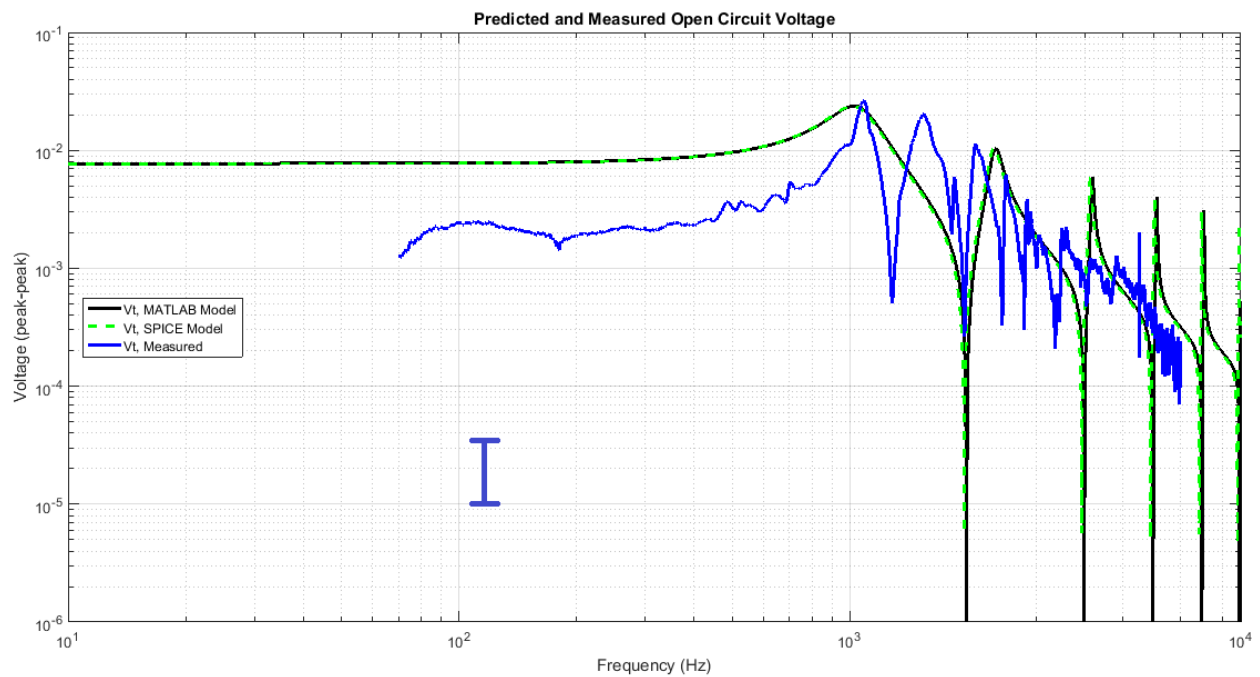
Figure 7.1. Modeled versus measured open circuit voltage, with experimental error bounds.

circuit voltage is also inversely proportional to the film's Young's modulus, which is specified by the manufacturer in a range of 2-4GPa, an uncertainty of 66% surrounding the nominal value. Finally, open-circuit voltage is negatively proportional to film bias pressure, which carries an uncertainty of approximately 10%. These uncertainties, combine with experimental uncertainty to place the measured open circuit voltage within the bounds of uncertainty.

7.2 Harvested Energy

7.2.1 Harvested Energy Spectrum, Resistive Loading

An expression for power delivered from the harvester to the load is given by [27]

$$P_{\text{load}} = \frac{1}{2} |V_{\text{load}}||I_{\text{load}}| \cos(\theta_{\text{Vload}} - \theta_{\text{Iload}}) \qquad (7.1)$$

where V_{load} and I_{load} are the voltage and current seen at the output of the harvester, respectively, and θ_{vload} and θ_{iload} are the phase of the harvester's voltage and current, respectively, in degrees, and P_{load} is the delivered power in Watts.

In the case of a purely resistive load, voltage and current are in phase and combined with Ohm's law, (7.1) reduces to

$$P_{\text{load}} = \frac{1}{2} |I_{\text{load}}|^2 R_{\text{load}} \qquad (7.2)$$

where R_{load} is the load resistance, in ohms. A frequency spectrum of modeled versus measured power is seen in Figure 7.2, for purely resistive loads of 1kΩ, 10kΩ, 100kΩ, and 1MΩ. Model predictions are provided for both MATLAB analytical and SPICE circuit models. Because purely resistive loads do not match the harvester impedance in a broadband sense, efficient

broadband harvesting is not expected in this case. The model is confirmed by the experimental

data, with the primary source of deviation stemming from unmodeled higher film modes, as

discussed in Section 3.11. The low-frequency rolloff of measured harvester power is explained

by the speaker driver's amplitude reducing in this region, as seen in Figure 6.5.
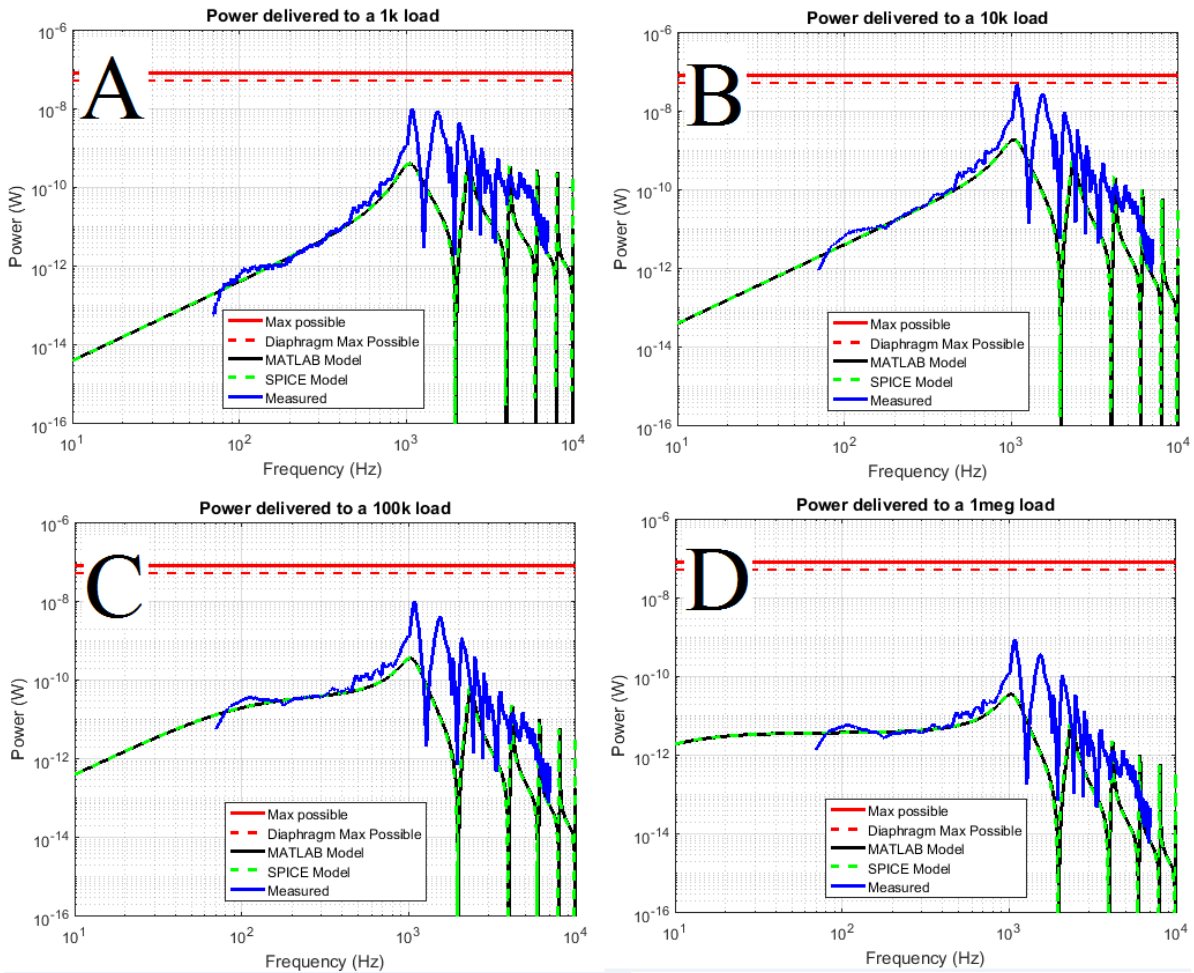
Figure 7.2. Modeled versus measured power output for purely resistive loads of (A) 1kΩ, (B)

10kΩ, (C) 100kΩ, (D) 1MΩ.

7.2.2 Harvested Energy Spectrum, Conjugate Matched Load

In the harvester load circuit implemented in Figure 5.10, the operational amplifier negative impedance circuit closely resembles an ideal negative capacitor above approximately 400Hz, with negligible contribution to the real part of the load impedance. Therefore in this frequency range (7.2) applies as a measure of real power delivered to the load. Below 400Hz the negative real impedance arising from the negative impedance converter begins to have measurable impact, artificially inflating power measurements calculated by (7.2).

A comparison between harvested power as predicted by the MATLAB and SPICE models and measured power is seen in Figure 7.3. The best achievable design given the stability constraints (Section 5.4) is a conjugate matched load consisting of a perfectly matched real load of 18.8 ohms, and a series negative capacitive load of 16.6nF, approximately 130pF away from the source Ct of 16.47nF. This lack of perfect stable cancellation is consistent with stability analysis predictions derived in Section 5.4. Given this lack of perfect cancellation, it would be possible to adjust the real load resistor R_h (Figure 5.10) to improve harvesting performance at frequencies near resonance. However, this would have minimal benefit at low frequencies. This adjustment was not made in the reported performance.

The difference between MATLAB and SPICE models are explained by the SPICE model's inclusion of imperfect operational amplifiers with limited gain and bandwidth, parasitics related to circuit implementation and instrumentation amplifiers, and the nonidealities associated with the negative capacitance circuit as discussed in Section 5.4. As before, the additional peaks and nulls seen in the measured power are explained by higher order film modes, which are omitted from both models. Applying the modeled system with performance matching the best

110

experimental system to the input noise from a 747 aircraft takeoff yields a modeled harvester

power of 1.2uJ per takeoff event. This is approximately 0.25% of the maximum available power

of 491uJ, with losses primarily arising from imperfect impedance match at low frequencies. The

aircraft power numbers derive from a model which neglects imperfections associated with the

negative capacitance implementation, including parasitic negative resistance and imperfect

amplifier performance.

The demonstrated performance, while not optimally broadband, exceeds performance

possible in purely resistive loads. It also exceeds broadband harvesting performance achieved by

existing acoustic energy harvester designs, as described in Chapter 2. Figure 7.4 shows a

comparison between broadband harvesting performance measured experimentally for this work's

best conjugate matched load, this work's best purely resistive load, and performance reported in

[5], which is representative of the resonant designs used in typical implementations. The
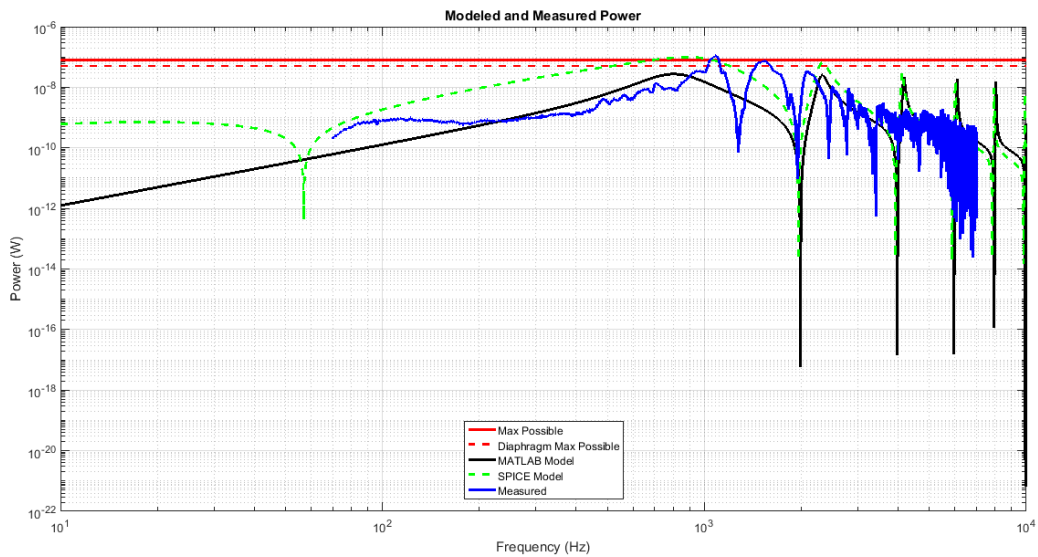
Figure 7.3. Modeled and measured power for the best stable design with conjugate matched
load.
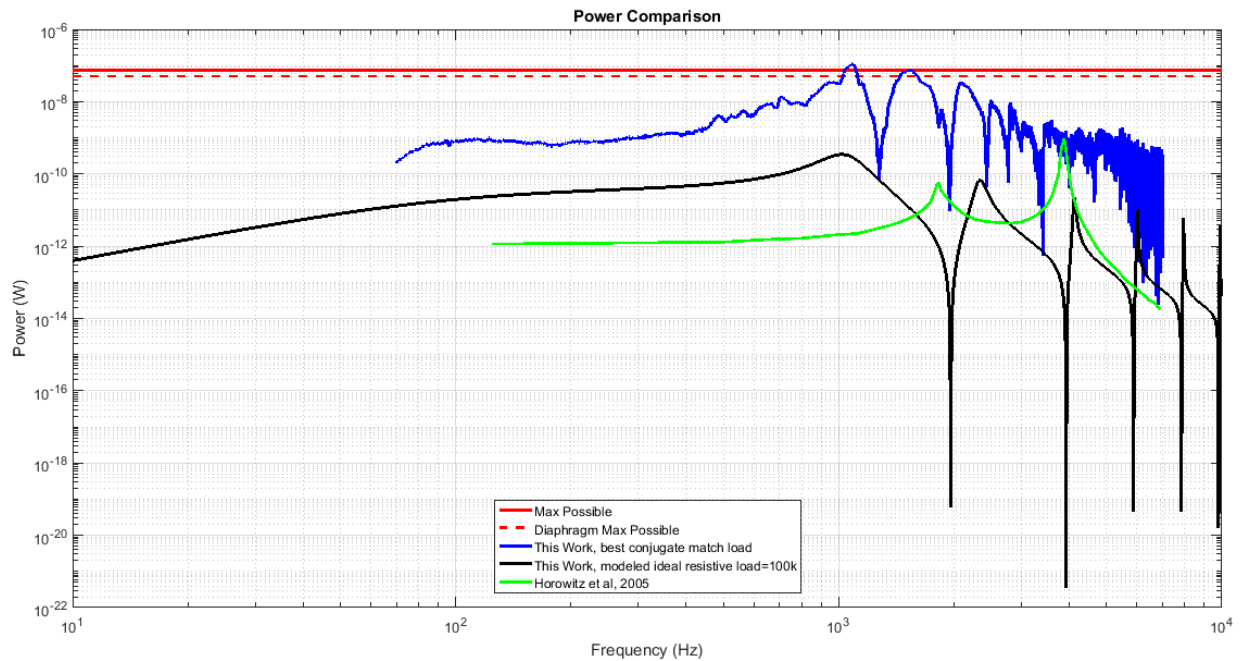
Figure 7.4. Comparison of broadband energy harvesting performance from this work's best conjugate matched load, this work's best resistive load (modeled), and representative performance yielded by resonant designs reported in literature [5].

performance reported from [5] is scaled to match input sound levels used in this work. The performance reported from [5] is also scaled up by a factor of 588 to be an equivalent harvesting area as this work, irrespective of practical limitations associated with such scaling.

7.3 Loaded Voltage

Modeled predictions of loaded voltage are derived by considering the system as a voltage divider. Applying this to the harvester source model in Figure 2.8 and a general load impedance Z_{load}, the loaded voltage is found to be

$$V_{\text{loaded}} = \left| \frac{V_t Z_{\text{load}}}{Z_{\text{load}} + R_s + jX_s} \right| \qquad (7.3)$$

where Rs and Xs are taken as in Chapter 2 and Vt is Thévenin source voltage. Such a loaded

voltage applies for both perfect conjugate loads and non optimal loads, as seen in Figure 7.4

("MATLAB model").

Applying this to a generalized Thévenin source as seen in Figure 2.8 and a perfect idealized

conjugate load as seen in Figure 2.9b, (7.3) simplifies to

$$V_{\text{loaded,conjugate match}} = \left| \frac{V_t}{2} \right| \left(1 - \frac{jX_t}{R_t} \right) \qquad (7.4)$$

where Vt is Thévenin source voltage.

A comparison of loaded harvester voltage arising from a conjugate matched load from

the two models and the experimental results is seen in Figure 7.5. As with the power modeling in

Section 7.3, the difference between the MATLAB and SPICE models are explained by the

SPICE model's inclusion of imperfect operational amplifiers with limited gain and bandwidth,

parasitics related to circuit implementation and instrumentation amplifiers, and the nonidealities

associated with the negative capacitance circuit implementation. The difference between the

measured loaded voltage and the modeled loaded voltage is attributed, as in the open-circuit

voltage measurements in Section 7.1, to experimental uncertainty and uncertainty in film

parameters.

The best experimental system was modeled to have a worst-case loaded voltage of

approximately 58 volts when exposed to 747 aircraft noise at a distance of 1000 feet. This

relatively low voltage is due to the imperfect impedance match, particularly at low
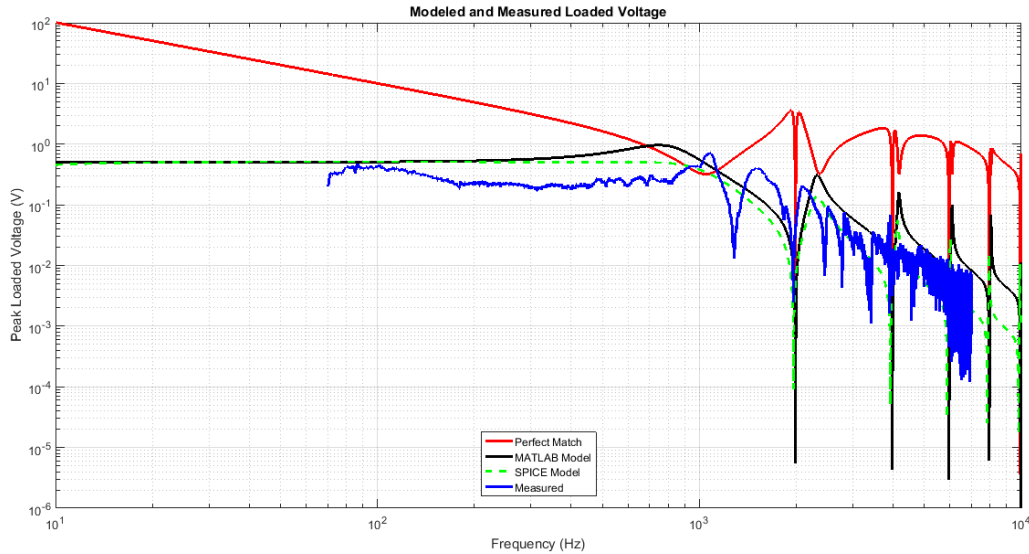
Figure 7.5. Comparison of modeled and measured loaded voltage given the best stable design of conjugate matched load.

frequencies. A 747 input noise given perfect impedance match would require a loaded voltage of 1387 volts. The high voltages required at low frequencies is explained by the requirement to displace increasingly large volumes of air at low frequencies, requiring increasingly large forces applied electrically to the harvester, while working against increasingly large compliant forces at large film displacements. Alternatively this could be interpreted as resulting from the high quality factor of the system. This high voltage requirement presents a significant challenge for broadband harvesting in real world scenarios, where acoustic sources are poorly controlled and a risk of saturating load circuitry exists. In a typical implementation, incoming acoustic pressure requiring a higher voltage than system supply voltage would result in saturation of the control system and a brief reduction in energy harvesting performance.

114

7.4 Chapter Summary

Experimental results are presented and compared against MATLAB and SPICE models developed in Chapter 3 and Chapter 5, respectively. Harvester source models are verified by experimental measurements of Vt (via open circuit voltage) given known acoustic input, and indirect measurements of Rt and Xt (via resistive load measurements). The model is shown to be accurate to within experimental uncertainty bounds, excepting higher order resonances which are omitted by the model. Finally, broadband harvesting performance given a negative capacitive load also validates the model. Stability challenges precluded a perfect broadband impedance match, in accordance with stability analysis performed in Chapter 5. However, despite this broadband harvesting performance was achieved exceeding that possible with a purely resistive load, and also exceeding that achieved with existing resonant acoustic energy harvester designs. A challenge in real-world systems arises from the high loaded voltage required for a broadband impedance match, particularly at low frequencies.

Chapter 8

Summary, Conclusions, Future Work

8.1 Summary and Conclusions

The technical challenge addressed in this work is the optimal harvesting of acoustic energy from a broadband acoustic noise source, and to do so on a large scale. Existing acoustic energy harvesters suffer from two main performance limitations. Existing harvesters tend to be MEMS-scale devices, with extremely small harvesting area and consequently small harvested energy. Existing harvesters are also limited in bandwidth, being based on highly-resonant acoustic structures. Such devices have limited utility in real-world applications where noise sources are unpredictable and generally broadband. This work addresses these two limitations. The size limitation is addressed by the design and analysis of a 10x10 cm electromechanical transducer based on piezoelectric film, and the development of an associated electromechanical model. Such a design is a size improvement many orders of magnitude greater than existing designs, with the potential to scale up further. The narrowband energy harvesting limitation is addressed by a reactive loading technique, providing in theory a broadband impedance match and therefore optimal energy transfer.

Chapter 2 introduces the background material required to understand the acoustic design, model, and theory behind optimal energy harvesting. Energy exists in the particle motion associated with sound, and is related to the sound intensity. Given certain assumptions and approximations, acoustic systems can be readily modeled as electrical circuits, with transducers providing transformation of impedances and energy between the mechanical and electrical domains. A review of various transduction technologies is presented. Piezoelectric film transduction is justified as the optimal transduction technology, as a result of it's low loss properties, low mass, tunable compliance, and low cost. Acoustic diffraction is presented, introducing challenges associated with diffraction effects, particularly at low frequencies. This justifies the design decision for an enclosed harvester. The maximum power transfer theory is presented, resulting in a requirement for broadband conjugate loading of the harvester's source impedance for optimal broadband energy transfer. An overview of existing acoustic energy harvesting and related technologies is presented, with a focus on the scale and bandwidth limitations described above.

Chapter 3 builds on the background presented in Chapter 2. Chapter 3 presents the design of an acoustic energy harvester based on piezoelectric Polyvinylidene Fluoride film, with an active harvesting area of 100 cm^2. An energy-based dynamic model is derived, resulting in an equivalent electromechanical circuit model for the harvester. The harvester's behavior is nonlinear, with nonlinear contributions arising from a cubic spring element and a bias-dependent transducer. The harvester is biased in film displacement, providing an improved electromechanical transduction and a DC bias point, used for linearizing the film's nonlinear dynamics. The bias point is provided by a partial vacuum in the film's enclosure. The bias point also provides for a tunable resonant frequency. The acoustic force arising from the film's

enclosure is modeled as a transmission line. The model is adjusted and improved for real-world effects associated with implementation. The result of the harvester is a complete linearized circuit model for the harvester's electroacoustic behavior. Due to the focus on low frequencies, the model only considers the fundamental film mode and omits higher-order modes. This model is used in later chapters for electrical load design for broadband energy harvesting.

Chapter 4 presents a mechanical implementation of the harvester design presented in Chapter 3. The harvester is implemented in a drum-like structure of approximately 10x10x10 cm, with a piezoelectric film suspended over a cavity. The harvester base is fabricated out of milled ABS plastic, and allows for a square active area of 10x10 cm. The bias point in film deflection is implemented as a vacuum in the harvester's cavity, which is produced by a hand vacuum pump and associated vacuum sealing system. The vacuum system presents a challenge for scaling of the technology, both due to fabrication and longevity challenges.

Chapter 5 describes the design of an electrical load which provides for broadband energy harvesting. This is implemented as a conjugate matched load of the harvester impedance, as described in Chapter 2. The conjugate matched load is directly informed by the harvester analytical model derived in Chapter 3. Here, a number of modeling simplifications are made, simplifying electrical design. The simplified harvester model very closely resembles a series resistor (18.8 ohms) and capacitor (16.47 nF) at the low frequencies characteristic of aircraft noise. The design's performance is shown in general to be insensitive to environmental conditions such as air temperature and pressure. The design is highly sensitive to load capacitance, requiring a 20pF precision of capacitance (~0.1%) for optimal, stable energy harvesting. This arises from the large reactive and relatively small real harvester impedance, resulting in significant reactive contributions to impedance mismatch for all but the closest of

118

load capacitance matches. This is consistent with related work in sound isolation [18],[19],[20],[21],[23],[24], and presents a challenge for real-world systems.

An analog circuit design is presented for electrical loading, based on an operational amplifier negative impedance converter circuit. While the losses from the operational amplifier circuit exceed the harvested power, in future work similar loads could be implemented using circuits with significantly reduced losses. The operational amplifier was selected for experimental purposes to validate the load matching concept, and harvested power was intentionally spent in a resistance rather than being delivered to a useful load. A number of stability challenges are identified in the electrical loading system, which are in general related to the requirement for matching a positive capacitance with a load negative capacitance. Stability challenges in particular are attributed to leakage resistance, resonance, and parasitic capacitance associated with circuit implementation. These stability challenges ultimately are the limiting factor in performance, precluding stable operation for load capacitances closer than 130pF from the target capacitance. The resulting harvested power from a 747 takeoff event at 1000 feet is 1.6uJ, approximately 0.25% of the maximum possible harvested power.

Chapter 6 presents an acoustic testbench for the energy harvester. The testbench is centered around an acoustic anechoic chamber, which allows for predictable sound pressure distributions, which are approximately free-field. An intricate calibration procedure is presented, resulting in 75 dB SPL acoustic drive with nearly flat frequency response from 70Hz – 7KHz. An automated test procedure is developed, allowing for rapid and precise testing. An electrical instrumentation design is presented, which allows for measurement of system behavior while minimizing impact on the system.

Chapter 7 presents four experiments. The first (Section 7.1) serves to directly validate the energy harvester's analytical model for the Thévenin source voltage, providing a measurement of this voltage when driven by a known acoustic source. The experimental data validates the model, within experimental uncertainty, while only considering the fundamental mode of film deflection. The second experiment (Section 7.2.1) measures the power delivered from the harvester to various purely resistive loads, given a known acoustic input. This serves as an indirect validation of the model's impedance predictions. As before, the experimental data matches the model's prediction within experimental uncertainty, when considering the fundamental mode of film behavior. The first two experiments combine to provide full validation of the electromechanical circuit model developed in Chapter 3, and simplifications presented in Chapter 5.

The third and fourth experiments measure system behavior when the harvester is loaded by the electrical load developed in Chapter 5, with the goal of optimal broadband conjugate impedance match of the harvester's source impedance. The third experiment (Section 7.2.2) measures power delivered to such a load, given a known acoustic input. While the designed load is in theory capable of providing a broadband impedance match and therefore efficient broadband energy harvesting, stability constraints and implementation parasitics preclude this. The closest impedance match stably achieved is a matched real part of 18.8 ohms, and a negative capacitance of approximately negative 16.6 nF, or 130 pF away from the target source equivalent capacitance. This is consistent with stability analysis completed in Section 5.4. While the design did not achieve the goal of efficient broadband energy harvesting from 100Hz-1KHz due to stability constraints, the design achieved an improved harvesting spectrum, and achieved broadband energy harvesting exceeding that which is possible with purely resistive loads or with

the resonant designs described in existing literature (Figure 7.4). The stability challenges, while not fundamental to broadband energy harvesting, are likely to be relevant in designs which apply the conjugate impedance match approach. These challenges are primarily related to the electrical load implementation and do not scale with harvester size, with the exception of harvester resonance, which would in general be expected to decrease in frequency with increased harvester scaling.

The fourth experiment (Section 7.3) measures the voltage at the harvester's outputs, when loaded by the conjugate load designed in Chapter 5. The close match between the measured and modeled loaded voltage further validates the harvester model. One challenge from real-world designs arises from the high loaded voltages required, particularly at high input pressure levels and low frequencies. While this work's load only requires 58 volts given a worst-case 747 takeoff at 1000 feet, this is due to the imperfect impedance match, particularly at low frequencies where the majority of the energy exists in aircraft noise. A perfect impedance match given these conditions would require a loaded voltage of approximately 1387 Volts.

8.2 Future Work

While this work demonstrates large-scale acoustic energy harvesting and an improvement towards efficient broadband energy harvesting, a number of opportunities exist for improvement and further research. The implemented design's stability considerations ultimately impacted the ability to stably produce a conjugate matched load, precluding efficient fully broadband energy harvesting. Opportunities exist to modify the existing load circuit, or explore alternative load circuit topologies to mitigate the adverse stability effects, allowing for a closer synthesis of broadband conjugate load and therefore broadband efficient energy harvesting.

While the operational amplifier circuit described is in theory capable of synthesizing the appropriate conjugate matched load given resolution of stability issues, the operational amplifier is an energy expensive implementation, and one that consumes more energy than is gained by it's inclusion in most acoustic energy harvesting applications. In addition, it does not deliver the power to a reservoir or a useful load, but rather intentionally spends power in a load resistor. A requirement exists for exploration of alternative load topologies that can synthesize an equivalent load with minimal losses. One such topology can be seen in Figure 2.11.

The existing design demonstrates an extreme sensitivity to load capacitance, requiring a precision of 0.1% for effective broadband energy harvesting, as seen in Figure 5.8. This is consistent with challenges reported in literature [18],[19],[20],[21],[23],[24]. Such a sensitivity presents a significant challenge for real-world designs, where typical component tolerances are 10%. An opportunity exists for exploration of mechanical and electrical changes to mitigate the extreme sensitivity to this parameter. For example, this may be achieved mechanically by a reduction in harvester output capacitance or effective spring constant with minimal effect on other parameters. It may be achieved electrically by the use of a dynamic circuit which updates load capacitance to most optimally harvest power while remaining stable.

The impedance match approach described in this work, while in theory capable of achieving efficient broadband energy harvesting, has high voltage requirements. This is particularly true at high input levels and low frequencies. A perfect impedance match with the existing design would require hundreds of volts at sound levels and spectra typical of real-world use (Figure 7.5). In many situations the losses incurred in the generation of such high voltages would be prohibitively large. An opportunity exists for the exploration of improved transducer design to reduce the required voltages. In particular, materials with improved electromechanical

122

coupling such as Macro Fiber Composite (MFC) may be able to achieve this due to their increased mechanical forces applied for a given electrical voltage. Alternative transducer geometries may also exist to this effect.

The transducer described in this work utilizes a vacuum system approach to provide a bias point in film deflection, improving transduction ability and facilitating linear analysis. The vacuum system, while effective in a research context, is not practical for real-world systems due to the energy cost, monetary cost and maintenance requirements. An opportunity exists for exploration of alternative biasing methods, such as constraining the film mechanically or heat embossing treatments. In addition, it is possible that alternative film geometries can bypass the biasing requirement entirely.

The approach described above employs an enclosure surrounding the film, which is necessary to mitigate the diffraction effects and associated performance loss. Such an approach may not be practical in real-world systems, or systems implemented in a larger scale. This is primarily due to the cost, size and weight associated with the structure. An opportunity exists to mitigate this requirement by use of other methods to mitigate diffraction effects, such as the use of other acoustic structures such as horns or phase-shifting structures such as those used in bass-reflex speaker cabinet designs.

The approach described in this work, while implemented on a scale larger than acoustic energy harvesters described in literature, has the potential to be scaled up even further. This would allow for even larger-scale energy harvesting. In addition, an effective energy harvester is also an effective sound absorber. The potential exists for the use of this technology in the context of large-scale sound absorption and isolation. Such a technology would have many applications, in the context of airports and other noisy industrial sites, home and commercial use, professional

audio applications, automotive, aerospace, and many others. A number of challenges are associated with the scaling of this technology. One such challenge is the breakdown of lumped-element assumptions as the size of the film increases. In addition, the sound absorption/energy harvesting performance is unexplored in the context of diffuse sound fields, near-field sound sources, and sound fields which are not perfectly orthogonal to the harvester surface.

Finally, an alternative application for the technology exists in the form of sound drivers. As explained by acoustic reciprocity, an effective active sound absorber is also an effective sound source. The potential exists for the use of the active impedance matching technology in the context of high-fidelity audio, using the conjugate impedance synthesis technology for effective broadband sound generation. Potential also exists for the use of efficient acoustic energy harvesting and sound generation within the same device.

Appendices

Appendix A

MATLAB Magnetic Harvester Model

```matlab
%Acoustic Energy Harvester Testbench
%Nathan Monroe, April 2016
clear all
close all
%%%%%%%%%%%%%%%%%%%%%%
%User parameters
%%%%%%%%%%%%%%%%%%%%%%
do_757 = 0; %tells program if it should use 757 data or constant power
spectrum
if do_757==0
    input_freq = 2*pi*linspace(100,10000,2000); %20k points between 1 and 100
rad / sec
    input_spectrum = 100*ones(1,2000); %dBSPL
else
    LogData = [24 32 36 38 41 38 39 42 40 38 38 37 36 36 36 37 36 32 30 30 24
19 11 7];
    LogData = 40 + LogData*80/70;
    LinData_W = 1e-12 * 10.^(LogData/10); %W/m^2/Hz
    LinData_Pa = sqrt(LinData_W * 420.5); %input spectrum in pressure
    LinData = 20*log10(LinData_Pa/(sqrt(2)*20e-6)); %input spectrum converted
to dBSPL (20uPa reference)
    n = 1; %number of points per third octave. nonzero integer.
    input_freq = 2*pi*logspace(1.7,4,24*n); %757 data extrapolated to finer
frequency resolution.
    input_spectrum = []; %757 data, dBSPL
    [row,col] = size(LinData);
    while col > 0 %generate finer resolution 757 data
        current = LinData(1);
        LinData = LinData(2:end);
        input_spectrum = [input_spectrum current*ones(1,n)/n];
        [row,col] = size(LinData);
    end
end
showplot=1; %set to 1 to plot output
n_turns = 1; %Number of turns
r_coil = 4; %radius of coil, cm
%Diameter of wire (um)
diam_wire = 5000; %40AWG wire = 80um
color = '-k';
%Mass of diaphgram (grams)
m_diaphragm = 5;
% resonant frequency of system (rad / s)
```

```matlab
w0_diaphragm = 450 * 2 * pi;
%Magnetic flux density (Wb/M^2)
B = 0.8;
harvester_area=.01; %cm^2. Default 100cm^2.
aeh_Model_thesis(n_turns,r_coil,diam_wire,m_diaphragm,w0_diaphragm,B,harveste
r_area,input_freq,input_spectrum,showplot,'-b');


%Acoustic Energy Harvester Model version 0.1
%Nathan Monroe, April 2016


function int_out =
aeh_Model_thesis(n_turns,r_coil,diam_wire,m_diaphragm,w0_diaphragm,B,harveste
r_area,input_freq,input_spectrum,showplot,color)
%%%%%%%%%%%%%%%%%%%%%%
%Constants
%%%%%%%%%%%%%%%%%%%%%%
%copper conductivity (ohm * m) at 20C
rho_cu=1.68*10^-8; %cu
%rho_cu=1/(3.5e7); %al
%copper density (grams per cm^3)
cu_density = 8.68; %cu
%cu_density = 2.7; %al
%vacuum permeability (H/m)
u0 = 4*3.14*10^-7;
%source acoustic impedance at STP (Pa/(M/s))
z0 = 420.5;
%%%%%%%%%%%%%%%%%%%%%%%%%%%%%%%%%%%%%%%%%%%%%
%copper cross-sectional area (cm^2)
cu_area = pi*((.5*diam_wire*(10^-4))^2);
%length_winding (cm)
length_winding = n_turns*2*pi*r_coil;
%winding resistance (ohms)
r_winding = (rho_cu*100*length_winding)/cu_area;
%winding mass (grams)
m_winding = cu_area * length_winding * cu_density;
%total intertial mass (grams)
total_mass = (m_diaphragm + m_winding)/1000; %want in Kg, not g
k_diaphragm = total_mass * (w0_diaphragm^2); %allows for entry of w0, not
diaphragm K.
a_winding = pi*(r_coil*.01)^2; %winding area (m^2)
%winding inductance (approximate) (henries). Assumes single layer of
%windings, no stacking.
l_winding = u0 * (n_turns^2)*a_winding/(diam_wire*(10^-6)*n_turns);
rd = (2*harvester_area*z0); %mechanical damping
P_in = sqrt(2)*(20e-6)*(10.^(input_spectrum/20)); %incoming pressure
%%%%%%%%%%%%%%%%%%%%%%
%Model
F=2*harvester_area*P_in;
G = length_winding * B; %Turns ratio of transducer. Set to zero for open loop
analysis.
%thevenin equivalent of force
Vt = j*input_freq*G.*F./(k_diaphragm-((total_mass*(input_freq.^2))-
(j*rd*input_freq)));
%real part of thevenin source impedance
Rt = r_winding+((G^2)*rd*(input_freq.^2))./(((k_diaphragm-
(total_mass*(input_freq.^2))).^2)+((rd*input_freq).^2));
```

127

```matlab
%reactive part of thevenin source impedance
Xt = (l_winding*input_freq) + (G^2)*input_freq.*(k_diaphragm-
(total_mass*(input_freq.^2)))./(((k_diaphragm-
(total_mass*(input_freq.^2))).^2)+((rd*input_freq).^2));
z_total = Rt + j*Xt; %total source impedance for matching
p_avail = 0.125*((abs(Vt).^2)./Rt); %available power from perfect match
int_out = sum(p_avail); %integrated power
if(showplot)
    loglog(input_freq/(2*pi),harvester_area*(P_in.^2)/(4*z0), '-r',
'LineWidth', 2);
    hold on;
    loglog(input_freq/(2*pi), p_avail,color, 'LineWidth', 2);
    xlabel('Frequency [Hz]')
    ylabel('Harvested Power [W]')
    title('Voice-Coil Converter : SPL = 100 dB');
    grid on;
end
end
```

Appendix B

MATLAB Piezoelectric Harvester Model

```
%Full_model_clean.m
%Linearized PVDF film model with back cavity
%Nathan Monroe
%Last Updated 5/24/2017

%clear all
%close all

format compact %matlab output more compact
format shortE %numbers in engineering format

%%%%%%%%%%%%%%%%%%%%%%
%User parameters
%%%%%%%%%%%%%%%%%%%%%%

    %noise source options:
    %   '757': Sonoma 757-200 data. Don't know if this is SEL, Lmax or other.
    %   '747_lmax': Heathrow 747-400 data. Use for voltage stress
    %   '747_SEL': Heathrow 747-400 data. Use for power estimate
    %   '777-1_lmax': Heathrow first 777-300ER data
    %   '777-2_lmax': Heathrow second 777-300ER data
    %   '747_wav': actual recording of 747, scaled for pascals. Use for
Loaded
    %   voltage, nothing else.
    %   'const': Constant input, flat in frequency.
    noise_source = 'const';
    SPL = 75; %input dBSPL for constant input. Not used for aircraft inputs

    %Output switches
    showPowerplot = 0; %set to 1 to plot power output given perfect match
    showmax = 1; %show maximum available power on power output plot
    plotcolor = '-k'; %color of plotted line for showmax above.
    showFreqplot = 0; %show Vt, Rt, Xt, voltage over frequency. Also
effective series capacitance.
    showLoadedVoltage = 0; %show loaded voltage over frequency. Assumes
perfect loading.
    showparams = 0; %print out text of calculated circuit components

    Vtcompare = 0; %Compare Vt predicted vs measured
    Vt_meaured_file = 'test_vt_thesis_5_9_17/vt_26p4mvpp.csv'; %file to plot
against predicted Vt
    Vt_scaling = 0.0264; %scaling for above file from dBSPL to volts pp
```

129

```matlab
    PowerCompare = 1; %compare measured power to estimated power for real
loading
    Exp_load_R = 18; %load resistance in real experiment
    Power_V_measured_file = 'test_5_16_17/v10_720mvpp.csv'; %measured loaded
voltage
    Power_V_scaling = 0.720; %scaling for above file from dBSPL to volts pp
    Power_V_scaling_freq = 0; %frequency to normalize scaling to. 0 means use
maximum point
    Power_I_measured_file = 'test_5_16_17/inb1_213mvpp.csv'; %measured
voltage representing delivered current
    Power_I_scaling = 0.213; %scaling for above file from dBSPL to volts pp
    I_amp_gain = 107; %gain of instrumentation amp to measure current


    %Output switches for actual, nonideal modeled load. Outputs power
frequency
    %resposne and loaded voltage frequency response.
    load_type = 'RC'; % options for actual loading: 'none', 'R', 'RL', 'RCp'
'RC', 'RLC', 'RLCC'
    ShowActualLoadedVoltage = 0; %show loaded voltage for a nonideal load
    ShowActualLoadedPower = 0; %show power for a nonideal load
    Cp_load = 0;    %parallel load capacitance, farads
    Rs_load = 18.8; %series load resistance, ohms
    Cs_load = -16.6e-9; %series load capacitance, farads.
    Ls_load = 0; %series load inductance, Henries.


    %Input variables
    include_backcavity = 1; %include back cavity effects or not
    distance = 304.8; %distance from source, meters. Default 1000ft = 304.8m.
    L = 0.1; %length of diaphragm, meters
    th = 110e-6; %thickness of diaphragm, meters. Default value is 110um.
Don't confuse with t, time
    r_piezo = 100e-3; %Harvester ESR, ohms.
    P_bias = 10000; %bias pressure, Pascals. 1Atm = 101.3KPa (full vaccuum).
Default 10KPa
    air_th = 0.00635; %thickness of associated air mass, in meters. Default
6.35mm=1/4in.
    electrode_area = 0.00889; %electrode area. Adds to capacitance. Square
Meters. Default 0.00889 = 88.9cm^2 based on solidworks design.
    cavity_depth = 0.09; %depth of the back cavity, meters. Default 9cm to
match experiment
    P_atm = 101325; %atmospheric pressure, Pascals. Affects Z0 and P0.
Default 101325 Pa = 1atm.
    T_air = 20; %air temp, Celsius. Affects Z0 and P0. Default 20C


    %%%%Physical constants, these shouldn't change.
    E = 2.5e9; %Young's modulus of PVDF, Pascals. 2.5GPa default from
datasheet
    v = 0.3; %Poisson Ratio of PVDF, unitless
    d31 = 23e-12; %Piezo coefficient of poled PVDF, C/N 23e-12 default.
    epsilon_3 = 11 * 8.85e-12; %Dielectric constant of PVDF, Farads/meter.
e_r = 11 from datasheet
    rho = 1780; %mass density of PVDF, kg/m^3
    gamma = 1.4; %adiabatic constant of air, unitless.
    Rsp = 287.058; %specific gas constant for air, J/(Kg*K). Assumes dry air.
```

```matlab
    %A weighting curve that's been applied to 757 data. Subtract this to
    %counteract it.
    a_weight = [-30.2,-26.2,-22.5,-19.1,-16.1,-13.4,-10.9,-8.6,-6.6,-4.8,-
3.2,-1.9,-0.8,0,0.6,1.0,1.2,1.3,1.2,1,0.5,-0.1,-1.1,-2.5];

    %Generate frequency content from the input text above
    if strcmp(noise_source,'const') %this option inputs a constant white
noise, intensity controlled by variable "SPL".
        input_omega = 2*pi*logspace(1,4,200000); %200k points between 1 and
100
        input_spectrum_dbspl = SPL*ones(1,200000); %dBSPL
        P_in = (20e-6)*(10.^(input_spectrum_dbspl/20)); %incoming pressure,
Pa RMS

    elseif strcmp(noise_source,'757') %use 757 data, converted to dBspl.
Preprocessing for input to analysis function.
        LogData = [24 32 36 38 41 38 39 42 40 38 38 37 36 36 36 37 36 32 30
30 24 19 11 7]; %frequency content for 757-200
        LogData = 40 + LogData*80/70;
        LinData_W = 1e-12 * 10.^(LogData/10); %W/m^2/Hz
        LinData_Pa = sqrt(LinData_W * 420.5); %input spectrum in pressure.
        LinData = 20*log10(LinData_Pa/(sqrt(2)*20e-6)); %input spectrum
converted to dB (20uPa reference). This isn't exactly labeled right, should
be logdata something.
        input_omega = 2*pi*logspace(1.7,4,24); %757 data frequency points.
        input_spectrum_dbspl = LinData; %757 data, dBSPL
        input_spectrum_dbspl = input_spectrum_dbspl - a_weight; %undo A
weighting
        P_in = (20e-6)*(10.^(input_spectrum_dbspl/20)); %incoming pressure,
Pa RMS

    %the below assumes the heathrow data was taken at 590 meters

    elseif strcmp(noise_source,'747_lmax') %use heathrow 747-400 data.
Normalize to 1000ft distance
        input_omega = 2*pi*logspace(1.7,4,24);
        input_spectrum_dbspl = 20*log10((590/distance)) +
[95.7,96.5,96,94.1,90.7,83.7,77,75.2,74.7,71.8,70.2,69.8,68.2,70.1,67.7,64.8,
63.2,65.8,67.5,70,61.9,61.8,53.4,44.4];
        P_in = (20e-6)*(10.^(input_spectrum_dbspl/20)); %incoming pressure,
Pa RMS

    elseif strcmp(noise_source,'747_SEL') %use heathrow 747-400 SEL data.
Normalize to 1000ft distance.  No A weighting here.
        input_omega = 2*pi*logspace(1.7,4,24);
        input_spectrum_dbspl = 20*log10((590/distance)) +
[103.7,103.6,102.7,100.6,96.7,90.3,84.1,81.6,79.1,77.4,76.5,77.2,76.4,77.1,76
.2,73.7,72.2,74.1,76,77.7,70.6,69.9,60.7,51.1];
        P_in = (20e-6)*(10.^(input_spectrum_dbspl/20)); %incoming pressure,
Pa RMS

    elseif strcmp(noise_source,'777-1_lmax') %use heathrow 777-300ER #1 data.
Normalize to 1000ft distance
        input_omega = 2*pi*logspace(1.7,4,24);
```

```matlab
        input_spectrum_dbspl = 20*log10((590/distance)) +
[88.5,85.2,82.1,78.5,72.6,66.6,63.2,59.7,57,58.4,61.4,62.2,64.7,64.3,64.2,65.
3,67.1,66,68,66.7,61.4,55.4,41.1,33.7];
        P_in = (20e-6)*(10.^(input_spectrum_dbspl/20)); %incoming pressure,
Pa RMS

    elseif strcmp(noise_source,'777-2_lmax') %use heathrow 777-300ER #2 data.
Normalize to 1000ft distance
        input_omega = 2*pi*logspace(1.7,4,24);
        input_spectrum_dbspl = 20*log10((590/distance)) +
[94.5,92.8,90.4,85.8,81.4,74.9,69.4,66.5,66.8,65.2,65.6,67.3,70.6,65.5,63.3,6
3.2,59.6,64.4,63.4,61,54.9,53,40.1,29.5];
        P_in = (20e-6)*(10.^(input_spectrum_dbspl/20)); %incoming pressure,
Pa RMS

    elseif strcmp(noise_source,'747_wav')
        scaling = 19.5;
        [y,Fs] =
audioread('C:\Users\Nathan\Desktop\thesis\Noise2EnergyProject\Noise2EnergyPro
ject\WAV files\Aircraft6.wav');
        t_start = 9; %start and end of clipped portion
        %t_end = 10;
        y_chunk = scaling*y(t_start*Fs:(t_start+1)*Fs); %clip the portion,
scale it for Pa.
        y_chunk_hann = y_chunk-mean(y_chunk).* hann(numel(y_chunk));
        nfft = 2^17; %0.39Hz, 2.56sec
        Xy = fft(y_chunk_hann,nfft);
        k = 0:1:nfft-1;
        dF = Fs/nfft;
        f = (dF*(0:nfft-1))-Fs/2';
        Xy = fftshift(Xy);
        leng = numel(f);
        f = f((leng/2)+1:end);
        Xy = 2*Xy((leng/2)+1:end)/n;
        Xy = Xy /(sqrt(2)); %RMS pressure
        P_in = Xy';
        P_in = P_in(2:end); %ignore DC component
        f = f(2:end);
        input_omega = f*2*pi;
    end


    %%%%%%%%%%%%%%%%%%%%%%%%%%%%%%%
    %%%Begin Model
    %%%%%%%%%%%%%%%%%%%%%%%%%%%%%%%%

    %Medium properties.
    T_air_K = T_air + 273.15; %air temp in Kelvin.
    air_rho = P_atm/(Rsp*T_air_K); %mass density of air based on local
pressure.
    c0 = sqrt(gamma*Rsp*T_air_K); %speed of sound in air, based on temp.
    z0 = gamma*P_atm/c0; %source impedance, based on pressure and c0 -> temp.

    %Source Properties.
    u0 = P_in/z0; %Corresponding particle velocity, m/s
```

```matlab
    %Harvester Properties.
    K_nonlinear = (1.5+v)*(E*(pi^4)*th/(16*(L^2)*(1-(v^2)))); %K cubic
    P0 = nthroot(((2*L/pi)^2)*P_bias/K_nonlinear,3); %static deflection P0,
meters.
    M = ((rho*th*(L^2)/4) + ((L^2)*0.25*air_th*air_rho)); %mass, including
air layer's effective contribution.
    B = 0.5*z0*(L^2); %damping from input thevenin
    K_linear = (3*(P0^2))*K_nonlinear; %linearized spring constant evaluated
at static displacement P0
    K_total = K_linear; %if no back cavity effect the only K contribution is
from the film
    if (include_backcavity) %if this flag is true, include back cavity
effects
        eff_cav_depth = cavity_depth - 0.5*P0; %effective cavity depth,
reduced slightly by film deflection
        K_Cavity = (z0*(L^2))*cot(input_omega*eff_cav_depth/c0).*input_omega;
%spring (or mass) contribution of back cavity
        K_total = K_linear + K_Cavity; %total spring contribution from film
and cavity. K is now a frequency-dependent vector.

    end

    D = P0*(pi^2)*E*d31*0.5/(1-v); %linearized transformer turns ratio,
evaluated at P0. First mode shape only
    C = (((L^2)/th)*(epsilon_3 - (2*E*(d31^2)/(1-
v))))+(electrode_area*epsilon_3/th); %capacitance. Includes electrode area
capacitance

    %%%%%%%%%%%%%%%%%%%%%
    %Model
    F = 2*z0*((2*L/pi)^2)*u0; %input force of first mode
    %thevenin equivalent of force RMS
    Vt = D*F./(C*(K_total + ((D^2)/C)-
(M*(input_omega.^2))+(1j*B*input_omega)));

    %real part of thevenin source impedance
    Rt = r_piezo + ((D^2)*B/(C^2))./(((K_total + ((D^2)/C)-
(M*(input_omega.^2)))).^2)+((input_omega*B).^2));

    %reactive part of thevenin source impedance
    Xt = -((K_total + ((D^2)/C)-(M*(input_omega.^2))).*(K_total-
(M*(input_omega.^2)))+((B*input_omega).^2))./(C*input_omega.*(((K_total +
((D^2)/C)-(M*(input_omega.^2)))).^2)+((input_omega*B).^2)));

    %Quality factor
    Q = abs(0.5*(Xt./Rt));

    %Various Harvested Power Measures
    p_harvest = 0.125*((abs(Vt).^2)./Rt); %amount harvested by ideal
harvester (W)
    p_max_possible = (L^2)*(P_in.*conj(P_in))/(4*z0); %maximum possible
power, design agnostic
    p_max_possible_this = (64/(pi^4))*p_max_possible; %maximum possible for
film design. Factor of (pi^4)/64 from edge constraints.
```

```matlab
    %loaded terminal voltage with ideal matched load
    v_loaded = sqrt(2)*abs((Vt/2).*(1-(j*Xt./Rt))); %factor of sqrt(2) gives
peak- Vt is in RMS

    %v_loaded_ifft = ifft(v_loaded_comp,nfft);
    %figure();
    %plot(v_loaded_ifft);

    total_v_loaded_peak = sum(v_loaded) %peak voltage (not peak to peak)

    Int = sum(p_harvest) %total power

    %Available power in 1 square meter. For debug
    Available_power_1sqm = (4/(L^2))*sum(p_max_possible);

    if(showPowerplot) %show frequency response of power collection.
        figure();
        if(showmax)
            loglog(input_omega/(2*pi),p_max_possible,'-r', 'LineWidth', 1);
            hold on;
            loglog(input_omega/(2*pi),p_max_possible_this,'--r', 'LineWidth',
1);
        end
        loglog(input_omega/(2*pi), p_harvest,plotcolor, 'LineWidth', 1);
        xlabel('Frequency (Hz)');
        ylabel('Power (W)');
        title(strcat('Biased Linearized Sheet Converter: L = ',num2str(L),',
R= ', num2str(r_piezo)));
        grid on;
        legend('Max possible power','Diaphragm Max Possible Power', 'This
Design Power', 'Location','South')

    end
    if (showFreqplot) %show Vt,Rt,Xt magnitudes over frequency. Also Ct
        figure;
        loglog(input_omega/(2*pi),abs(Xt), 'LineWidth', 2);
        hold on;
        loglog(input_omega/(2*pi),abs(Vt), '-r', 'LineWidth', 2);
        loglog(input_omega/(2*pi),abs(Rt), '-k', 'LineWidth', 2);
        loglog(input_omega/(2*pi),Q, '-g', 'LineWidth', 2);
        grid on;
        xlabel('Frequency (Hz)');
        ylabel('Ohms real/reactive, Volts');
        legend('Xt','Vt (RMS)','Rt','Q', 'Location','West')
        title('Vt, Rt, Xt, Q Predicted Frequency Dependence');
        figure();
        loglog(input_omega/(2*pi),abs(1./((Xt).*input_omega)), 'LineWidth',
2);
        xlabel('Frequency (Hz)');
        ylabel('Equivalent Load Capacitance, Farads');
        title('Equivalent Load Capacitance');
        grid on;
    end
```

```matlab
    if (showLoadedVoltage) %show the loaded voltage frequency spectrum
        figure;
        loglog(input_omega/(2*pi), v_loaded, 'LineWidth', 2); %loaded
terminal voltage over frequency
        grid on;
        ylabel('Voltage (peak)');
        xlabel('Frequency (Hz)');
        title('Loaded Voltage Spectrum (peak, not pp)- assumes ideal load');
    end

    if (showparams) %print out text of parameters
        P0
        C
        D
        K_linear
        K_nonlinear
        M
        B
    end

    if (Vtcompare) %plot Vt predicted against a specified measured Vt
        [meas_freq, meas_volts] = SPL2V(Vt_meaured_file, Vt_scaling);
        figure();
        loglog(input_omega/(2*pi),abs(Vt)*2*sqrt(2), '-k', 'LineWidth', 2);
        hold on;
        spice = load('spice_vos_thesis_2.txt'); %pull out numbers from SPICE
output
        sf = spice(:,1);
        svr = spice(:,2);
        svi=spice(:,3);
        v_spice_pp = 2*sqrt((svr.^2)+(svi.^2));
        loglog(sf,v_spice_pp,'--g','linewidth',2);
        loglog(meas_freq,meas_volts,'-b','LineWidth',2);
        grid on;
        ylim([1e-6 1e-1]);
        ylabel('Voltage (peak-peak)');
        xlabel('Frequency (Hz)');
        title('Predicted and Measured Open Circuit Voltage');
        legend('Vt, MATLAB Model','Vt, SPICE Model','Vt,
Measured','Location','West')

    end

    [maxvt_rms,w0_index] = max(abs(Vt));
    maxvt_pp = 2 * sqrt(2) * maxvt_rms %peak to peak OCV at resonance
    f0 = input_omega(w0_index)/(2*pi) %corresponding resonant frequency

    %load_type,R_load,C_load,L_load
    if (~strcmp(load_type,'none')) %nonideal loadings
        Z_Cs = -j./(Cs_load * input_omega); %impedances for reactive
imaginary components
        Z_Ls = j*Ls_load*input_omega;
        Z_Cp = -j./(Cp_load * input_omega);
        Z_Rs = Rs_load;
        if (strcmp(load_type,'R'))
```

135

```matlab
            Z_load = Z_Rs;
        end
        if (strcmp(load_type,'RL'))
            Z_load = Z_Rs + Z_Ls;
        end
        if (strcmp(load_type,'RC'))
            Z_load = Z_Rs + Z_Cs;
        end
        if (strcmp(load_type,'RCp'))
            Z_load = (Z_Rs.*Z_Cp)./(Z_Rs + Z_Cp);
        end
        if (strcmp(load_type,'RLC'))
            Z_load = Z_Rs + Z_Cs + Z_Ls;
        end
        if (strcmp(load_type,'RLCC'))
            Z_load = Z_Cp.*(Z_Cs + Z_Ls + Z_Rs)./(Z_Cp + Z_Cs + Z_Ls + Z_Rs);
%load impedance with a parallel cap and series RLC
        end
        P_actual_load =
0.5*(abs(Vt).^2).*real(Z_load)./(abs(Z_load+(j*Xt)+Rt).^2); %power delivered
to a real load

        if (ShowActualLoadedVoltage)

            V_actual_load = sqrt(2)*abs(Vt.*Z_load./(Z_load+j*Xt+Rt));
%loaded voltage peak (not pp)

            %V_actual_load_t = ifft(V_actual_load,n);
            %figure();
            %plot(V_actual_load_t);

            total_V_actual_load = sum(V_actual_load)
            figure();
            loglog(input_omega/(2*pi), v_loaded,'r', 'LineWidth', 2);
%theoretical loaded terminal voltage over frequency
            hold on;
            loglog(input_omega/2/pi,V_actual_load,'k', 'LineWidth', 2);
            grid on;
            ylabel('Peak Loaded Voltage (V)');
            xlabel('Frequency (Hz)');
            legend('Loaded voltage (peak)- this modeled match','Theoretical
loaded voltage (peak)- perfect match', 'Location','South')
            title('Modeled and Measured Loaded Voltage')
            if(PowerCompare)
                spice = load('spice_loaded_v_match_thesis.txt');
                sf = spice(:,1); %spice frequency vector
                svr = spice(:,2); %spice real part of output power vector
                svi=spice(:,3); %spice imaginary part of output power vector
                sv = sqrt((svr.^2)+(svi.^2)); %spice power magnitude
                loglog(sf,sv,'--g','LineWidth',2); %plot spice trace
                [meas_freq_PV, meas_volts_PV, meas_phase_PV] =
SPL2V(Power_V_measured_file, Power_V_scaling,Power_V_scaling_freq); %pull in
measured loaded voltage
                loglog(meas_freq_PV,meas_volts_PV,'b', 'LineWidth', 2);
                legend('Perfect Match','MATLAB Model', 'SPICE
Model','Measured', 'Location','South')
```

```matlab
                xlim([10 10000])
                ylim([1e-6 100])
            end
        end


        int_actual = sum(P_actual_load) %harvested power from actual loading
        if (ShowActualLoadedPower)
            figure();
                if(showmax)
                    loglog(input_omega/(2*pi),p_max_possible,'-r',
'LineWidth', 2);
                    hold on;
                    loglog(input_omega/(2*pi),p_max_possible_this,'--r',
'LineWidth', 2);
                end
            loglog(input_omega/(2*pi), P_actual_load ,'k', 'LineWidth', 2);
            hold on;


            [f1, v1] =
SPL2V('test_vt_thesis_5_9_17/1k_3p16mvpp.csv',0.00316);
            spice = load('spice_1k_power_thesis.txt');
            sf = spice(:,1); %spice frequency vector
            spr = spice(:,2); %spice real part of output power vector
            spi=spice(:,3); %spice imaginary part of output power vector
            sp = sqrt((spr.^2)+(spi.^2)); %spice power magnitude
            loglog(sf,sp,'--g','LineWidth',2); %plot spice trace
            p1 = (v1.^2)/1000; %modeled power from 1k load
            loglog(f1,p1,'b','linewidth',2);
            xlabel('Frequency (Hz)');
            ylabel('Power (W)');
            title('Power delivered to a 1k load');
            ylim([1e-16 1e-6]);
            grid on;
            legend('Max possible','Diaphragm Max Possible', 'MATLAB
Model','SPICE Model','Measured', 'Location','South')
        end

        if(PowerCompare) %compare measured power to estimated power for an
actual load.
            [meas_freq_PV, meas_volts_PV, meas_phase_PV] =
SPL2V(Power_V_measured_file, Power_V_scaling,Power_V_scaling_freq); %pull in
measured loaded voltage
            [meas_freq_PI, meas_volts_PI, meas_phase_PI] =
SPL2V(Power_I_measured_file, Power_I_scaling); %pull in measured current
            meas_V_load_R = meas_volts_PI / I_amp_gain; %measured voltage
across load resistor
            meas_I = meas_V_load_R / Exp_load_R; %measured current through
load resistor
            meas_P = 0.5*(meas_I.^2)*Exp_load_R; %power to resistor
calculated with IV.
            %meas_P_alt = -0.5 * meas_volts_PV .* meas_I
.*cosd((meas_phase_PV-meas_phase_PI)); %alternative power measurement
            figure();
            loglog(input_omega/(2*pi),p_max_possible,'-r', 'LineWidth', 2);
%max possible power
            hold on;
```

```matlab
            loglog(input_omega/(2*pi),p_max_possible_this,'--r', 'LineWidth',
2); %max possible power with diaphragm limitations
            loglog(meas_freq_PV, meas_P,'b', 'LineWidth', 2); %power measured
by experiment, calculated by IV way
            loglog(input_omega/(2*pi), P_actual_load ,'k', 'LineWidth', 2);
%power as predicted by model with real load
            spice = load('spice_power_bestmatch_thesis.txt');
            sf = spice(:,1); %spice frequency vector
            spr = spice(:,2); %spice real part of output power vector
            spi=spice(:,3); %spice imaginary part of output power vector
            sp = sqrt((spr.^2)+(spi.^2)); %spice power magnitude
            %loglog(sf,sp,'--g','LineWidth',2); %plot spice trace
            load('horowitz_digitized_thesis.dat'); %horowitz data
            horo_f = horowitz_digitized_thesis(:,1);
            horo_eff = horowitz_digitized_thesis(:,2);
            loglog(horo_f,horo_eff*2*7.64e-8,'g','linewidth',2); % plot
horowitz data, normalized to this work.
            %loglog(meas_freq_PV, meas_P_formal_way, 'LineWidth', 2); %power
measured by experiment, calculated by formal PF way
            xlabel('Frequency (Hz)');
            ylabel('Power (W)');
            xlim([10 10000]);
            title('Power Comparison');
            grid on;
            legend('Max Possible','Diaphragm Max Possible','This Work, best
conjugate match load', 'This Work, modeled ideal resistive
load=100k','Horowitz et al, 2005','Location','South')
        end
    end

    %capacitor value needed to match at target_freq.
    target_freq = 100; %100Hz for perfet match
    [foo, index] = min(abs((input_omega/2/pi)-target_freq));
    eq_cap = abs(1./((Xt).*input_omega));
    cap_80Hz = abs(1./((Xt(index)).*input_omega(index)));


%SPL2V.m
%Nathan Monroe
%1/9/2017
%Takes in a frequency response CSV generated by REW in dBSPL,
%Outputs volts
%Needs one data point of dBSPL to volt for scaling.

function [freq, volts, phase] = SPL2V(file, setV,setfreq)
%takes in filename and voltage at a set frequency (or max), and optionally
frequency
%of that set voltage.
    M = csvread(file,14,0);
    freq = M(:,1);
    SPL = M(:,2);
    phase = M(:,3);
    volts_unscaled = 10.^(SPL/20); %convert it to linear
    switch nargin
        case 3
            if setfreq == 0
```

```matlab
                volts = volts_unscaled * setV/max(volts_unscaled); %scale it
for measured voltage at peak
            else
            [~, ind] = min(abs(freq-setfreq));
            volts = volts_unscaled * setV/volts_unscaled(ind); %scale it for
a certain frequency
            end
        otherwise %scale for peak voltage
            volts = volts_unscaled * setV/max(volts_unscaled); %scale it for
measured voltage at peak
    end

end
```
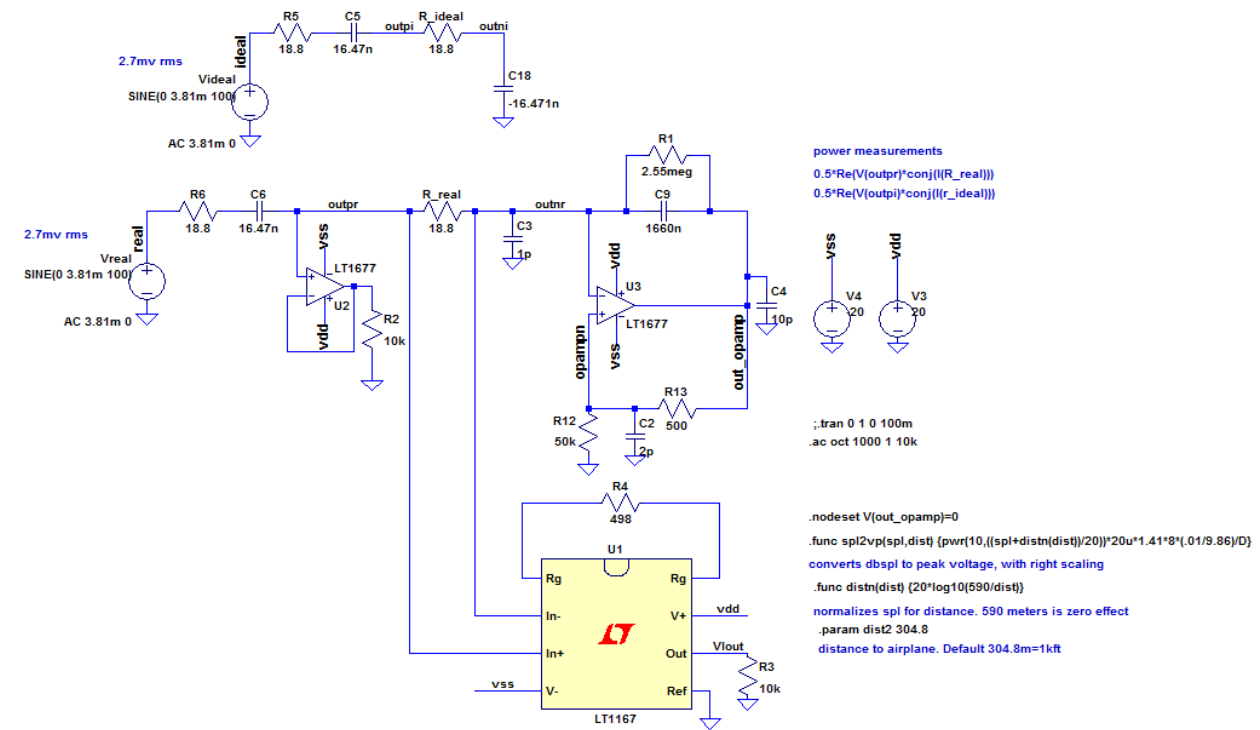
Appendix C

SPICE Harvester Model

Simplified harvester model as in Section 5.1 with ideal loading and implemented loading as discussed in Section 5.3, and harvester instrumentation as discussed in Section 6.3. Below: corresponding SPICE netlist.
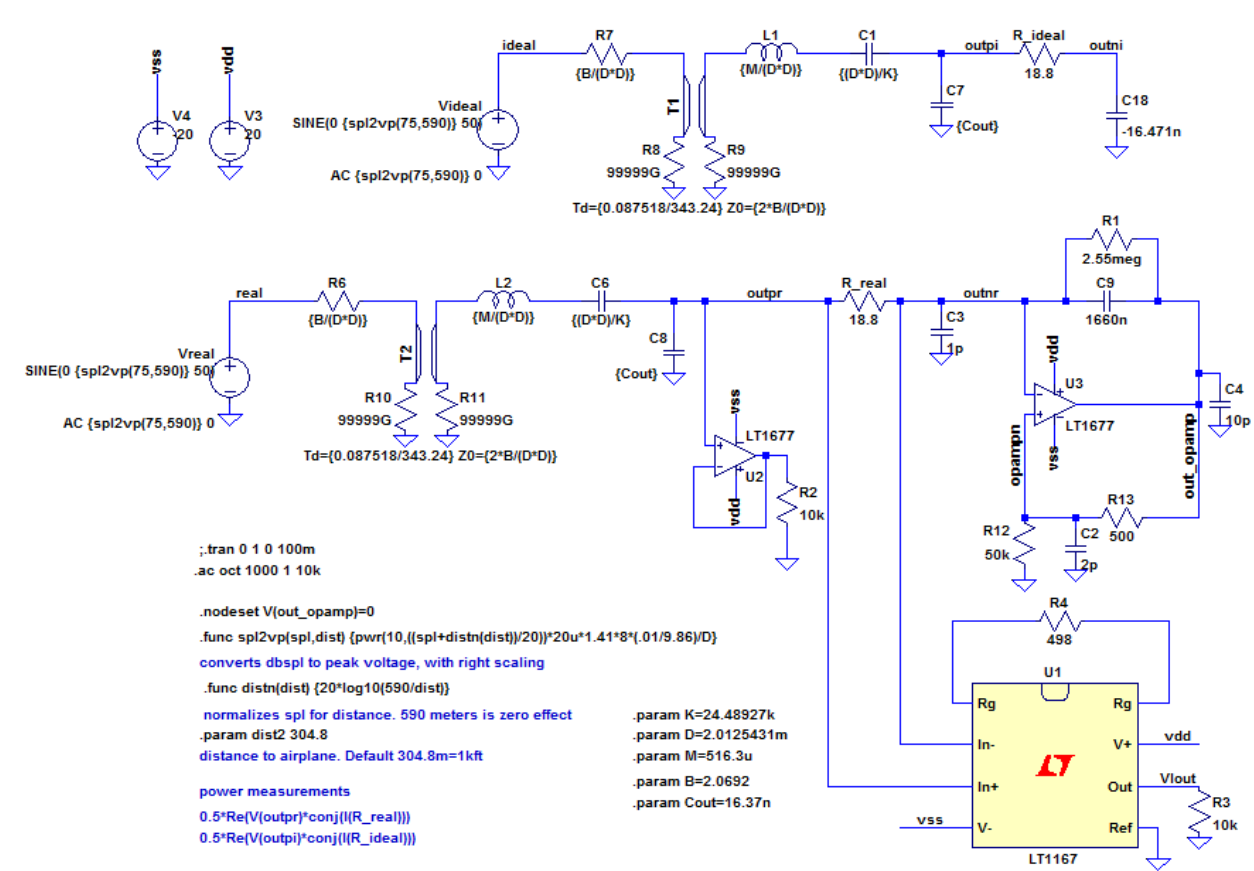
```
V3 vdd 0 20
V4 vss 0 -20
R_real outpr outnr 18.8
R12 0 opampn 50k
R13 out_opamp opampn 500
C9 out_opamp outnr 1660n Rser=0 Lser=0 Rpar=0 Cpar=0
C18 outni 0 -16.471n Rser=0 Lser=0
R_ideal outpi outni 18.8
XU3 opampn outnr vdd vss out_opamp LT1677
XU1 N004 outnr outpr vss 0 VIout vdd N005 LT1167
R3 VIout 0 10k
R4 N005 N004 498
R1 out_opamp outnr 2.55meg
C2 opampn 0 2p
C3 outnr 0 1p
C4 out_opamp 0 10p
R5 N001 ideal 18.8
C5 outpi N001 16.47n
Videal ideal 0 SINE(0 3.81m 100) AC 3.81m 0
R6 N002 real 18.8
C6 outpr N002 16.47n
Vreal real 0 SINE(0 3.81m 100) AC 3.81m 0
XU2 outpr N003 vdd vss N003 LT1677
R2 N003 0 10k
.ac oct 1000 1 10k
;.tran 0 1 0 100m
.func spl2vp(spl,dist)
{pwr(10,((spl+distn(dist))/20))*20u*1.41*8*(.01/9.86)/D}
* converts dbspl to peak voltage, with right scaling
.func distn(dist) {20*log10(590/dist)}
* normalizes spl for distance. 590 meters is zero effect
.param dist2 304.8
* distance to airplane. Default 304.8m=1kft
.nodeset V(out_opamp)=0
* power measurements
* 0.5*Re(V(outpr)*conj(I(R_real)))
* 0.5*Re(V(outpi)*conj(I(r_ideal)))
* 2.7mv rms
* 2.7mv rms
.lib LTC.lib
.backanno
.end
```

Full, linearized harvester model as in Section 3.10 with ideal loading and implemented loading as discussed in Section 5.3, and harvester instrumentation as discussed in Section 6.3. Below: corresponding SPICE netlist.


```
V3 vdd 0 20
V4 vss 0 -20
R_real outpr outnr 18.8
R12 0 opampn 50k
R13 out_opamp opampn 500
C9 out_opamp outnr 1660n Rser=0 Lser=0 Rpar=0 Cpar=0
C18 outni 0 -16.471n Rser=0 Lser=0
XU3 opampn outnr vdd vss out_opamp LT1677
XU1 N012 outnr outpr vss 0 VIout vdd N013 LT1167
R3 VIout 0 10k
R4 N013 N012 498
R1 out_opamp outnr 2.55meg
C2 opampn 0 2p
C3 outnr 0 1p
C4 out_opamp 0 10p
R_ideal outni outpi 18.8
XU2 outpr N011 vdd vss N011 LT1677
R2 N011 0 10k
R7 N001 ideal {B/(D*D)}
L1 N002 N003 {M/(D*D)} Rser=0
```

```
C1 outpi N003 {(D*D)/K}
C7 outpi 0 {Cout} Rser=0 Lser=0
R8 0 N004 99999G
R9 0 N005 99999G
Videal ideal 0 SINE(0 {spl2vp(75,590)} 50) AC {spl2vp(75,590)} 0
T1 N004 N005 N001 N002 Td={0.087518/343.24} Z0={2*B/(D*D)}
R6 N006 real {B/(D*D)}
L2 N007 N008 {M/(D*D)} Rser=0
C6 outpr N008 {(D*D)/K}
C8 outpr 0 {Cout} Rser=0 Lser=0
R10 0 N009 99999G
R11 0 N010 99999G
Vreal real 0 SINE(0 {spl2vp(75,590)} 50) AC {spl2vp(75,590)} 0
T2 N009 N010 N006 N007 Td={0.087518/343.24} Z0={2*B/(D*D)}
.ac oct 1000 1 10k
;.tran 0 1 0 100m
.func spl2vp(spl,dist)
{pwr(10,((spl+distn(dist))/20))*20u*1.41*8*(.01/9.86)/D}
* converts dbspl to peak voltage, with right scaling
.func distn(dist) {20*log10(590/dist)}
* normalizes spl for distance. 590 meters is zero effect
.param dist2 304.8
* distance to airplane. Default 304.8m=1kft
.nodeset V(out_opamp)=0
* power measurements
* 0.5*Re(V(outpr)*conj(I(R_real)))
* 0.5*Re(V(outpi)*conj(I(R_ideal)))
.param M=516.3u
.param B=2.0692
.param D=2.0125431m
.param K=24.48927k
.param Cout=16.37n
.lib LTC.lib
.backanno
.end
```
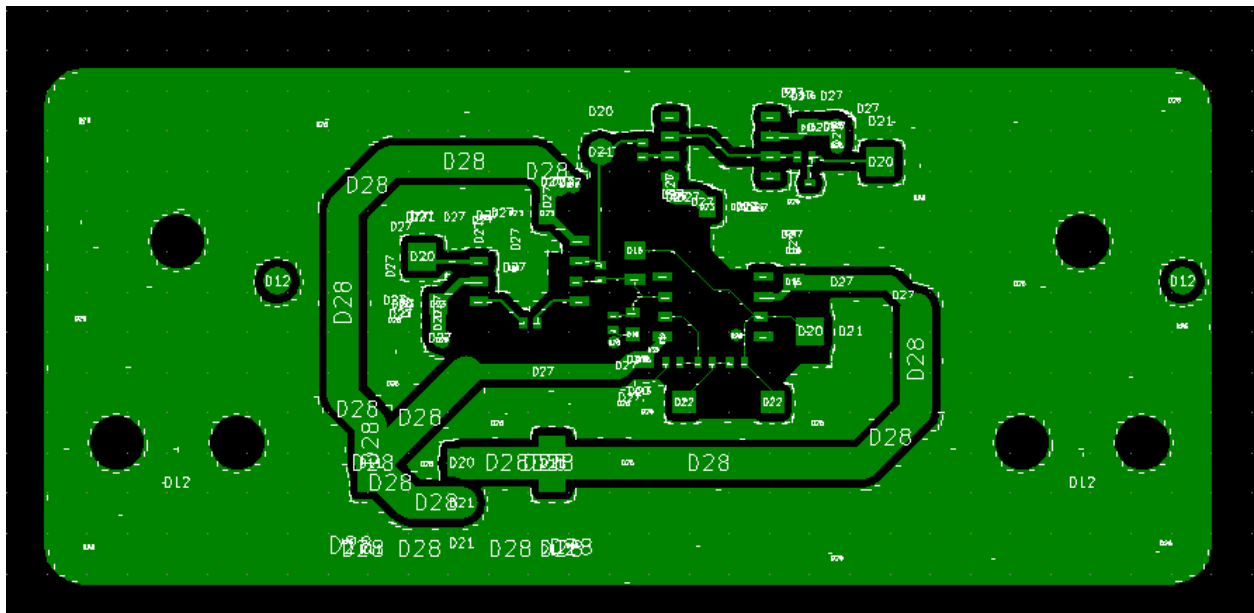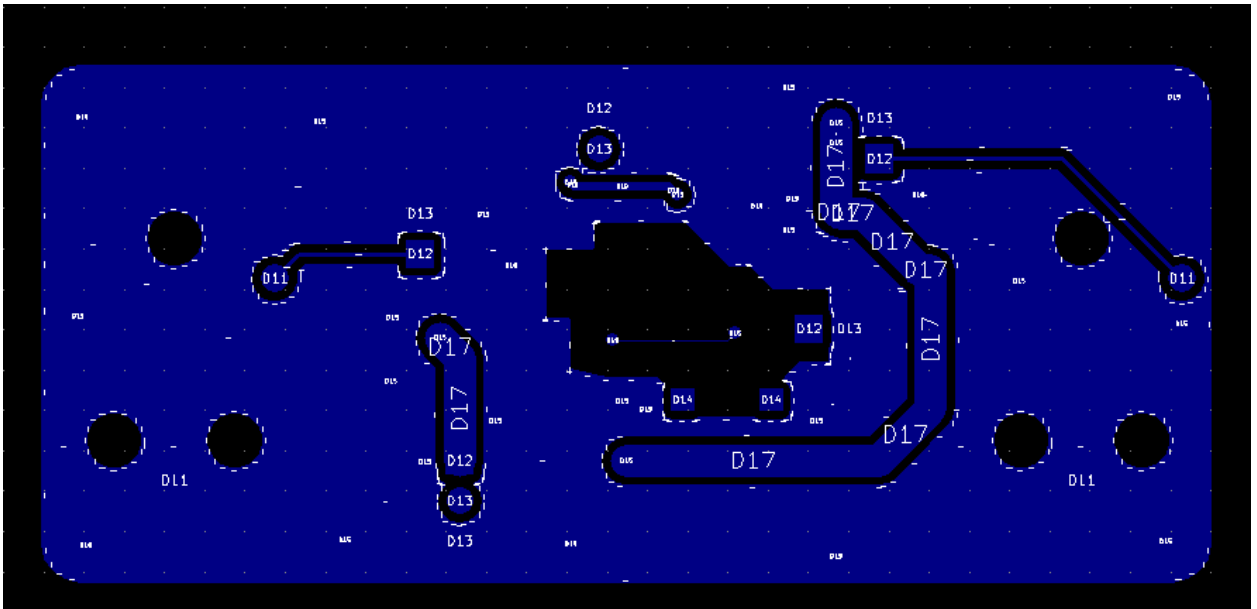
Appendix D

Circuit Board Layout

Acoustic energy harvester circuit board, as designed in Section 5.4, with instrumentation as described in Section 6.3.
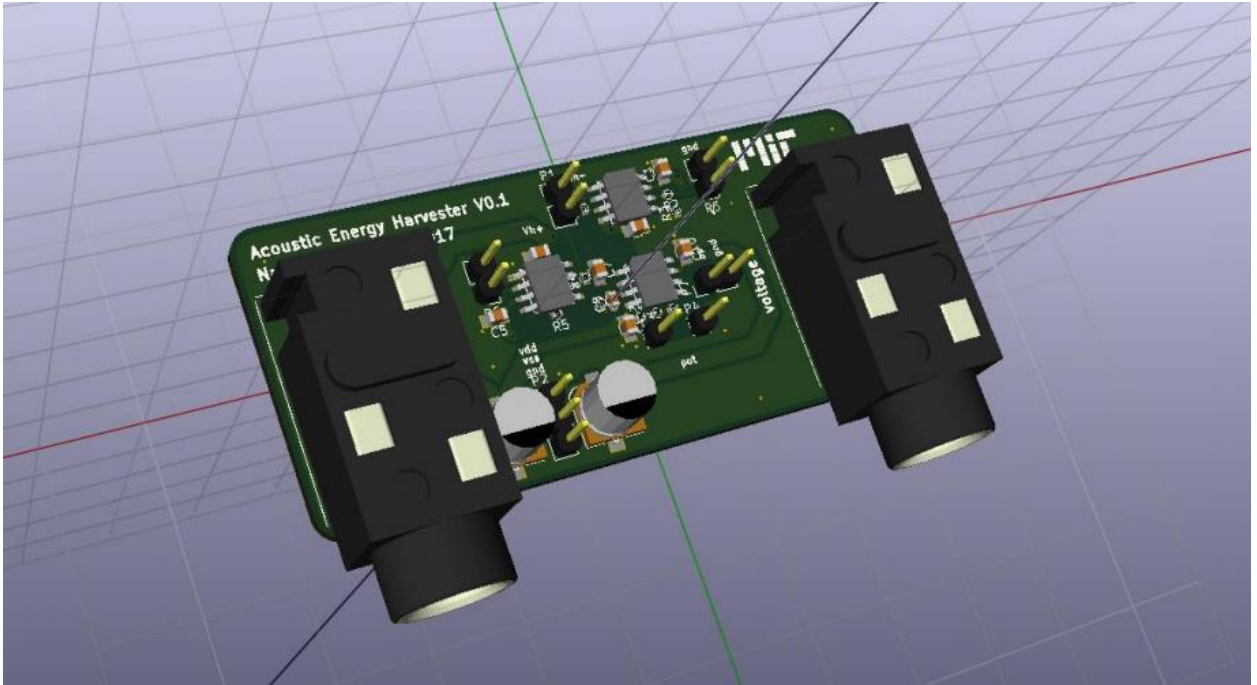
Top copper layer:

Bottom copper layer:

PCB 3D view

Appendix E

MATLAB Stability Analysis Code

Symbolic code for stability analysis, as discussed in Section 5.4.4.

```matlab
%Stability_TF.m
%Nathan Monroe
%5/4/2017
%made to look at vout/vin relatino and understand low-frequency poles.

%syms z1 z2 z3 z4 A real;
syms A s Rt Ct Rh R3 C R2 R1 real;
z1 = R1;
z2 = R2;
z3 = (R3/(s*C))/(R3+(1/(s*C)));
z4 = Rt + Rh + (1/(s*Ct));



%see drawing. Op amp out goes Z2 to Z1 to gnd via noninverting.
%op amp out goes Z3 to Z4 via inverting input to source.
%A is op amp gain

%transfer function of Vout/Vin
tf6 = (-A*z3)/(z3+z4);
tf7 = -A*z1/(z1+z2);
tf8 = A*z4/(z3+z4);
VoTF = tf6/(1+tf7+tf8);
VoTF = simplify(VoTF);
pretty(VoTF)
```

Numerical code for stability analysis, as discussed in Section 5.4.4.

```matlab
%Stability_TF_real.m
%Nathan Monroe
%5/4/2017
%Uses matlab tf models to model the harvester's vout/vin transfer function.
clear all;

s = tf('s');

%A = (19e6)/((s/1.53)-1); %op amp gain, with dominant pole
```

```matlab
A=19e6; %ideal op amp
Rt = 18.8; %Harvester model Rth
Ct = 16.47e-9; %thevenin source model cap, 16.47nF.
Rh = 18.8; %matched real load
R3 = 2.55e6; %resistor in parallel with neg feedback cap. 1megaohm to start
C = 1660.e-9; %negative feedback cap. 100x cap to be cancelled for now.
R2 = 500; %positive feedback resistors
R1 = 50e3;

z1 = R1; %op amp noninverting input to gnd
z2 = R2; %op amp output to noninverting input
%z3 = 1/(s*Cn); %no parallel resistor in negative feedback
z3 = (R3/(s*C))/(R3+(1/(s*C)));
z4 = Rt + Rh + (1/(s*Ct));

tf1 = (-A*z3)/(z3+z4);
tf2 = -A*z1/(z1+z2);
tf3 = A*z4/(z3+z4);
VoTF = tf1/(1+tf2+tf3);
opts = bodeoptions;
opts.FreqUnits = 'Hz';
opts.xlim=[1, 10^4];
opts.Grid = 'on';
figure();
bode(VoTF,opts)
figure();
pzmap(VoTF);
grid on;

p1 = -1/(C*R3)
p2 = ((-Ct*(Rh+Rt))+(-R3*(C+Ct))+sqrt((((-Ct*(Rh+Rt))+(-R3*(C+Ct)))^2)-
(4*C*Ct*R3*(Rh+Rt))))/(2*C*Ct*R3*(Rh+Rt))
p3 = ((-Ct*(Rh+Rt))+(-R3*(C+Ct))-sqrt((((-Ct*(Rh+Rt))+(-R3*(C+Ct)))^2)-
(4*C*Ct*R3*(Rh+Rt))))/(2*C*Ct*R3*(Rh+Rt))
Y = (R1/(R1+R2))-(1/A); %intermediate variable Y
p4a = C*R3*(Rh+Rt)*(Y-1);
p4b = (Y*R3)+((Y-1)*(Rh+Rt+(C*R3/Ct)));
p4c = (1/Ct)*(Y-1);

p4 = (-p4b + sqrt((p4b^2)-(4*p4a*p4c)))/(2*p4a)
p5 = (-p4b - sqrt((p4b^2)-(4*p4a*p4c)))/(2*p4a)
```

References

[1]   Nakajima, Heidi. "Acoustics, Production and Perception of Speech". HST.714. MIT, Cambridge MA. October 2016.

[2]   Rosowski, John. "Electric-Mechanic-Acoustic Transformers". HST.714. MIT, Cambridge MA. September 2016.

[3]   Chang, S.C. June 2013. "Harvesting Energy From Non-Ideal Vibrations". Retreived from MIT D-Space. http://hdl.handle.net/1721.1/82346.

[4]   Pillai et al. A Review of Acoustic Energy Harvesting. INTERNATIONAL JOURNAL OF PRECISION ENGINEERING AND MANUFACTURING Vol. 15, No. 5, pp. 949-965.

[5]   Horowitz et al. MEMS Acoustic Energy Harvester. PowerMEMS 2005.

[6]   Zhu et al. Strategies for Increasing the Operating Frequency Range of Vibration Energy Harvesters: A Review. MEASUREMENT SCIENCE AND TECHNOLOGY, 2010.

[7]   Phipps et al. Demonstration of a wireless, self-powered, electroacoustic

      liner system. J. Acoust. Soc. Am. 125 (2), February 2009.

[8]   Williams et al. 1996 Analysis of a micro-electric generator for microsystems. *Sensors Actuators,* A 52 8–11.

[9]   Petropoulos T, Yeatman EM, Mitcheson PD. MEMS coupled resonators for power generation and sensing. Micromechanics Europe, Leuven, Belgium; 2004.

[10] Kaphengst et al. Adaptive Load Synthesis for Autonomous Resonant Frequency Tuning of Electromagnetic Energy Harvesters. PowerMEMS 2012, Atlanta, GA, USA, December 2-5, 2012.

[11] Chang et al. Harvesting Energy from Multi-Frequency Vibrations With a Tunable Electrical Load. PowerMEMS 2012, Atlanta, GA, USA, December 2-5, 2012.

[12] Mallick et al. An Electrically Tunable Low Frequency Electromagnetic Energy Harvester. Procedia Engineering 87 (2014) 771 – 774.

[13] Kim, S. H., Ji, C. H., Galle, P., Herrault, F., Wu, X., and et al., "An Electromagnetic Energy Scavenger from Direct Airflow," Journal of Micromechanics and Microengineering, Vol. 19, No. 9, Paper No. 094010, 2009.

[14] Horowitz, St., Development of a MEMS-based Acoustic Energy Harvester, University of Florida, PhD Thesis, 2005.

[15] Schlecht et al. Active Power Factor Correction for Switching Power Supplies. IEEE Transactions On Power Electronics, Vol. Pe-2, No. 4, October 1987.

[16] Eargle's The Microphone Book: From Mono to Stereo to Surround - A Guide to Microphone Design and Application 3rd Edition. Ray A Rayburn. Focal Press, 2011.

[17] Toh et al. Electronic Resonant Frequency Tuning of a Marine Energy Harvester. In Proceedings of the PowerMEMS, Seoul, Korea, 15–18 November, 2011; pp. 383–386.

[18] Sluka et al. Sound Shielding by a Piezoelectric Membrane and a Negative Capacitor with Feedback Control. IEEE Transactions on Ultrasonics, Ferroelectrics, and Frequency Control, vol. 55, no. 8, August 2008.

[19] Sluka et al. Feedback Control of Piezoelectric Actuator Elastic Properties in a Vibration Isolation System, Ferroelectrics, 351:1, 51-61, DOI: 10.1080/00150190701353051. 2007.

[20] Date et al. Electrically controlled elasticity utilizing piezoelectric coupling. Journal of Applied Physics, vol 87, no 2, January 2000.

[21] Fukada et al. Sound Isolation By Piezoelectric Polymer Films Connected With Negative Capacitance Circuits. 11th International Symposium on Electrets. Pp. 223-226. 2002.

[22] Kim et al. Broadband Noise Reduction Of Piezoelectric Smart Panel Featuring Negative-Capacitive-Converter Shunt Circuit. J. Acoust. Soc. Am. 120 (4), October 2006.

[23] Kodama et al. Vibration Control of Curved Piezoelectric Sheets Using Negative Capacitance Circuits. Ferroelectrics, 351:33–42, 2007.

[24] Korde et al. The Effect Of A Negative Capacitance Circuit On The Out-Of-Plane Dissipation And Stiffness Of A Piezoelectric Membrane. Smart Mater. Struct. 17 035017. 2008.

[25] Introduction to Microsystem Design. Schomburg, W.K. Springer, 2011.

[26] Diagnostic Ultrasound Imaging Inside Out. T.L. Szabo. Elsevier Academic Press, 2004.

[27] Principles of Power Electronics. Kassakian, J.G. et al. Pearson, 1991.